

**THÈSE DE DOCTORAT
DE SORBONNE UNIVERSITÉ**

Spécialité : Physique

École doctorale n°564: Physique en Île-de-France

réalisée

au Laboratoire Kastler Brossel

sous la direction de Pierre-François Cohadon

présentée par

Pierre-Edouard Jacquet

pour obtenir le grade de :

DOCTEUR DE SORBONNE UNIVERSITÉ

Sujet de la thèse :

Squeezed light optomechanics: Theory and Experiments

soutenue le 26 Février 2026

devant le jury composé de :

M ^{me}	Agnès MAITRE	PU	INSP (SU)	Présidente
M	Pierre VERLOT	MC	LuMIn (UPSaclay)	Rapporteur
M	Jean-Pierre ZENDRI	DR	INFN (UPadova)	Rapporteur
M ^{me}	Sara DUCCI	PU	MPQ (UPCité)	Examinaterice
M	Jack HARRIS	PU	Yale University	Examinateur
M	Pierre-François COHADON	MC	LKB (ENS)	Directeur



Remerciements

Merci bien

Contents

Introduction	3
Historical background	3
State of the art	3
Relevance of this work	3
I Theory: Background	5
I.1 Optics	7
I.1.1 Spatial Modes	7
I.1.2 Quantum Description	7
I.1.3 Coherent and Squeezed States	15
I.1.4 Classical Modulations	20
I.1.5 Quantum Sideband Diagram	22
I.2 Cavities	22
I.2.1 Cavity Geometries and Stability Conditions	22
I.2.2 Cavity Resonances	24
I.2.3 Mode-Matching	25
I.2.4 Simple Cavities	25
I.2.5 Non Linear Cavities	35
I.2.6 Optomechanical Cavities	42

I.3 Detection	48
I.3.1 Direct detection	48
I.3.2 Balanced Homodyne Detection	51
II Theory: Squeezed Light & Optomechanics	53
II.1 Squeezed Light and Optomechanics	55
II.1.1 Standard Quantum Limit	55
II.1.2 Frequency Independent Squeezing in Optomechanical Cavities	58
II.1.3 Frequency Dependent Squeezing in Optomechanical Cavities	61
II.1.4 Filter Cavities for Frequency Dependent Squeezing	62
II.2 Cavity Optomechanics with Membrane based systems	63
II.2.1 Classical Description	63
II.2.2 Quantum Description	67
III Experimental Methods	71
III.1 Feedback control	72
III.1.1 Overview	72
III.1.2 Proportion-Integral (PI) Controllers	73
III.1.3 PyRPL overview	75
III.1.4 IQ modules	77
III.2 Locking techniques	79
III.2.1 Temperature Lock	80
III.2.2 Optical phase Lock	80
III.2.3 Cavity Locks	81
III.2.4 Offset Frequency Locks and Phase Lock Loop	84
IV Experiments: Optomechanics	87

IV.1 System Description and Setup	88
IV.1.1 Previous LKB work and Motivation	88
IV.1.2 Specifications and Design	89
IV.1.3 Flexure Actuation	93
IV.1.4 Experimental Setup	95
IV.1.5 Alignment Procedures	97
IV.2 Experimental Characterization	97
IV.2.1 Cavity Scans	97
IV.2.2 Cavity Locking and Mechanical Characterization	106
IV.2.3 Bistability	109
IV.3 Design of an Optomechanical Fibered Cavity	109
IV.3.1 Design considerations	109
V Experiments: Squeezed Light	111
V.1 Optical Setup Overview	112
V.2 Cavity Resonances and Locks	113
V.2.1 IRMC Cavity	113
V.2.2 SHG Cavity	114
V.2.3 OPO Cavity	116
V.3 Spectral analysis	116
V.3.1 Detection of Squeezing and Anti-squeezing	116
V.3.2 Spectral Variation with Frequency	116
V.3.3 Optimal Quadrature Conditions	116
V.4 Filter Cavity Concept	116
V.4.1 Virgo Filter Cavity	116
V.4.2 Thermal effects in bichromatic locks	116

Conclusion	119
Summary of Work	119
Outlooks	119
Final Remarks	119
Appendix A: Two-photon derivations	121
Field Quantization	121
Two photon formalism	123
Derivation of the optimal angle	129
Appendix B: Error Signals	131
Direct detection error signals	131
PDH error signal	133
Bibliography	141

Introduction

Historical background

State of the art

Relevance of this work

Chapter I

Theory: Background

This chapter will cover the elementary concepts required to describe an membrane based optomechanical system in a quantum regime. We will first recall basics on optical field quantization as well describing coherent and squeezed light field, to then turn to the more specific frequency dependent squeezed light field. Secondly, we will cover the mathematical description of a mechanical resonator interacting with a generic coherent optical field, highlighting the differences with the seminal optomechanical system of a mirror on a spring. Finally, we will derive the equations of motions of a membrane based optomechanical system with frequency dependent squeezed optical fields [1].

Contents

I.1	Optics	7
I.1.1	Spatial Modes	7
I.1.2	Quantum Description	7
I.1.3	Coherent and Squeezed States	15
I.1.4	Classical Modulations	20
I.1.5	Quantum Sideband Diagram	22
I.2	Cavities	22
I.2.1	Cavity Geometries and Stability Conditions	22
I.2.2	Cavity Resonances	24
I.2.3	Mode-Matching	25
I.2.4	Simple Cavities	25
I.2.5	Non Linear Cavities	35
I.2.6	Optomechanical Cavities	42
I.3	Detection	48
I.3.1	Direct detection	48
I.3.2	Balanced Homodyne Detection	51

I.1 Optics

I.1.1 Spatial Modes

The spatial structure of an electromagnetic wave propagating along the z -axis can be described by a set of well-defined transverse modes, which are solutions of the paraxial Helmholtz equation. The most fundamental solution is the Gaussian mode, whose electric field amplitude reads

$$E(\mathbf{r}) = E_0 \frac{w_0}{w(z)} \exp\left(-\frac{x^2 + y^2}{w^2(z)}\right) \exp\left[-i\left(kz + \frac{k(x^2 + y^2)}{2R(z)} - \psi(z)\right)\right], \quad (\text{I.1})$$

where $\mathbf{r} = (x, y, z)$, E_0 is the field amplitude at the beam waist, $k = 2\pi/\lambda$ the wavenumber, and λ the optical wavelength. The various quantities introduced above are defined as

$$\begin{aligned} w(z) &\equiv w_0 \sqrt{1 + (z/z_R)^2}, & z_R &\equiv \pi w_0^2 / \lambda, \\ R(z) &\equiv z [1 + (z_R/z)^2], & \psi(z) &\equiv \arctan(z/z_R), \end{aligned}$$

with w_0 the waist, z_R the Rayleigh range, $R(z)$ the wavefront curvature, and $\psi(z)$ the Gouy phase. A compact expression of the Gaussian envelope is written as

$$E(\mathbf{r}) = E_0 \frac{iz_R}{q(z)} \exp\left(-\frac{ik(x^2 + y^2)}{2q(z)}\right) e^{ikz} \quad \text{with} \quad q(z) \equiv z + iz_R, \quad (\text{I.2})$$

where we defined the complex beam parameter $q(z)$. Beyond the fundamental Gaussian mode, more general solutions of the paraxial equation can be constructed. In Cartesian coordinates, these are the Hermite–Gaussian modes TEM_{mn} , given by

$$\begin{aligned} E_{mn}(\mathbf{r}) &= E_0 \frac{w_0}{w(z)} H_m\left(\frac{\sqrt{2}x}{w(z)}\right) H_n\left(\frac{\sqrt{2}y}{w(z)}\right) \exp\left(-\frac{x^2 + y^2}{w^2(z)}\right) \\ &\quad \times \exp\left[-i\left(kz + \frac{k(x^2 + y^2)}{2R(z)} - (m + n + 1)\psi(z)\right)\right], \quad (\text{I.3}) \end{aligned}$$

where H_m, H_n are Hermite polynomials.

I.1.2 Quantum Description

Quantised Electromagnetic Field

We will consider both cases of a finite quantisation volume V and an infinite volume: when dealing with cavity modes, we will use the finite volume description, while for propagating modes carrying sideband correlations we will use the infinite volume description, under the

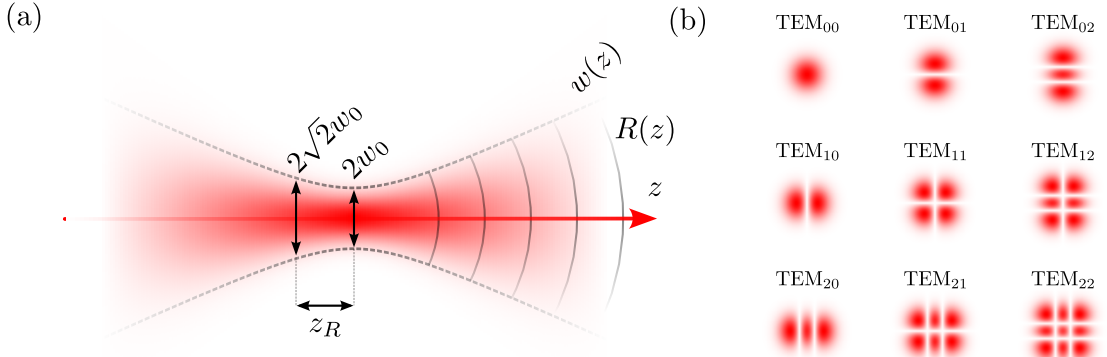


Fig. I.1 Gaussian beam characteristics: (a) Intensity profile of the fundamental Gaussian mode at different positions along the propagation axis z . The various quantities introduced in the text are indicated. (b) Transverse intensity profiles of the first few Hermite–Gaussian modes TEM_{mn} . These modes form an orthonormal basis to describe the spatial structure of paraxial beams: any realistic beam can be decomposed as a superposition of these modes.

two-photon formalism prescription. Both descriptions are linked through the input-output formalism introduced later on.

We first consider the quantised electromagnetic field in a volume V . The electric field operator can be written as

$$\hat{\mathbf{E}}(\mathbf{r}, t) = i \sum_{\ell} \mathcal{E}_{\ell} \left[\hat{a}_{\ell} \mathbf{f}_{\ell}(\mathbf{r}) e^{-i\omega_{\ell}t} - \hat{a}_{\ell}^{\dagger} \mathbf{f}_{\ell}^*(\mathbf{r}) e^{+i\omega_{\ell}t} \right], \quad (\text{I.4})$$

where $\mathcal{E}_{\ell} = \sqrt{\frac{\hbar\omega_{\ell}}{2\varepsilon_0 V}}$ is the field amplitude per photon in mode ℓ , \hbar is the reduced Planck constant, ω_{ℓ} is the angular frequency of mode ℓ , and ε_0 is the vacuum permittivity. The spatial mode functions $\mathbf{f}_{\ell}(\mathbf{r})$ form an orthonormal basis in V according to

$$\int_V d^3r \mathbf{f}_{\ell}^*(\mathbf{r}) \cdot \mathbf{f}_{\ell'}(\mathbf{r}) = \delta_{\ell\ell'}, \quad \mathbf{f}_{\ell}(\mathbf{r}) \propto E_{mn}(\mathbf{r}) \boldsymbol{\epsilon}_x$$

where we assumed a linearly polarized field along the x -axis, with $\boldsymbol{\epsilon}_x$ the corresponding unit vector. The index $\ell = (m, n)$ then labels the different spatial modes, the Hermite–Gaussian modes in our case.

In the limit of an infinite quantisation volume $V \rightarrow \infty$, the discrete mode index ℓ becomes a continuous variable i.e. the mode spacing becomes infinitesimal. As detailed in the Appendix, we now need to consider a continuum of modes with annihilation operator $\hat{a}[\omega]$ labeled by their angular frequency ω . To come down to the two-photon formalism, we make

the following assumptions :

- We consider frequencies $\omega = \omega_0 \pm \Omega$ centered around a carrier frequency ω_0 , with $\Omega \in [-B, +B] \ll \omega_0$ where B is the bandwidth. This is valid since the bandwidth B , generally up to tens of GHz, is small compared to ω_0 which is hundreds of THz for optical frequencies.
- We consider a single spatial mode, i.e. we drop the spatial dependence of the field and consider only one transverse mode function $\mathbf{f}(\mathbf{r})$, the fundamental Gaussian mode imposed by the laser source and/or spatial filtering elements. This is valid since the spatial envelope of the beam does not vary significantly over the considered bandwidth. The spatial mode function is then factored out of the integrals over frequency.
- We consider the electric field operator to only be dependent on time t , having projected the field onto the transverse mode function and integrated over the transverse plane, as well as setting the propagation coordinate $z = 0$ for simplicity.

Upon these assumptions, the electric field operator reduces to a time dependent operator (Heisenberg picture) expressed as

$$\hat{E}(t) = \mathcal{E}_0 \left[\cos\left(\omega_0 t - \frac{\pi}{2}\right) \int_{-\infty}^{\infty} \frac{d\Omega}{2\pi} (\hat{a}_+ + \hat{a}_-^\dagger) e^{-i\Omega t} + \sin\left(\omega_0 t - \frac{\pi}{2}\right) \int_{-\infty}^{\infty} \frac{d\Omega}{2\pi} i(\hat{a}_-^\dagger - \hat{a}_+) e^{-i\Omega t} \right] \quad (\text{I.5})$$

where we defined the sideband annihilation operators as $\hat{a}_+ \equiv \hat{a}[\omega_0 + \Omega]$ and $\hat{a}_- \equiv \hat{a}[\omega_0 - \Omega]$. The field amplitude per photon at the carrier frequency is given by $\mathcal{E}_0 = \sqrt{\hbar\omega_0/2\varepsilon_0 c A}$, where A is the effective cross-sectional area of the beam and c the speed of light in vacuum. The explicit relationship between the discrete mode operator \hat{a}_ℓ and the continuous mode operator $\hat{a}[\omega]$ (and thus their hermitian conjugate) is given in the Appendix.

Note: Although the electric field operator is written in the Heisenberg picture, the annihilation and creation operators $\hat{a}[\omega]$ and $\hat{a}[\omega]^\dagger$ are Schrodinger like operators, i.e. time independent operators. This is because we already factored out the time dependence $e^{-i\omega t}$ associated to each frequency mode when writing our annihilation/creation operators. As seen later on, the time dependence of the field operator defined through the Fourier transform arises from the superposition of many frequency modes, leading to beating at frequency Ω . This is the heart of the two-photon formalism, where a time dependent field Heisenberg like operator is built from the superposition of Schrodinger like annihilation/creation operators at different frequencies. In the literature, the schrodinger like operators are sometimes written as \hat{a}_ω to draw a parallel between the discrete mode case \hat{a}_ℓ , but we will stick to the

$\hat{a}[\omega]$ notation to avoid confusion with time dependent operators.

When writing annihilation operators, we will often drop the frequency dependence to lighten the notation, but it is implicit that they depend on frequency i.e. $\hat{a} \equiv \hat{a}[\omega]$, such that it applies to both sideband operators \hat{a}_+ and \hat{a}_- .

Commutation Relations

As demonstrated in the Appendix, the continuous annihilation and creation operators satisfy the following commutation relations:

$$[\hat{a}[\omega], \hat{a}^\dagger[\omega']] = 2\pi \delta(\omega - \omega'), \quad [\hat{a}[\omega], \hat{a}[\omega']] = 0, \quad [\hat{a}^\dagger[\omega], \hat{a}^\dagger[\omega']] = 0.$$

such that the sideband operators satisfy

$$[\hat{a}_\pm, \hat{a}_\pm^\dagger] = 2\pi \delta(\Omega - \Omega'), \quad [\hat{a}_\pm, \hat{a}_\mp] = 0, \quad [\hat{a}_\pm^\dagger, \hat{a}_\mp^\dagger] = 0.$$

Quadrature Operators

We describe the phase-space properties of a field mode using hermitian quadrature operators. These are linear combinations of the annihilation and creation operators that correspond to measurable observables in the electromagnetic field. Here again, we won't write explicitly the frequency dependence, but it is implicit in the following i.e. $\hat{\mathbf{u}} \equiv \hat{\mathbf{u}}[\Omega]$ and $\hat{\mathbf{a}} \equiv \hat{\mathbf{a}}[\Omega]$. The two most common quadratures are defined as follows:

$$\hat{\mathbf{u}} \equiv \begin{pmatrix} \hat{a}_1 \\ \hat{a}_2 \end{pmatrix} = \boldsymbol{\Gamma} \hat{\mathbf{a}} \quad \text{with} \quad \boldsymbol{\Gamma} \equiv \begin{pmatrix} 1 & 1 \\ -i & i \end{pmatrix} \quad \text{and} \quad \hat{\mathbf{a}} \equiv \begin{pmatrix} \hat{a}_+ \\ \hat{a}_-^\dagger \end{pmatrix} \quad (\text{I.6})$$

where we defined the field vector $\hat{\mathbf{a}}$ and the transfer matrix $\boldsymbol{\Gamma}$, later used to switch from *one-photon* to *two-photon* description of optical elements. The electric field operator can then be recasted as

$$\hat{E}(t) = \mathcal{E}_0 \left[\cos\left(\omega_0 t - \frac{\pi}{2}\right) \int_{-\infty}^{\infty} \frac{d\Omega}{2\pi} \hat{a}_1[\Omega] e^{-i\Omega t} + \sin\left(\omega_0 t - \frac{\pi}{2}\right) \int_{-\infty}^{\infty} \frac{d\Omega}{2\pi} \hat{a}_2[\Omega] e^{-i\Omega t} \right]. \quad (\text{I.7})$$

where it is now explicit that the electric field features two orthogonal components oscillating at the carrier frequency ω_0 , with amplitudes given by the quadrature operators \hat{a}_1 and \hat{a}_2 .

Fourier Transform

We now come to the aforementioned building of a time dependent field operator from the superposition of many frequency modes. This is done through the Fourier transform defined as

$$\begin{aligned}\hat{\mathbf{a}}(t) &= \int_{-\infty}^{+\infty} \frac{d\Omega}{2\pi} e^{-i\Omega t} \hat{\mathbf{a}}[\Omega] \\ \hat{\mathbf{a}}[\Omega] &= \int_{-\infty}^{+\infty} dt e^{i\Omega t} \hat{\mathbf{a}}(t)\end{aligned}\quad (\text{I.8})$$

In this definition, a notable property is that the hermitian conjugate in the time domain translates to a frequency inversion in the Fourier domain:

$$[\hat{a}(t)]^\dagger = \hat{a}^\dagger(t), \quad [\hat{a}_+]^\dagger = \hat{a}_-. \quad (\text{I.9})$$

It then follows that the quadrature operators in the time domain are effectively Hermitian operators, as expected for observables, while the frequency domain quadrature operators satisfy

$$\hat{a}_1^\dagger[\Omega] = \hat{a}_1[-\Omega], \quad \hat{a}_2^\dagger[\Omega] = \hat{a}_2[-\Omega]. \quad (\text{I.10})$$

Commutation Relations in vector form

The matrix form commutator in both time and frequency space reads

$$[\hat{\mathbf{a}}, \hat{\mathbf{a}}^\dagger] = \sigma_z \times \begin{cases} \delta(t - t') \\ 2\pi\delta(\Omega - \Omega'). \end{cases} \quad (\text{I.11})$$

with σ_z the Pauli Z matrix, and where it is implicit that we evaluate both at different frequencies or times respectively. An arbitrary rotated quadrature pair is obtained by

$$\hat{\mathbf{u}}_\phi \equiv \mathbf{R}(\phi) \hat{\mathbf{u}} = \mathbf{R}(\phi) \Gamma \hat{\mathbf{a}} \quad \text{with} \quad \mathbf{R}(\phi) \equiv \begin{pmatrix} \cos \phi & \sin \phi \\ -\sin \phi & \cos \phi \end{pmatrix}. \quad (\text{I.12})$$

and where we identify the useful identity

$$\mathbf{R}(\phi) \Gamma = \begin{pmatrix} e^{-i\phi} & e^{i\phi} \\ -ie^{-i\phi} & ie^{i\phi} \end{pmatrix}.$$

The commutators of the rotated quadrature operators read

$$[\hat{\mathbf{u}}_\phi, \hat{\mathbf{u}}_\phi^\dagger] = 2i \mathbf{J} \begin{cases} \delta(t - t') \\ 2\pi\delta(\Omega - \Omega') \end{cases} \quad \text{with} \quad \mathbf{J} \equiv \begin{pmatrix} 0 & 1 \\ -1 & 0 \end{pmatrix}. \quad (\text{I.13})$$

This identity would not be true had we considered large sideband frequencies $\Omega \sim \omega_0$ i.e. it would feature corrections in all \mathbf{J} terms, including diagonal.

Linearization of the optical field

Let's now consider a quantum state living in this continuous mode space $|\psi\rangle$. We can always linearize the field operators around their mean value, which is particularly useful when dealing with intense fields featuring small quantum fluctuations around a large classical amplitude. This is the case for coherent and squeezed states, which are introduced right below. The annihilation operator is then be decomposed as

$$\hat{a} = \bar{a} + \delta\hat{a} \quad (\text{I.14})$$

where $\bar{a} = \langle\psi|\hat{a}|\psi\rangle \in \mathbb{C}$ is the mean complex amplitude of the quantum state, and $\delta\hat{a}$ represents quantum fluctuations with $\langle\psi|\delta\hat{a}|\psi\rangle = 0$. Note this decomposition is valid for any quantum state, including coherent and squeezed states. We note \bar{a} to distinguish it from the complex amplitude α of a coherent state introduced below, which is a specific case of this decomposition. The field vector is then expressed as

$$\hat{\mathbf{a}} = \begin{pmatrix} \bar{a}_+ \\ \bar{a}_-^* \end{pmatrix} + \begin{pmatrix} \delta\hat{a}_+ \\ \delta\hat{a}_-^\dagger \end{pmatrix} = \bar{\mathbf{a}} + \delta\hat{\mathbf{a}} \quad (\text{I.15})$$

and it then follows that the quadrature operators can also be expressed as

$$\hat{\mathbf{u}}_\phi = \mathbf{R}(\phi) \boldsymbol{\Gamma} (\bar{\mathbf{a}} + \delta\hat{\mathbf{a}}) = \bar{\mathbf{u}}_\phi + \delta\hat{\mathbf{u}}_\phi. \quad (\text{I.16})$$

For the vacuum state $|0\rangle$, we have $\bar{a}_\pm = 0$ and thus $\hat{\mathbf{a}} = \delta\hat{\mathbf{a}}$. Since we will always consider fluctuations around the mean value, we will systematically use the notation $\delta\hat{a}$ to refer to the annihilation operator, unless specified otherwise, as well as assuming the vacuum state as the reference when we write average values as $\langle \cdot \rangle \equiv \langle 0 | \cdot | 0 \rangle$. All the above definitions and properties thus apply to the fluctuation operators (commutation relations, Fourier transforms, etc.).

Amplitude and Phase Quadratures

Considering the mean field amplitude $\bar{\alpha} = |\bar{\alpha}|e^{i\bar{\varphi}}$, we will often refer to the amplitude and phase quadratures, defined respectively as the quadratures at angles $\phi = \bar{\varphi}$ and $\phi = \bar{\varphi} + \pi/2$. As the angle $\bar{\varphi}$ defines the mean field phase relative to a reference (e.g. a local oscillator), we will assume without loss of generality that $\bar{\varphi} = 0$, such that the amplitude and phase quadratures correspond to \hat{a}_1 and \hat{a}_2 respectively. We will then relabel them as

$$\delta\hat{p} \equiv \delta\hat{a}_{\phi=0} = \delta\hat{a}_1, \quad \delta\hat{q} \equiv \delta\hat{a}_{\phi=\pi/2} = \delta\hat{a}_2. \quad (\text{I.17})$$

Noise Spectral Density Matrix

A central concept in this thesis is the two-sided Noise Spectral Density matrix of the quadrature fluctuations, which characterizes the second-order statistical properties of the quantum state in the frequency domain. Namely, it describes the spectral distribution of the variances and covariances of the quadrature fluctuations. For a given quadrature angle ϕ , it is defined as

$$\begin{aligned} \mathbf{S}_\phi[\Omega] &= \frac{1}{2} \int \frac{\delta\Omega'}{2\pi} \langle \{\delta\hat{\mathbf{u}}_\phi, \delta\hat{\mathbf{u}}_\phi^\dagger\} \rangle \\ &= \frac{1}{2} \int \frac{\delta\Omega'}{2\pi} \mathbf{R}(\phi) \langle \{\delta\hat{\mathbf{u}}, \delta\hat{\mathbf{u}}^\dagger\} \rangle \mathbf{R}(-\phi) \\ &= \frac{1}{2} \int \frac{\delta\Omega'}{2\pi} \mathbf{R}(\phi) \begin{pmatrix} \langle \{\delta\hat{p}, \delta\hat{p}^\dagger\} \rangle & \langle \{\delta\hat{p}, \delta\hat{q}^\dagger\} \rangle \\ \langle \{\delta\hat{q}, \delta\hat{p}^\dagger\} \rangle & \langle \{\delta\hat{q}, \delta\hat{q}^\dagger\} \rangle \end{pmatrix} \mathbf{R}(-\phi) \end{aligned} \quad (\text{I.18})$$

where $\{\hat{A}, \hat{B}\} = \hat{A}\hat{B} + \hat{B}\hat{A}$ denotes the anticommutator, implicitly evaluated at frequencies Ω and Ω' , and integrated over Ω' . The diagonal elements of the noise spectral density matrix correspond to the power spectral densities of the quadrature fluctuations, while the off-diagonal elements represent the cross-spectral densities between different quadratures. The noise spectral density matrix is a Hermitian matrix, reflecting the physical properties of the quantum state. We will particularly focus on the amplitude and phase quadrature noise spectral density matrix, obtained by setting $\phi = 0$, and we will denote it as $\mathbf{S}[\Omega] \equiv \mathbf{S}_{\phi=0}[\Omega]$. The subscripts will then denote whether we refer to the transmitted or reflected fields of an optical cavity, the output spectrum of a squeezer, etc. For completeness we introduce the single-sided noise spectral density matrix, defined as

$$\bar{\mathbf{S}}_\phi[\Omega] = \frac{1}{2} (\mathbf{S}_\phi[\Omega] + \mathbf{S}_\phi[-\Omega]) \quad (\text{I.19})$$

such that the variance of a quadrature operator can be retrieved by integrating the single-sided noise spectral density over positive frequencies only (as one would with a real signal in

a spectrum analyzer). A generalized version of the Heisenberg uncertainty relation can be expressed in terms of the noise spectral density matrix as

$$\det \mathbf{S}_\phi[\Omega] \geq 1 \quad (\text{I.20})$$

which sets a fundamental limit on the simultaneous knowledge of the quadrature fluctuations at a given frequency Ω .

Vacuum state

For the vacuum state $|0\rangle$, we derive the noise spectral density matrix using the commutation relations and the fact that $\langle \delta\hat{a} \rangle = 0$ (see Annexe). The calculation yields

$$\mathbf{S}_{\text{vac}}[\Omega] = \begin{pmatrix} 1 & 0 \\ 0 & 1 \end{pmatrix} \quad (\text{I.21})$$

for any angle ϕ and frequency Ω . This result indicates that the vacuum state has equal fluctuations in both quadratures, with no correlations between them, as expected for a minimum uncertainty state. The noise spectral density matrix of the vacuum state serves as a reference point for comparing other quantum states, such as coherent and squeezed states, which exhibit different fluctuation properties.

Linear Optical Systems

As we will develop further in the next section, the output fields of various optical systems can be expressed in a general linear form as

$$\delta\hat{\mathbf{u}}_{\text{out}} = \mathbf{T} \delta\hat{\mathbf{u}}_{\text{in}} + \mathbf{L} \delta\hat{\mathbf{u}}_{\text{vac}}. \quad (\text{I.22})$$

where \mathbf{T} and \mathbf{L} are 2×2 frequency dependent transfer matrices. The input and vacuum fields are assumed to be in the vacuum state, as well as being uncorrelated such that

$$\begin{aligned} \langle \delta\hat{\mathbf{u}}_{\text{in}} \delta\hat{\mathbf{u}}_{\text{in}}^\dagger \rangle &= 2\pi\delta(\Omega + \Omega')\mathbf{S}_{\text{in}}[\Omega] \\ \langle \delta\hat{\mathbf{u}}_{\text{vac}} \delta\hat{\mathbf{u}}_{\text{vac}}^\dagger \rangle &= 2\pi\delta(\Omega + \Omega')\mathbf{1} \\ \langle \delta\hat{\mathbf{u}}_{\text{in}} \delta\hat{\mathbf{u}}_{\text{vac}}^\dagger \rangle &= \mathbf{0} \end{aligned} \quad (\text{I.23})$$

Computing the noise spectra is then straightforward :

$$\mathbf{S}_{\text{out}}[\Omega] = \mathbf{T}\mathbf{S}_{\text{in}}\mathbf{T}^\dagger + \mathbf{L}\mathbf{L}^\dagger \quad (\text{I.24})$$

where $\mathbf{S}_{\text{vac}} = \mathbf{1}$ as seen above. For an arbitrary quadrature angle ϕ , we simply rotate the transfer matrices as

$$\mathbf{T}_\phi = \mathbf{R}(\phi) \mathbf{T} \mathbf{R}(-\phi), \quad \mathbf{L}_\phi = \mathbf{R}(\phi) \mathbf{L} \mathbf{R}(-\phi)$$

such that

$$\mathbf{S}_{\text{out},\phi}[\Omega] = \mathbf{T}_\phi \mathbf{S}_{\text{in},\phi} \mathbf{T}_\phi^\dagger + \mathbf{L}_\phi \mathbf{L}_\phi^\dagger \quad (\text{I.25})$$

Graphical Representation of Gaussian States

For Gaussian states, we can actually picture them in a 2D space, where the two axes correspond to the two quadratures \hat{a}_1 and \hat{a}_2 . In the case where the mean phase is zero, these quadratures correspond to the amplitude and phase quadratures \hat{p} and \hat{q} . The quantum state can then be represented as a 2D Gaussian distribution centered around the mean values of the quadratures, with the shape and orientation of the distribution characterized by the off diagonal elements of the noise spectral density matrix. The uncertainties in the quadratures are represented by the widths of the Gaussian distribution along each axis, while correlations between the quadratures are represented by the tilt of the distribution. This graphical representation provides an intuitive way to visualize and understand the properties of Gaussian quantum states, such as coherent and squeezed states, in terms of their quadrature fluctuations and correlations.

I.1.3 Coherent and Squeezed States

We now turn to standard optical quantum states, in particular gaussian states i.e. full positive in Wigner function representations such as coherent and squeezed states, that we will denote in braket notation as $|\alpha\rangle$ and $|\alpha, r, \theta\rangle$.

Coherent States:

The monochromatic coherent state $|\alpha\rangle$ is an eigenstate of the annihilation operator:

$$\hat{a}_+ |\alpha\rangle = \alpha \delta(\Omega) |\alpha\rangle \quad (\text{I.26})$$

where $\alpha = |\alpha| e^{i\bar{\varphi}}$ is a complex number representing the mean coherent amplitude. In this notation, the angle $\bar{\varphi}$ is the mean angle of the distribution, used to describe the relative phase to a reference (e.g. a local oscillator), as in Fig ???. The \hat{a} linear decomposition above (Eq I.14) then yields $\alpha = \bar{\alpha}$ for a coherent state. A generic multimode coherent state is generated by the displacement operator $\hat{D}(\alpha)$ such that

$$|\alpha\rangle = \hat{D}(\alpha) |0\rangle \quad (\text{I.27})$$

where the general expression for the displacement operator acting on the vacuum state is given by

$$\hat{D}(\alpha) = \exp\left(\int \frac{d\Omega}{2\pi} [\alpha(\Omega)\hat{a}_-^\dagger - \alpha^*(\Omega)\hat{a}_+]\right) \quad (\text{I.28})$$

which collapses to

$$\hat{D}(\alpha) = \exp\left(\frac{1}{2\pi} [\alpha\hat{a}^\dagger[\omega_0] - \alpha^*\hat{a}[\omega_0]]\right) \quad (\text{I.29})$$

when defining a monochromatic coherent state $\alpha(\Omega) = \alpha\delta(\Omega)$, that is a coherent state at the carrier frequency only. Upon the action of this displacement operator, the sideband operator is transformed as

$$D^\dagger(\alpha)\hat{a}_+ D(\alpha) = \hat{a}_+ + \alpha\delta(\Omega) \quad (\text{I.30})$$

such that we can verify the eigenvalue equation (Eq I.26) straightforwardly as

$$\begin{aligned} \hat{a}_+ |\alpha\rangle &= D(\alpha)(D^\dagger(\alpha)\hat{a}_+ D(\alpha)) |0\rangle \\ &= \hat{D}(\alpha)(\alpha\delta(\Omega) + \hat{a}_+) |0\rangle \\ &= \alpha\delta(\Omega) |\alpha\rangle \end{aligned}$$

Expectation values: Using the quadrature vector $\hat{\mathbf{u}}_\phi$ (Eq I.12), and the $\mathbf{R}\Gamma$ identity, the expectation values in a coherent state are

$$\langle \hat{D}^\dagger \hat{\mathbf{u}}_\phi \hat{D} \rangle = \mathbf{R}(\phi) \langle \hat{D}^\dagger \hat{\mathbf{u}} \hat{D} \rangle = 2\delta(\Omega) \begin{pmatrix} \text{Re}(|\alpha|e^{i(\bar{\varphi}-\phi)}) \\ \text{Im}(|\alpha|e^{i(\bar{\varphi}-\phi)}) \end{pmatrix} \quad (\text{I.31})$$

such that the components reduce to $2\text{Re}(\alpha)$ and $2\text{Im}(\alpha)$ if $\phi = 0$, and to $2|\alpha|$ and 0 if $\phi = \bar{\varphi}$, or equivalently if we set $\bar{\varphi} = \phi = 0$ as mentioned earlier (such that $\hat{\mathbf{u}}$ corresponds to the amplitude and phase quadratures). We also notice the delta function at $\Omega = 0$, indicating that the coherent state has a non-zero mean field only at the carrier frequency.

Spectrum: For a coherent state, the fluctuations are identical to that of the vacuum state, seen directly from equation (I.30). Since the fluctuation operators are unchanged by the displacement, the noise spectral density matrix remains that of the vacuum:

$$\mathbf{S}_{\text{coh}}[\Omega] = \mathbf{S}_{\text{vac}} = \begin{pmatrix} 1 & 0 \\ 0 & 1 \end{pmatrix} \quad (\text{I.32})$$

for any angle ϕ and frequency Ω . Relating to the linear optical systems introduced, this is equivalent to having identity transfer matrices $\mathbf{T} = \mathbf{1}$ and $\mathbf{L} = \mathbf{0}$, such that no additional noise is added to the input vacuum fluctuations. Coherent states only differ from vacuum by their non-zero mean field amplitudes at the carrier frequency $\Omega = 0$, symbolized by the

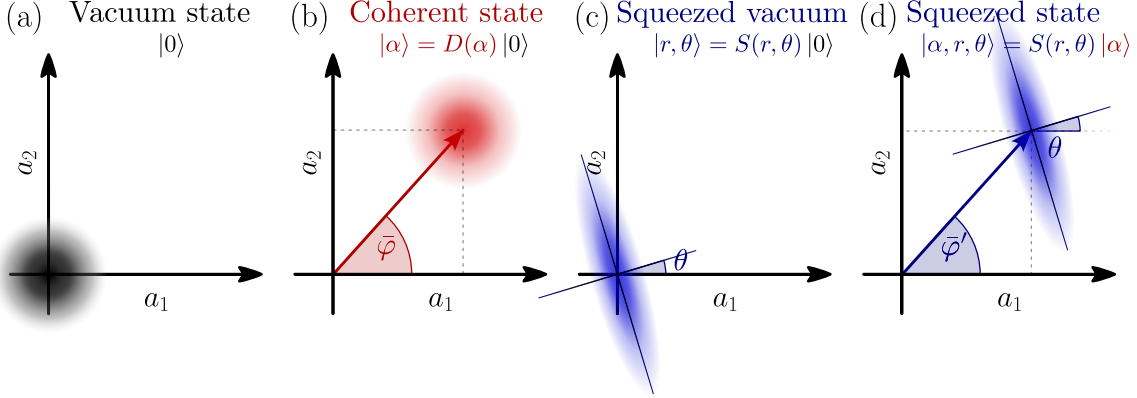


Fig. I.2 Phase-space representations of Gaussian quantum states. 2D cuts of the Wigner function in the quadrature plane ($a_1[\Omega]$, $a_2[\Omega]$) at a given frequency. (a) vacuum state: a circular Gaussian centered at the origin, featuring equal quantum fluctuations in both a_1 and a_2 quadratures. (b) coherent state: a displaced circular Gaussian, showing a shift in phase space along an angle φ with vacuum fluctuations. This corresponds to either the carrier ($\Omega = 0$), or a sideband frequency with a non zero modulation. (c) vacuum squeezed state: an elliptical Gaussian centered at the origin, with reduced noise along a rotated quadrature and increased noise in the orthogonal direction. (d) bright squeezed state: an ellipse shifted away from the origin, combining anisotropic fluctuations and a nonzero mean amplitude. The displacement angle φ and squeezing angle θ are independent.

delta function in the expectation values above.

Squeezed States:

Squeezed states $|\alpha, r, \theta\rangle$ are quantum gaussian states of light in which the noise (variance) of one quadrature is reduced below the vacuum level, at the expense of increased noise in the conjugate quadrature. A generic squeezed state is characterized by three parameters: the displacement amplitude α , the squeezing parameter r , and the squeezing angle θ . The so called 'bright' squeezed state is generated by applying both a displacement and a squeezing operation to the vacuum state:

$$|\alpha, r, \theta\rangle = \hat{S}(r, \theta)\hat{D}(\alpha)|0\rangle \quad (\text{I.33})$$

where the squeezing operator $\hat{S}(r, \theta)$ is defined as

$$\hat{S}(r, \theta) = \exp\left(r \int_{-\infty}^{\infty} \frac{d\Omega}{2\pi} \left[e^{-i2\theta(\Omega)} \hat{a}_+ \hat{a}_- - e^{i2\theta(\Omega)} \hat{a}_+^\dagger \hat{a}_-^\dagger \right] \right) \quad (\text{I.34})$$

where we assumed the squeezing parameter r to be frequency independent. This operator describes the process of parametric down-conversion, where pairs of photons are created

or annihilated in the sideband modes \hat{a}_\pm with a phase relation determined by the squeezing angle $\theta(\Omega)$. We can then write the action of the squeezing operator on the sideband operators as

$$\hat{S}^\dagger \hat{a}_+ \hat{S} = \hat{a}_+ \cosh r - e^{i2\theta(\Omega)} \hat{a}_-^\dagger \sinh r \quad (\text{I.35})$$

and similarly for \hat{a}_- . This transformation shows how the squeezing operator mixes the annihilation and creation operators, leading to modified quadrature fluctuations in the squeezed state. Applying both transformations (displacement and squeezing) to the field vector, we have

$$\hat{D}^\dagger \hat{S}^\dagger \hat{a}_+ \hat{S} \hat{D} = \hat{a}_+ \cosh r - e^{i2\theta} \hat{a}_-^\dagger \sinh r + \gamma \delta(\Omega) \quad (\text{I.36})$$

with $\gamma = \alpha \cosh r - \alpha^* e^{i2\theta} \sinh r = |\gamma| e^{i\bar{\varphi}'}$ the displaced amplitude at the carrier frequency. We stress that the phase $\bar{\varphi}'$ generally differs from the displacement angle $\bar{\varphi}$ of the coherent amplitude α .

Expectation values: Similarly as in a coherent state, but this time from Eq (I.36), we can derive the expectation values of the quadrature vector in a bright squeezed state as

$$\langle \hat{D}^\dagger \hat{S}^\dagger \hat{\mathbf{u}}_\phi \hat{S} \hat{D} \rangle = \mathbf{R}(\phi) \langle \hat{D}^\dagger \hat{S}^\dagger \hat{\mathbf{u}} \hat{S} \hat{D} \rangle = 2\delta(\Omega) \begin{pmatrix} \text{Re}(|\gamma| e^{i(\bar{\varphi}' - \phi)}) \\ \text{Im}(|\gamma| e^{i(\bar{\varphi}' - \phi)}) \end{pmatrix} \quad (\text{I.37})$$

indicating that the mean field is shifted by the displaced amplitude γ at the carrier frequency ω_0 .

Spectrum: We identify the field fluctuation transformation under the squeezing and displacement operators from I.36:

$$\hat{D} \hat{S}^\dagger \delta \hat{\mathbf{a}} \hat{S} \hat{D} = \begin{pmatrix} \cosh r & -e^{i2\theta(\Omega)} \sinh r \\ -e^{-i2\theta(\Omega)} \sinh r & \cosh r \end{pmatrix} \delta \hat{\mathbf{a}} \quad (\text{I.38})$$

such that the quadrature fluctuations read

$$\hat{D}^\dagger \hat{S}^\dagger \delta \hat{\mathbf{u}} \hat{S} \hat{D} = \mathbf{T} \delta \hat{\mathbf{u}} \quad (\text{I.39})$$

where we defined the transfer matrix

$$\begin{aligned} \mathbf{T} &= \begin{pmatrix} \cosh r - \sinh r \cos 2\theta(\Omega) & -\sinh r \sin 2\theta(\Omega) \\ -\sinh r \sin 2\theta(\Omega) & \cosh r + \sinh r \cos 2\theta(\Omega) \end{pmatrix} \\ &= \mathbf{R}(-\theta) e^{-r\sigma_z} \mathbf{R}(\theta) \end{aligned}$$

Using the linear optical system formalism introduced earlier, we identify the transfer matrices

\mathbf{T} and $\mathbf{L} = \mathbf{0}$ (no additional noise). The noise spectral density matrix of a bright squeezed state is then computed as

$$\mathbf{S}_{\text{sqz}}[\Omega] = \mathbf{T}\mathbf{S}_{\text{vac}}\mathbf{T}^\dagger = \mathbf{T}\mathbf{T}^\dagger. \quad (\text{I.40})$$

Explicitly, this yields

$$\begin{aligned} \mathbf{S}_{\text{sqz}}[\Omega] &= \mathbf{R}(-\theta)e^{-2r\sigma_z}\mathbf{R}(\theta) \\ &= \begin{pmatrix} \cosh 2r - \sinh 2r \cos 2\theta(\Omega) & -\sinh 2r \sin 2\theta(\Omega) \\ -\sinh 2r \sin 2\theta(\Omega) & \cosh 2r + \sinh 2r \cos 2\theta(\Omega) \end{pmatrix}. \end{aligned} \quad (\text{I.41})$$

This result shows how the squeezing parameter r and squeezing angle θ influence the quadrature fluctuations in the squeezed state. The diagonal elements of the noise spectral density matrix represent the variances of the quadrature fluctuations, while the off-diagonal elements represent the correlations between the quadratures. At an arbitrary measurement angle ϕ , the noise spectral density matrix is given by

$$\begin{aligned} \mathbf{S}_{\text{sqz},\phi}[\Omega] &= \mathbf{R}(\phi)\mathbf{S}_{\text{sqz}}[\Omega]\mathbf{R}(-\phi) \\ &= \mathbf{R}(\phi - \theta)e^{-2r\sigma_z}\mathbf{R}(\theta - \phi). \end{aligned} \quad (\text{I.42})$$

such that measuring along the squeezing angle $\phi = \theta(\Omega)$ yields the minimum variance in the first quadrature.

To obtain a full band reduction, one can then either use a frequency dependent squeezing angle $\theta(\Omega)$ and a fixed measurement quadrature ϕ , or inversely if the squeezing angle is fixed, one can rotate the measurement quadrature ϕ . These two techniques are known as frequency dependent squeezing [2] and variational readout [Vyatchanin1993, 2] respectively. Frequency dependent squeezing is the focus of our work here, and will be detailed in Chapter II.

Amplitude and Phase squeezed states: Considering a displaced squeezed state, two special cases are of interest: the amplitude squeezed state where $\theta = \bar{\varphi}$ and the phase squeezed state where $\theta = \bar{\varphi} + \pi/2$. In the first case, the amplitude quadrature \hat{p} is squeezed, while the phase quadrature \hat{q} is anti-squeezed. In the second case, the phase quadrature is squeezed, while the amplitude quadrature is anti-squeezed. The covariance matrices for these states can be derived from Eq. (I.109) by setting $\psi = 0$ or $\psi = \pi/2$, respectively.

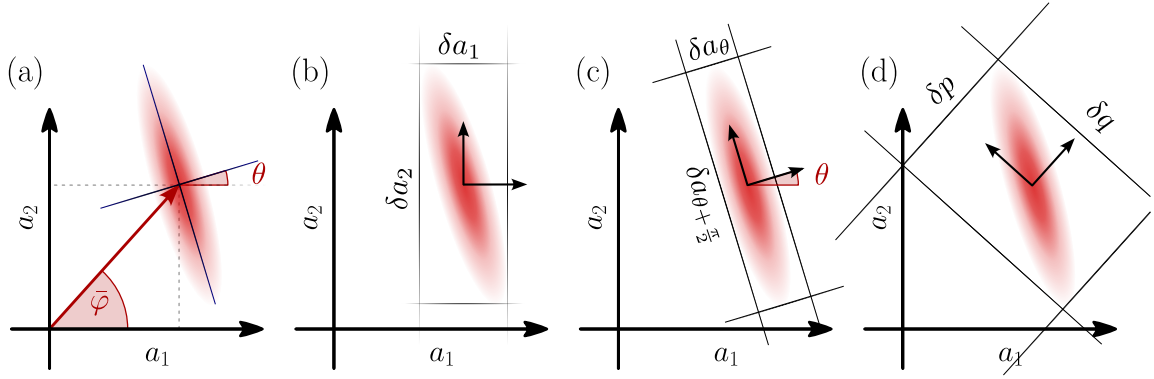


Fig. I.3 Phase-space representations of bright squeezed states with the different quadratures choices. (a) generic bright squeezed state. (b) projection of the quantum noise on the standard quadratures (a_1, a_2) . (c) projection of the quantum noise on the ellipse major axes quadratures $(a_\theta, a_{\theta+\pi/2})$, with θ the ellipse angle with respect to the standard quadratures. (d) projection of the quantum noise on the amplitude and phase quadratures (p, q) .

I.1.4 Classical Modulations

A key ingredient in our study is the concept of sidebands generated by classical modulations of a coherent field. These sidebands are frequency components that appear around the carrier frequency of the field due to the modulation process. We will consider two types of classical modulations: amplitude modulation (AM) and phase modulation (PM). These are instrumental in experimental physics, as they notably allow to extract usable error signals as to stabilize and lock various parameters of an optical setup, such as the length of a cavity or the phase of a local oscillator. Additionally, as we will see later, the optomechanical interaction itself is seen as a phase modulation of the intracavity field by the mechanical motion, generating sidebands and noises that carry information about the mechanical position.

Amplitude Modulation (AM) : Let the classical amplitude be modulated at Ω_{mod} in amplitude:

$$\alpha(t) = \bar{\alpha} (1 + \epsilon_a \cos(\Omega_{\text{mod}} t)) \quad (\text{I.43})$$

with $\epsilon_a \ll 1$, the field amplitude modulation depth. While the DC term lives at frequency ω_0 , the modulation introduces sidebands at frequencies $\omega_0 \pm \Omega_{\text{mod}}$, seen by expanding the cosine:

$$\alpha(t) = \bar{\alpha} \left(1 + \frac{\epsilon_a}{2} e^{i\Omega_{\text{mod}} t} + \frac{\epsilon_a}{2} e^{-i\Omega_{\text{mod}} t} \right) \quad (\text{I.44})$$

Phase Modulation (PM) : Now let the classical amplitude be modulated in phase at frequency Ω_{mod} :

$$\alpha(t) = \bar{\alpha} e^{i\epsilon_\phi \cos(\Omega_{\text{mod}} t)} \quad (\text{I.45})$$

with $\epsilon_\phi \ll 1$ the field phase modulation depth. Expanding to first order in ϵ_ϕ gives:

$$\alpha(t) \approx \bar{\alpha} \left(1 + \frac{i\epsilon_\phi}{2} e^{i\Omega_{\text{mod}} t} + \frac{i\epsilon_\phi}{2} e^{-i\Omega_{\text{mod}} t} \right) \quad (\text{I.46})$$

While the carrier term lives at frequency ω_0 , the modulation introduces sidebands at $\omega_0 \pm \Omega_{\text{mod}}$, both shifted in phase by $\pi/2$ relative to the carrier.

In both cases, amplitude or phase modulations, the field contains a carrier at frequency ω and two sidebands at $\omega \pm \Omega$. Amplitude modulation results in sidebands that are in phase with the carrier, while phase modulation produces sidebands with a $\pm\pi/2$ phase shift relative to the carrier. We also note a general modulation process as :

$$\alpha(t) = \bar{\alpha} (1 + \varepsilon(t)) \quad (\text{I.47})$$

where $\varepsilon(t) \in \mathbb{C}$ is a modulation function that weakly modulates the complex amplitude in time, and that features information about the modulation frequency and depth. It then follows that the linearized amplitude-phase operators can be expressed as

$$\hat{\mathbf{u}}_{\bar{\alpha}}(t) = 2|\bar{\alpha}| \begin{pmatrix} 1 \\ 0 \end{pmatrix} + 2|\bar{\alpha}| \begin{pmatrix} \text{Re}(\varepsilon(t)) \\ \text{Im}(\varepsilon(t)) \end{pmatrix} + \begin{pmatrix} \delta\hat{p}(t) \\ \delta\hat{q}(t) \end{pmatrix} \quad (\text{I.48})$$

Computing the Fourier transform for amplitude and phase modulations yields

$$\begin{aligned} \varepsilon^{AM}(\Omega) &= \frac{\epsilon_a}{2} \left(\delta(\Omega - \Omega_{\text{mod}}) + \delta(\Omega + \Omega_{\text{mod}}) \right) \\ \varepsilon^{PM}(\Omega) &= \frac{i\epsilon_\phi}{2} \left(\delta(\Omega - \Omega_{\text{mod}}) + \delta(\Omega + \Omega_{\text{mod}}) \right) \end{aligned} \quad (\text{I.49})$$

And the quadrature operators of a modulated field can be expressed as

$$\hat{\mathbf{u}}_{\bar{\alpha}}[\Omega] = 2|\bar{\alpha}| \begin{pmatrix} 1 \\ 0 \end{pmatrix} \delta(\Omega) + 2|\bar{\alpha}| \begin{pmatrix} \text{Re}(\varepsilon[\Omega]) \\ \text{Im}(\varepsilon[\Omega]) \end{pmatrix} + \begin{pmatrix} \delta\hat{p}[\Omega] \\ \delta\hat{q}[\Omega] \end{pmatrix} \quad (\text{I.50})$$

We illustrate this by computing the spectra of a coherent field modulated in amplitude. The amplitude-phase quadrature fluctuation part reads

$$\delta\hat{\mathbf{u}}_{\bar{\alpha}}[\Omega] = |\bar{\alpha}|\epsilon_a \begin{pmatrix} \delta(\Omega - \Omega_{\text{mod}}) + \delta(\Omega + \Omega_{\text{mod}}) \\ 0 \end{pmatrix} + \begin{pmatrix} \delta\hat{p}[\Omega] \\ \delta\hat{q}[\Omega] \end{pmatrix} \quad (\text{I.51})$$

such that its covariance matrix reads

$$\mathbf{S}_{\bar{\alpha}}[\Omega] = 2|\bar{\alpha}|^2 \epsilon_a^2 \left[\delta(\Omega - \Omega_{\text{mod}}) + \delta(\Omega + \Omega_{\text{mod}}) \right] \begin{pmatrix} 1 & 0 \\ 0 & 0 \end{pmatrix} + \mathbf{1} \quad (\text{I.52})$$

As seen in the above expression, the covariance matrix display a sum of dirac functions corresponding to a classical amplitude modulation of the field, as well as a flat vacuum noise across all frequencies.

I.1.5 Quantum Sideband Diagram

We now have all the tools to graphically represent the quantum states of light in the frequency domain. The so-called quantum sideband diagram is a useful representation to visualize the quantum states of light, especially when dealing with modulated fields and their sidebands. In this representation, we plot the carrier frequency ω_0 at the center, and the sidebands at frequencies $\omega_0 \pm \Omega$ on either side.

Each sideband is represented by a vector in the quadrature plane, with its length and angle determined by the amplitude and phase of the sideband as seen above. The quantum noise associated with each sideband is represented by a gaussian distribution around the tip of the vector, with its shape and orientation determined by the noise spectral density matrix of the quantum state. The additional ingredient that the sideband diagram provides is the correlation between symmetrical sidebands, represented by markers connecting the two sidebands at $\omega_0 + \Omega$ and $\omega_0 - \Omega$. These correlations are crucial in understanding the properties of squeezed states, where the noise in one quadrature is reduced below the vacuum level, while the noise in the conjugate quadrature is increased. The sideband diagram allows us to visualize these correlations and their impact on the overall quantum state of light. This representation is particularly useful when analyzing the effects of optical cavities and other linear optical systems on quantum states, as they modify the amplitude and phase of the sidebands, hence the correlated/anticorrelated quadratures.

I.2 Cavities

Optical cavities are at the heart of this work, as they are used to coherently enhance the light-matter interaction in various systems, and also to filter and manipulate quantum states of light. In this section, we review the basic properties of optical cavities, their resonance conditions, and we derive the covariance matrices of their output fields.

I.2.1 Cavity Geometries and Stability Conditions

An optical cavity is a structure that *traps* photons by means of reflection between two or more mirrors. They can be either standing wave cavities, where the light bounces back and forth between two mirrors, or traveling wave cavities, where the light circulates in a loop. In both cases, the cavity supports discrete resonant modes determined by its geometry and the boundary conditions imposed by the mirrors. The stability criteria of a specific cavity

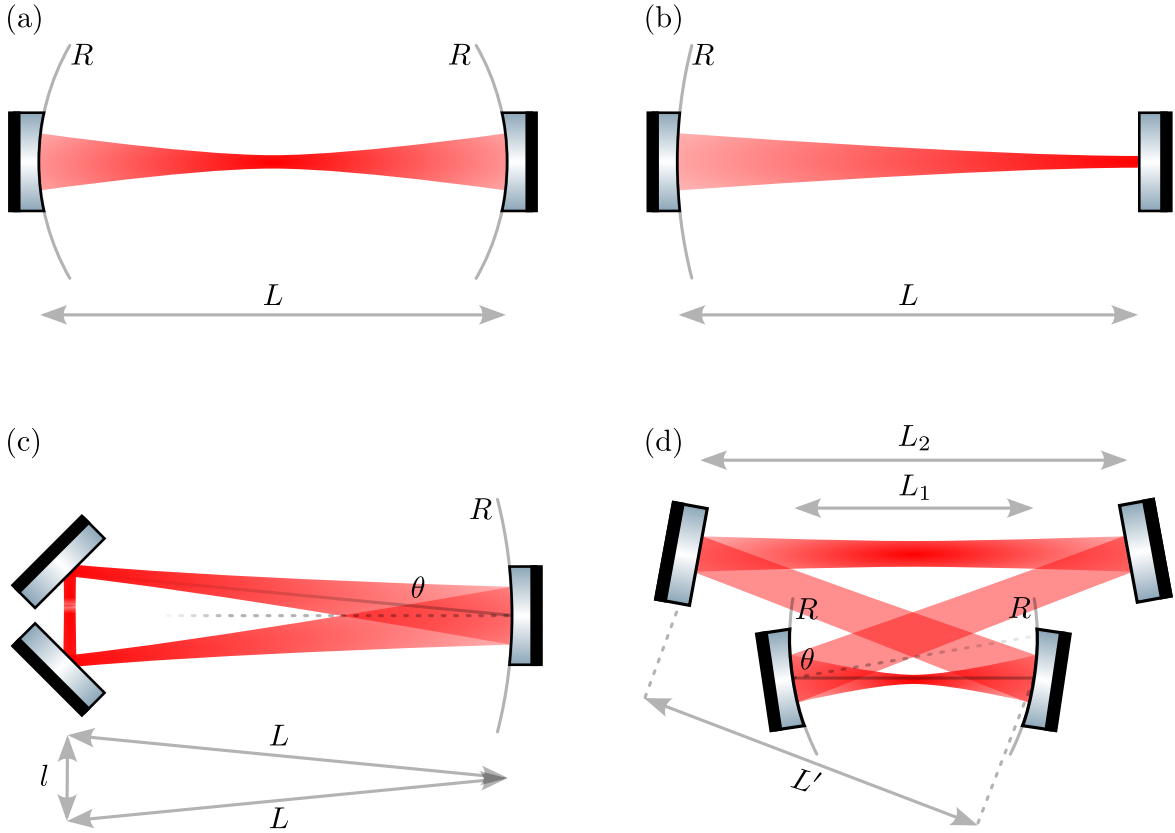


Fig. I.4 Geometries of various cavity types used in this work. (a) Linear concave-concave cavity (confocal in the $L \sim 2R$ case). (b) Linear plano-concave cavity. (a) and (b) are both standing wave cavities. (c) Planar triangular cavity. (d) Planar bow-tie cavity. (c) and (d) are both travelling wave cavities.

configuration is derived considering the round trip ABCD matrix of the cavity describing how the complex beam parameter $q(z)$ introduced in (I.2) transforms after one round trip. The stability condition then simply reads as $-1 < (A + D)/2 < 1$. In the case of planar - travelling wave cavities, one needs to consider both the tangential and sagittal planes, as these cavities are astigmatic. The stricter condition, generally the sagittal plane one, then defines the stability range of the cavity.

Linear standing wave cavities: We first consider the two linear cavities used in this work, namely a concave-concave cavity (Fig I.13.(a)) with two identical concave mirrors, and a plano-concave cavity with one flat mirror and one concave mirror (Fig I.13.(b)). Using the ABCD formalism for a confocal cavity of length L formed by two identical mirrors of radii of curvature R , the stability condition reads

$$0 < L < 2R \quad (\text{I.53})$$

For the plano-concave cavity, the stability condition reads

$$0 < L < R \quad (\text{I.54})$$

Planar traveling wave cavities: We now consider a triangular cavity formed by two concave mirrors of radius of curvature R and one flat mirror (Fig I.13.(c)). The stability condition reads

$$0 < L_{rt} < 2R \cos(\theta) \quad (\text{I.55})$$

where $L_{rt} = 2L + l$ is the cavity round trip length, and θ is the angle of incidence of the beam onto the curved mirror. This condition is the sagittal one, and is more stringent than the tangential one.

Considering now a bow-tie cavity formed by two concave mirrors of radius of curvature R and two flat mirrors (Figure I.13.(d)), the full stability condition reads

$$0 < \left(1 - \frac{L_1 + 2L'}{R \cos \theta}\right) \left(1 - \frac{L_2}{R \cos \theta}\right) < 1 \quad (\text{I.56})$$

where L_1 is the distance between the two concave mirrors, L_2 the distance between the two flat mirrors, and L' the distance between a concave and a flat mirror (assuming a symmetric cavity). A simple design rule guaranteeing stability is then to set $L_1 + 2L' < R \cos \theta$ and $L_2 < R \cos \theta$.

I.2.2 Cavity Resonances

If the cavity is stable, it will then feature a discrete set of resonant modes everytime the cavity length is an integer multiple of half the wavelength $\lambda/2$ (standing wave cavity) or the wavelength λ (traveling wave cavity). In the frequency domain, modes are spaced by the free spectral range ω_{FSR} of the cavity, defined as

$$\omega_{\text{FSR}} = \frac{\pi c}{L} \quad (\text{linear cavity}), \quad \omega_{\text{FSR}} = \frac{2\pi c}{L_{rt}} \quad (\text{traveling wave cavity}) \quad (\text{I.57})$$

such that the resonant frequencies are given by

$$\omega_m = m \omega_{\text{FSR}}, \quad m \in \mathbb{N} \quad (\text{I.58})$$

and the cavity is on resonance when the input laser frequency ω_0 matches one of the resonant frequencies ω_m i.e. $\omega_0 = \omega_m$. To achieve this, one can either tune the laser frequency or the cavity length. In our experiments, we use the second option by mounting one of the cavity

mirrors on a piezoelectric actuator. Changing the cavity length L by δL shifts the resonant frequencies by

$$\delta\omega_m = -m \frac{\pi c}{L^2} \delta L = -\frac{\omega_m}{L} \delta L \quad (\text{I.59})$$

I.2.3 Mode-Matching

A cavity also supports TEM_{mn} transverse modes, each with a specific spatial profile and resonant frequency. The resonant frequencies of these transverse modes are shifted relative to the fundamental mode by an amount that depends on the cavity geometry and the mode indices (m, n) . Coupling an incoming beam into a stable optical cavity requires that the spatial mode of the beam matches that of the cavity. This means that the mode function of the incoming beam, assumed to be a TEM_{00} Gaussian mode $f_0(\mathbf{r})$, must overlap with the cavity's fundamental mode $f'_0(\mathbf{r})$. If the basis functions are not perfectly aligned, the incoming field can be expanded in the orthonormal basis of cavity modes as

$$f_0(\mathbf{r}) = c_0 f'_0(\mathbf{r}) + \sum_{m>0} c_m f'_m(\mathbf{r}), \quad (\text{I.60})$$

where the coefficients c_m quantify the projection of the incident field onto the cavity eigenmodes. Only the component $c_0 f'_0$ couples efficiently to the fundamental cavity mode due to the mirror geometry, while any mismatch excites higher-order transverse modes f'_m . The mode-matching procedure therefore consists in maximizing the overlap integral

$$\eta = \left| \int d^3\mathbf{r} f_0^*(\mathbf{r}) f'_0(\mathbf{r}) \right|^2, \quad (\text{I.61})$$

which ensures that essentially all the incoming photons populate the desired cavity mode, while suppressing excitation of spurious modes.

I.2.4 Simple Cavities

We consider a single field cavity mode described by the annihilation operator \hat{a} , interacting with several independent noise inputs. The system is governed by a Hamiltonian

$$\hat{H} = -\hbar\Delta\hat{a}^\dagger\hat{a} \quad (\text{I.62})$$

with $\Delta \equiv \omega_0 - \omega_c$ the cavity detuning to the laser frequency, and each input introduces dissipation characterized by a decay rate $\kappa_i = T_i/\tau$, with T_i the power transmittivity of the mirror and $\tau = 2L/c$ the roundtrip time of the cavity. This is we consider an input coupler (mirror) with decay rate κ_1 and an output coupler (mirror) with decay rate κ_2 . The laser

field is shone onto the cavity by the input coupler.

In the frame rotating at the laser frequency, the dynamics of \hat{a} is given by the Quantum Langevin Equation (QLE):

$$\begin{aligned}\frac{d}{dt}\hat{a}(t) &= -\frac{i}{\hbar}[\hat{a}, \hat{H}] - \frac{\kappa}{2}\hat{a}(t) + \sqrt{\kappa_1}\hat{a}_{\text{in}}(t) + \sqrt{\kappa_2}\delta\hat{a}_{\text{vac}}(t) + \sqrt{\kappa_0}\delta\hat{a}_{\text{l}}(t) \\ &= -\left(\frac{\kappa}{2} - i\Delta\right)\hat{a}(t) + \sqrt{\kappa_1}\hat{a}_{\text{in}}(t) + \sqrt{\kappa_2}\delta\hat{a}_{\text{vac}}(t) + \sqrt{\kappa_0}\delta\hat{a}_{\text{l}}(t)\end{aligned}\quad (\text{I.63})$$

where $\kappa = \kappa_0 + \kappa_1 + \kappa_2$ is the total decay rate, with $\kappa_0 = \mathcal{L}/\tau$ and $\delta\hat{a}_{\text{l}}(t)$ the rate and fluctuation operator of additional losses. Here losses \mathcal{L} have ppm units. Another key element to deriving both steady state behaviour as well as quadrature spectra is the input-output formula given by:

$$\hat{a}_{\text{ref}} = \sqrt{\kappa_1}\hat{a} - \hat{a}_{\text{in}}, \quad \hat{a}_{\text{trans}} = \sqrt{\kappa_2}\hat{a} - \delta\hat{a}_{\text{vac}} \quad (\text{I.64})$$

for both the reflected and transmitted field. In the input-output formula, the \hat{a}_{in} refers to the field incoming on the coupler considered, which are simple vacuum fluctuations on the output coupler since we don't shine the laser by this port. Importantly, this formula describes how open quantum systems exchange information with their environment, linking the internal cavity field to the external fields. Here, the external fields are the two photon fields defined at the start of this chapter, expressed in units of $1/\sqrt{\text{Hz}}$, and the internal field \hat{a} is unitless. This key relation allows to compute how a discrete quantum system (the cavity mode) interacts with continuous quantum fields (the input and output fields), enabling the analysis of phenomena such as reflection, transmission, and noise properties of the cavity.

As introduced in the previous subsection, one can split the annihilation operator in a mean field part α and a fluctuation part $\delta\hat{\mathbf{a}}(t)$ (vector form) such that this equation turns into two i.e. a scalar differential equation, and an operator differentail equation, that is:

$$\begin{cases} 0 = -\left(\frac{\kappa}{2} - i\Delta\right)\bar{\alpha} + \sqrt{\kappa_1}\bar{\alpha}_{\text{in}} \\ \delta\dot{\hat{\mathbf{a}}}(t) = -\begin{pmatrix} \kappa/2 - i\Delta & 0 \\ 0 & \kappa/2 + i\Delta \end{pmatrix}\delta\hat{\mathbf{a}}(t) + \sqrt{\kappa_1}\delta\hat{a}_{\text{in}}(t) + \sqrt{\kappa_2}\delta\hat{a}_{\text{vac}}(t) + \sqrt{\kappa_0}\delta\hat{a}_{\text{l}}(t) \end{cases} \quad (\text{II.62})$$

Mean field solution (Static case): Taking the first scalar equation and expressing the mean intracavity field gives

$$\bar{\alpha} = \frac{\sqrt{\kappa_1}}{\kappa/2 - i\Delta}\bar{\alpha}_{\text{in}} \quad (\text{I.65})$$

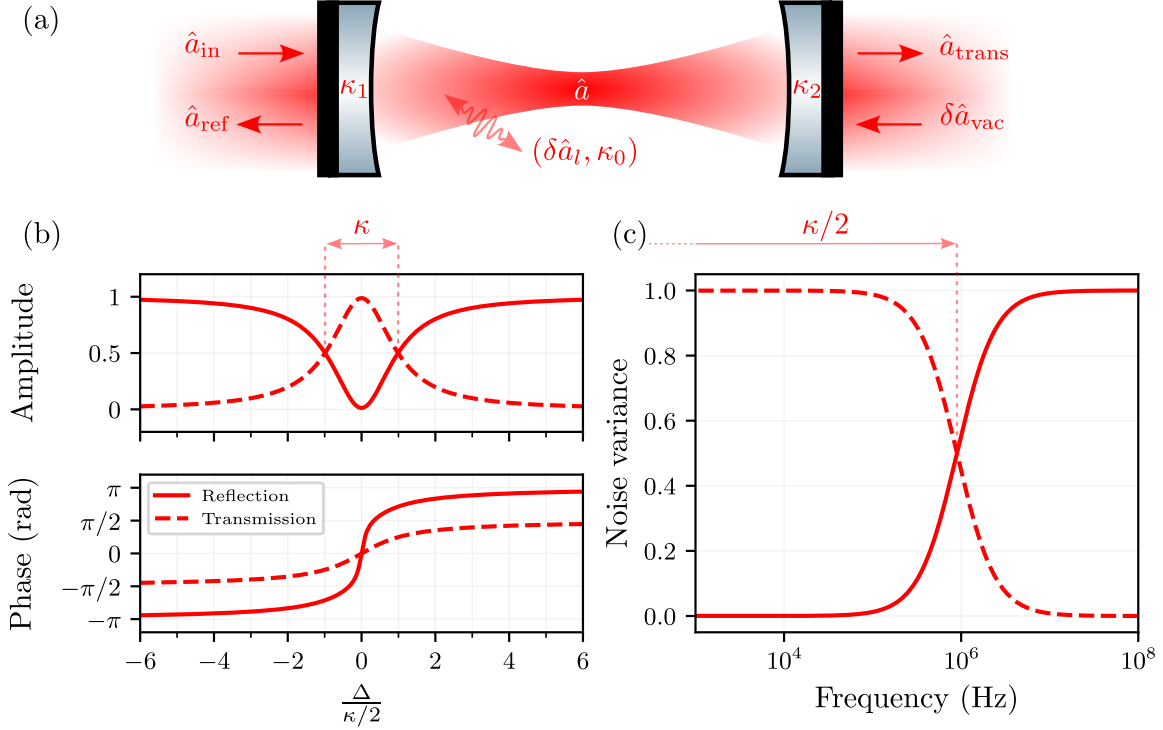


Fig. I.5 Filtering properties of optical cavities. (a) Cavity diagram and definitions. \hat{a} 's are the various fields at play. κ 's are the various couplings involved i.e. input and output mirrors, as well as intrinsic cavity cavity losses, with $\delta\hat{a}$'s the associated fluctuations. (b) Amplitude and phase response of an optical cavity as a function of the laser detuning (in cavity linewidth unit). In this case, both mirrors are identical ($\kappa_1 = \kappa_2$) and cavity losses are negligible ($\kappa_0 \ll \kappa_1$). (c) Transfer functions of the input classical noises as in (I.90)

Patching it up with the input-output formula this gives

$$\bar{\alpha}_{\text{ref}} = \left(\frac{\kappa_1}{\kappa/2 - i\Delta} - 1 \right) \bar{\alpha}_{\text{in}} \quad \bar{\alpha}_{\text{trans}} = \frac{\sqrt{\kappa_1 \kappa_2}}{(\kappa/2 - i\Delta)} \bar{\alpha}_{\text{in}}. \quad (\text{I.66})$$

The reflection and transmission coefficients are then

$$R(\Delta) = \left| \frac{\bar{\alpha}_{\text{ref}}}{\bar{\alpha}_{\text{in}}} \right|^2 = \frac{(\kappa_1 - \kappa/2)^2 + \Delta^2}{(\kappa/2)^2 + \Delta^2} \quad T(\Delta) = \left| \frac{\bar{\alpha}_{\text{trans}}}{\bar{\alpha}_{\text{in}}} \right|^2 = \frac{\kappa_1 \kappa_2}{(\kappa/2)^2 + \Delta^2}. \quad (\text{I.67})$$

The cavity linewidth (FWHM) is then given by $\kappa/2\pi$ (Hz), as illustrated in Fig I.5.(b). We will then refer to $\kappa/4\pi$ (HWHM) as the cavity bandwidth (Hz). Plugging back the expression

of $\kappa_i = T_i/\tau$ in the reflection coefficient, we have

$$R(\pm\infty) = 1 \quad R(0) = \left(\frac{T_1 - T_2 - \mathcal{L}}{T_1 + T_2 + \mathcal{L}} \right)^2 \quad (\text{I.68})$$

such that the relative depth of the resonance dip gives us information about the cavity losses and couplings. In particular, the resonance dip vanishes when $T_1 = T_2 + \mathcal{L}$, which is the so called *impedance matching* condition: no light is reflected at resonance and all of it is transmitted or lost. Similarly, the transmission coefficient reads

$$T(\pm\infty) = 0 \quad T(0) = \frac{4T_1 T_2}{(T_1 + T_2 + \mathcal{L})^2} \quad (\text{I.69})$$

We also define the cavity finesse \mathcal{F} , which is a measure of the sharpness of the resonance peaks relative to its FSR, as

$$\mathcal{F} = \frac{\omega_{\text{FSR}}}{\kappa} = \frac{\pi c}{L\kappa} = \frac{2\pi}{T_1 + T_2 + \mathcal{L}} \quad (\text{I.70})$$

which also gives the average number of round trips a photon makes before escaping the cavity i.e. $\langle n_{rt} \rangle = \mathcal{F}/\pi$. For a given cavity length (so same FSR), the higher the finesse, the longer the photon lifetime in the cavity κ^{-1} .

Measuring all these quantities then allows to fully characterize the cavity parameters T_1 , T_2 and \mathcal{L} . This is done by measuring the reflection and transmission coefficients at resonance and far from resonance, as well as the cavity linewidth (or finesse).

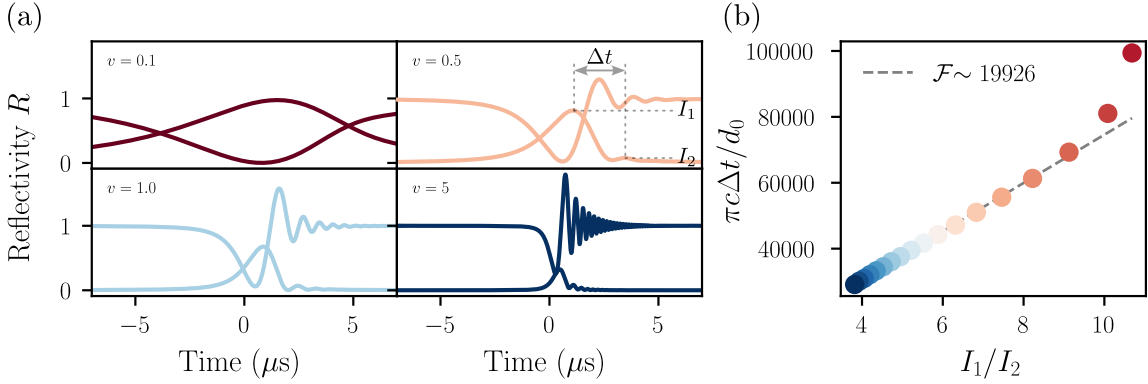
Mean field solution (Dynamical case):

We now let the detuning vary linearly in time, and express it in units of cavity bandwidth as $\Delta(t) = \Delta_0 + v \frac{\kappa^2}{2} t$ where we defined v as the sweep speed in units of cavity bandwidth per κ^{-1} . The intracavity field yields the standard differential equation

$$\dot{\bar{\alpha}}(t) = - \left(\frac{\kappa}{2} - i \left(\Delta_0 + \frac{v\kappa^2}{2} t \right) \right) \bar{\alpha}(t) + \sqrt{\kappa_1} \bar{\alpha}_{\text{in}} \quad (\text{I.71})$$

This is solved by the means of integration factor method, such that we find

$$\begin{aligned} \alpha(t) &= \exp \left[\left(-\frac{\kappa}{2} + i\Delta_0 \right) t + i \frac{v\kappa^2}{4} t^2 \right] \\ &\times \left[\alpha(0) + \sqrt{\kappa_1} \bar{\alpha}_{\text{in}} \int_0^t \exp \left(\left(\frac{\kappa}{2} - i\Delta_0 \right) s - i \frac{v\kappa^2}{4} s^2 \right) ds \right]. \end{aligned} \quad (\text{I.72})$$

Fig. I.6 $F \text{ sim} = 20000, L=2\text{e-}2$

This expression describes the transient response of the intracavity field as the detuning is swept through resonance. When scanning over the cavity resonance at a rate exceeding the cavity bandwidth, photons at various detuning start to build up in the cavity without reaching the steady state value. This results in a characteristic asymmetric lineshape, where these different *colored* photons start beating against each other, leading to oscillations in the transmitted and reflected intensities. This is illustrated in Fig I.5.(c) for different sweep speeds. The above does feature an analytical formula involving error functions erf, such that can either fit the data by performing a numerical integration or the analytical formula. However if the data array feature too few points numerical integration becomes numerically costly. [figure to do](#) .

The finesse-extraction procedure of Poirson *et al.* [3] can be expressed in our notation by identifying their cavity length d_0 with our L , and their bandwidth Ω_r with $\kappa/2$. In the fast-sweep regime—equivalent to our linear detuning sweep $\Delta(t) = \Delta_0 + v\Delta t$ —the transmitted intensity displays a sequence of maxima originating from the same interference mechanism responsible for the oscillatory behaviour in our analytical solution (Eq. (1.71)). Poirson *et al.* show that the time interval Δt between the first two transmitted maxima satisfies, near $\Delta t \simeq \tau$, the relation

$$\frac{\pi c}{L} \Delta t \simeq \frac{F}{e} \frac{I_1}{I_2}, \quad (\text{I.73})$$

which is their Eq. (21) rewritten using our notation. Since the intensity decay time is $\tau = 2/\kappa = FL/(\pi c)$, Eq. (I.73) links the measured ratio I_1/I_2 and the peak spacing Δt directly to the cavity finesse. This provides an experimentally simple and robust method to determine F , fully consistent with the dynamical intracavity-field model developed here.

Fluctuations solution: To derive the covariance matrix we go to Fourier space such that

$$\mathbf{M}_\Delta \delta \hat{\mathbf{a}}[\Omega] = \sqrt{\kappa_1} \delta \hat{\mathbf{a}}_{\text{in}}[\Omega] + \sqrt{\kappa_2} \delta \hat{\mathbf{a}}_{\text{vac}}[\Omega] + \sqrt{\kappa_0} \delta \hat{\mathbf{a}}_{\text{l}}[\Omega] \quad (\text{I.74})$$

with

$$\mathbf{M}_\Delta = \begin{pmatrix} \kappa/2 - i(\Delta + \Omega) & 0 \\ 0 & \kappa/2 + i(\Delta - \Omega) \end{pmatrix}$$

For notational convenience, we will drop the explicit dependence on Ω in the following. Inverting the above relation and plugging it in the input-output relations gives the reflected and transmitted fields as

$$\begin{aligned} \delta \hat{\mathbf{a}}_{\text{ref}} &= (\kappa_1 \mathbf{M}_\Delta^{-1} - \mathbf{1}) \delta \hat{\mathbf{a}}_{\text{in}} + \sqrt{\kappa_1} \mathbf{M}_\Delta^{-1} (\sqrt{\kappa_2} \delta \hat{\mathbf{a}}_{\text{vac}} + \sqrt{\kappa_0} \delta \hat{\mathbf{a}}_{\text{l}}) \\ \delta \hat{\mathbf{a}}_{\text{trans}} &= \sqrt{\kappa_2} \mathbf{M}_\Delta^{-1} (\sqrt{\kappa_1} \delta \hat{\mathbf{a}}_{\text{in}} + \sqrt{\kappa_0} \delta \hat{\mathbf{a}}_{\text{l}}) + (\kappa_2 \mathbf{M}_\Delta^{-1} - \mathbf{1}) \delta \hat{\mathbf{a}}_{\text{vac}} \end{aligned} \quad (\text{I.75})$$

where we can introduce the optical susceptibility χ_c such that the matrix \mathbf{M}_Δ^{-1} reads

$$\mathbf{M}_\Delta^{-1} = \begin{pmatrix} \chi_c[\Omega] & 0 \\ 0 & \chi_c^*[-\Omega] \end{pmatrix}, \quad \text{with} \quad \chi_c[\Omega] = \frac{1}{\kappa/2 - i(\Delta + \Omega)}$$

and with the same convention than that of the Fourier transform i.e. the two photon conjugate is a complex conjugation and a frequency inversion, we note that $[\chi_c[0]]^\dagger = \chi_c^*[0]$ such that the \mathbf{M}_Δ matrices are diagonal on resonance. Using $\delta \hat{\mathbf{a}} = \mathbf{\Gamma}^{-1} \delta \hat{\mathbf{u}}$ the reflected and transmitted quadratures read

$$\begin{aligned} \delta \hat{\mathbf{u}}_{\text{ref}} &= (\kappa_1 \mathbf{\Gamma} \mathbf{M}_\Delta^{-1} \mathbf{\Gamma}^{-1} - \mathbf{1}) \delta \hat{\mathbf{u}}_{\text{in}} + \sqrt{\kappa_1} \mathbf{\Gamma} \mathbf{M}_\Delta^{-1} \mathbf{\Gamma}^{-1} (\sqrt{\kappa_2} \delta \hat{\mathbf{u}}_{\text{vac}} + \sqrt{\kappa_0} \delta \hat{\mathbf{u}}_{\text{l}}) \\ \delta \hat{\mathbf{u}}_{\text{trans}} &= \sqrt{\kappa_2} \mathbf{\Gamma} \mathbf{M}_\Delta^{-1} \mathbf{\Gamma}^{-1} (\sqrt{\kappa_1} \delta \hat{\mathbf{u}}_{\text{in}} + \sqrt{\kappa_0} \delta \hat{\mathbf{u}}_{\text{l}}) + (\kappa_2 \mathbf{\Gamma} \mathbf{M}_\Delta^{-1} \mathbf{\Gamma}^{-1} - \mathbf{1}) \delta \hat{\mathbf{u}}_{\text{vac}} \end{aligned} \quad (\text{I.76})$$

where the matrix product above reads

$$\mathbf{\Gamma} \mathbf{M}_\Delta^{-1} \mathbf{\Gamma}^{-1} = \frac{1}{(\kappa/2 - i\Omega)^2 + \Delta^2} \begin{pmatrix} \kappa/2 - i\Omega & -\Delta \\ \Delta & \kappa/2 - i\Omega \end{pmatrix}.$$

The structure above is the engine behind frequency-dependent squeezing. On resonance, we have

$$\mathbf{M}_0^{-1} = \frac{1}{\kappa/2 - i\Omega} \mathbf{I} \implies \mathbf{\Gamma} \mathbf{M}_0^{-1} \mathbf{\Gamma}^{-1} = \frac{1}{\kappa/2 - i\Omega} \mathbf{I}$$

causing symmetric sidebands around the carrier to be filtered identically both in amplitude and phase — so the quadrature along which these sidebands are correlated (if considering squeezed correlations) remains the same at all frequencies. The moment the cavity is detuned, the $\mathbf{\Gamma} \mathbf{M}_\Delta^{-1} \mathbf{\Gamma}^{-1}$ off-diagonal terms asymmetrically mix the upper and lower sidebands;

in the two-photon picture this is a frequency-dependent rotation and scaling of the (p, q) basis. The amplitude (Lorentzian) part sets how strongly each sideband passes, while the phase accrued inside the cavity sets the rotation angle that now varies with Ω . A broadband field with a single squeezing angle at the input is therefore converted into an output whose squeezing angle “twists” with frequency: near one band it can align with the phase quadrature, and at another it can align with the amplitude quadrature. This is exactly the mechanism exploited by filter cavities in precision interferometry: by choosing bandwidth, detuning, and coupling, one tailors the rotation profile to the target noise crossover. Practically, the attainable rotation and the preserved squeezing are limited by optical loss and mode mismatch, which inject uncorrelated vacuum and partially unwind the correlations the detuned cavity imprints on sidebands.

Note: On resonance ($\Delta = 0$), the output quadratures can then be written as

$$\begin{aligned}\delta\hat{\mathbf{u}}_{\text{ref}} &= \frac{\kappa_1 - \kappa/2 + i\Omega}{\kappa/2 - i\Omega} \delta\hat{\mathbf{u}}_{\text{in}} + \frac{\sqrt{\kappa_1\kappa_2}}{\kappa/2 - i\Omega} \delta\hat{\mathbf{u}}_{\text{vac}} + \frac{\sqrt{\kappa_1\kappa_0}}{\kappa/2 - i\Omega} \delta\hat{\mathbf{u}}_{\text{l}} \\ \delta\hat{\mathbf{u}}_{\text{trans}} &= \frac{\sqrt{\kappa_1\kappa_2}}{\kappa/2 - i\Omega} \delta\hat{\mathbf{u}}_{\text{in}} + \frac{\kappa_2 - \kappa/2 + i\Omega}{\kappa/2 - i\Omega} \delta\hat{\mathbf{u}}_{\text{vac}} + \frac{\sqrt{\kappa_2\kappa_0}}{\kappa/2 - i\Omega} \delta\hat{\mathbf{u}}_{\text{l}}\end{aligned}\quad (\text{I.77})$$

and their noise spectra are

$$\begin{aligned}\mathbf{S}_{\text{ref}}[\Omega] &= \frac{(\kappa_1 - \kappa/2)^2 + \Omega^2}{(\kappa/2)^2 + \Omega^2} \mathbf{S}_{\text{in}} + \frac{\kappa_1}{(\kappa/2)^2 + \Omega^2} (\kappa_0 \mathbf{1} + \kappa_2 \mathbf{1}) \\ \mathbf{S}_{\text{trans}}[\Omega] &= \frac{(\kappa_2 - \kappa/2)^2 + \Omega^2}{(\kappa/2)^2 + \Omega^2} \mathbf{1} + \frac{\kappa_2}{(\kappa/2)^2 + \Omega^2} (\kappa_0 \mathbf{1} + \kappa_1 \mathbf{S}_{\text{in}})\end{aligned}\quad (\text{I.78})$$

where the vacuum and loss covariance matrices are equal to $\mathbf{1}$. As these two vacua sum up linearly, it is equivalent to consider a single vacuum with an effective decay rate $\kappa_2 + \kappa_0 \rightarrow \kappa_2$ to lighten the notation. We then absorb intrinsic losses into the output coupler, and consider only two ports: the input coupler with decay rate κ_1 and the output coupler with decay rate κ_2 . We stress that this substitution is only valid when considering the **reflected** quadratures. When focusing on the transmitted quadratures, one can perform a similar redefinition with κ_1 i.e. $\kappa_1 + \kappa_0 \rightarrow \kappa_1$.

Transfer matrices and Spectra: Expressing the reflected and transmitted quadratures in matrix form yields

$$\begin{aligned}\delta\hat{\mathbf{u}}_{\text{ref}} &= \mathbf{T}_{\text{ref}} \delta\hat{\mathbf{u}}_{\text{in}} + \mathbf{L}_{\text{ref}} \delta\hat{\mathbf{u}}_{\text{vac}} \\ \delta\hat{\mathbf{u}}_{\text{trans}} &= \mathbf{T}_{\text{trans}} \delta\hat{\mathbf{u}}_{\text{in}} + \mathbf{L}_{\text{trans}} \delta\hat{\mathbf{u}}_{\text{vac}}\end{aligned}\quad (\text{I.79})$$

where the transfer matrices for the input and loss ports given by

$$\begin{aligned}\mathbf{T}_{\text{ref}} &= \kappa_1 \mathbf{\Gamma} \mathbf{M}_{\Delta}^{-1} \mathbf{\Gamma}^{-1} - \mathbf{1}, & \mathbf{L}_{\text{ref}} &= \sqrt{\kappa_1 \kappa_2} \mathbf{\Gamma} \mathbf{M}_{\Delta}^{-1} \mathbf{\Gamma}^{-1} \\ \mathbf{T}_{\text{trans}} &= \sqrt{\kappa_1 \kappa_2} \mathbf{\Gamma} \mathbf{M}_{\Delta}^{-1} \mathbf{\Gamma}^{-1}, & \mathbf{L}_{\text{trans}} &= \kappa_2 \mathbf{\Gamma} \mathbf{M}_{\Delta}^{-1} \mathbf{\Gamma}^{-1} - \mathbf{1}\end{aligned}$$

Conveniently, we introduce the complex reflectivities and transmissivities experienced by the sideband fields as

$$r_{\Delta}[\Omega] = \kappa_1 \chi_c[\Omega] - 1, \quad r'_{\Delta}[\Omega] = \kappa_2 \chi_c[\Omega] - 1, \quad t_{\Delta}[\Omega] = \sqrt{\kappa_1 \kappa_2} \chi_c[\Omega] \quad (\text{I.80})$$

Here we introduced two different reflection coefficients: $r_{\Delta}[\Omega]$ for the input coupler, and $r'_{\Delta}[\Omega]$ for the output coupler describing the reflection of the incoming field fluctuations on each port. The transmission coefficient $t_{\Delta}[\Omega]$ is the same for both ports since it describes the field fluctuations transmitted from one port to the other, no matter what the direction of propagation is. We can now define the modulus and phase of the positive and negative sideband reflectivities and transmissivities as

$$\begin{aligned}r_+ e^{i\phi_+} &= r_{\Delta}[\Omega], & r_- e^{-i\phi_-} &= r_{\Delta}^*[-\Omega] \\ r'_+ e^{i\phi'_+} &= r'_{\Delta}[\Omega], & r'_- e^{-i\phi'_-} &= r'^*_{\Delta}[-\Omega] \\ t_+ e^{i\theta_+} &= t_{\Delta}[\Omega], & t_- e^{-i\theta_-} &= t_{\Delta}^*[-\Omega]\end{aligned} \quad (\text{I.81})$$

describing the amplitude filtering and dephasing underwent by a sideband at Ω and its two-photon conjugate in both reflection and transmission. The output quadrature transfer matrices can then be expressed as

$$\mathbf{T}_{\text{ref}} = \mathbf{\Gamma} \begin{pmatrix} r_+ e^{i\phi_+} & 0 \\ 0 & r_- e^{-i\phi_-} \end{pmatrix} \mathbf{\Gamma}^{-1} \quad \text{and} \quad \mathbf{L}_{\text{ref}} = \mathbf{\Gamma} \begin{pmatrix} t_+ e^{i\theta_+} & 0 \\ 0 & t_- e^{-i\theta_-} \end{pmatrix} \mathbf{\Gamma}^{-1}$$

and in transmission as

$$\mathbf{T}_{\text{trans}} = \mathbf{\Gamma} \begin{pmatrix} t_+ e^{i\theta_+} & 0 \\ 0 & t_- e^{-i\theta_-} \end{pmatrix} \mathbf{\Gamma}^{-1} \quad \text{and} \quad \mathbf{L}_{\text{trans}} = \mathbf{\Gamma} \begin{pmatrix} r'_+ e^{i\phi'_+} & 0 \\ 0 & r'_- e^{-i\phi'_-} \end{pmatrix} \mathbf{\Gamma}^{-1}$$

We use the usual transformation for the positive and negative sideband reflectivities as

$$\begin{aligned}\bar{r} &= \frac{r_+ + r_-}{2}, & \delta r &= \frac{r_+ - r_-}{2} \\ \bar{\phi} &= \frac{\phi_+ + \phi_-}{2}, & \delta\phi &= \frac{\phi_+ - \phi_-}{2}\end{aligned} \quad (\text{I.82})$$

to finally write the reflected quadrature transfer matrices as

$$\mathbf{T}_{\text{ref}} = e^{i\delta\phi} \mathbf{R}(-\bar{\phi}) \left(\bar{r} \mathbf{1} + i \delta r \mathbf{R}(\pi/2) \right) \quad \text{and} \quad \mathbf{L}_{\text{ref}} = e^{i\delta\theta} \mathbf{R}(-\bar{\theta}) \left(\bar{t} \mathbf{1} + i \delta t \mathbf{R}(\frac{\pi}{2}) \right) \quad (\text{I.83})$$

as well as the transmitted quadrature transfer matrices

$$\mathbf{T}_{\text{trans}} = e^{i\delta\theta} \mathbf{R}(-\bar{\theta}) \left(\bar{t} \mathbf{1} + i \delta t \mathbf{R}(\frac{\pi}{2}) \right) \quad \text{and} \quad \mathbf{L}_{\text{trans}} = e^{i\delta\phi} \mathbf{R}(-\bar{\phi}) \left(\bar{r}' \mathbf{1} + i \delta r' \mathbf{R}(\frac{\pi}{2}) \right) \quad (\text{I.84})$$

such that the covariance matrices for the reflected and transmitted quadratures of a detuned cavity are given by

$$\begin{aligned} \mathbf{S}_{\text{ref}}[\Omega] &= \mathbf{T}_{\text{ref}} \mathbf{S}_{\text{in}} \mathbf{T}_{\text{ref}}^\dagger + \mathbf{L}_{\text{ref}} \mathbf{L}_{\text{ref}}^\dagger \\ \mathbf{S}_{\text{trans}}[\Omega] &= \mathbf{T}_{\text{trans}} \mathbf{S}_{\text{in}} \mathbf{T}_{\text{trans}}^\dagger + \mathbf{L}_{\text{trans}} \mathbf{L}_{\text{trans}}^\dagger \end{aligned} \quad (\text{I.85})$$

$$\mathbf{T}_r[\Omega] = \boldsymbol{\Gamma} \mathbf{r}_\Delta[\Omega] \boldsymbol{\Gamma}^{-1} = \frac{1}{2} \begin{pmatrix} r_+ e^{i\phi_+} + r_- e^{-i\phi_-} & i(r_+ e^{i\phi_+} - r_- e^{-i\phi_-}) \\ -i(r_+ e^{i\phi_+} - r_- e^{-i\phi_-}) & r_+ e^{i\phi_+} + r_- e^{-i\phi_-} \end{pmatrix} \quad (\text{I.86})$$

and similarly for the one photon transmission matrix

$$\mathbf{t}_\Delta[\Omega] = \sqrt{\kappa_1 \kappa_2} \mathbf{M}_\Delta^{-1} = \begin{pmatrix} t_\Delta[\Omega] & 0 \\ 0 & t_\Delta^*[-\Omega] \end{pmatrix} \quad \text{with} \quad t_\Delta[\Omega] = \frac{\sqrt{\kappa_1 \kappa_2}}{\kappa/2 - i(\Delta + \Omega)} \quad (\text{I.87})$$

such that

$$\mathbf{T}_t[\Omega] = \boldsymbol{\Gamma} \mathbf{t}_\Delta[\Omega] \boldsymbol{\Gamma}^{-1} = \frac{1}{2} \begin{pmatrix} t_\Delta[\Omega] + t_\Delta^*[-\Omega] & i(t_\Delta[\Omega] - t_\Delta^*[-\Omega]) \\ -i(t_\Delta[\Omega] - t_\Delta^*[-\Omega]) & t_\Delta[\Omega] + t_\Delta^*[-\Omega] \end{pmatrix} \quad (\text{I.88})$$

Example 1: Mode Cleaner

Let us consider a configuration such that $\kappa_1 = \kappa_2 \approx \kappa/2$ where we assume negligible losses $\kappa_0 \ll \kappa_{1,2}$. It represents a cavity where the input and output mirror transmittivities are equal, and we set the laser resonant to the cavity ($\Delta = 0$), such that the transmitted quadratures are written

$$\delta \hat{\mathbf{u}}_{\text{trans}}[\Omega] = \frac{\kappa/2}{\kappa/2 - i\Omega} \delta \hat{\mathbf{u}}_{\text{in}}[\Omega] + \frac{i\Omega}{\kappa/2 - i\Omega} \delta \hat{\mathbf{u}}_{\text{vac}}[\Omega]. \quad (\text{I.89})$$

The resulting transmitted quadrature covariance matric is given by:

$$\mathbf{S}_{\text{trans}}[\Omega] = \frac{(\kappa/2)^2}{(\kappa/2)^2 + \Omega^2} \mathbf{S}_{\text{in}} + \frac{\Omega^2}{(\kappa/2)^2 + \Omega^2} \mathbf{1} \quad (\text{I.90})$$

Now consider that the input fluctuations are above those of vacuum i.e. the input field features classical noise. We would then have $S_{pp}^{\text{in}} > S_{pp}^{\text{vac}} = 1$ and $S_{qq}^{\text{in}} > S_{qq}^{\text{vac}} = 1$. One can notice that the prefactor to the input noises is a Lorentzian function - a low pass filter. Hence, the noises of the input fields are low pass filtered by the cavity, while the vacuum fluctuations are high pass filtered at precisely the same cutoff $\kappa/2$. The mean field of the *bright* coherent input is fully transmitted, but its super-vacuum fluctuations, potentially classically modulated, are filtered by the cavity. Taking a high finesse cavity such that the cutoff frequency is low, the transmitted field now features vacuum sidebands: it has been *cleaned* from classical noise. This is the principle of a *mode cleaner* cavity, which is used in many precision experiments to provide a spectrally pure laser field, as well as a spatially filtered beam such that the transmitted beam is a pure TEM₀₀.

Example 2: Detuned single port cavity

We now consider a lossless single port cavity with $\kappa_2 = 0$ and $\kappa_1 = \kappa$. the transfer matrix for the reflected **field** then reads

$$\kappa \mathbf{M}_\Delta^{-1} - \mathbf{1} = \begin{pmatrix} \frac{\kappa/2 + i(\Delta + \Omega)}{\kappa/2 - i(\Delta + \Omega)} & 0 \\ 0 & \frac{\kappa/2 - i(\Delta - \Omega)}{\kappa/2 + i(\Delta - \Omega)} \end{pmatrix}$$

where we see that the upper and lower sidebands are reflected with different amplitude ρ_+ and ρ_- and phase shifts ϕ_+ and ϕ_- when the cavity is detuned ($\Delta \neq 0$). We then have :

$$\rho_+ = \left| \frac{\kappa/2 + i(\Delta + \Omega)}{\kappa/2 - i(\Delta + \Omega)} \right| = 1, \quad \rho_- = \left| \frac{\kappa/2 - i(\Delta - \Omega)}{\kappa/2 + i(\Delta - \Omega)} \right| = 1 \quad (\text{I.91})$$

$$\phi_+[\Omega] = 2 \arctan \left(\frac{\Delta + \Omega}{\kappa/2} \right), \quad \phi_-[\Omega] = 2 \arctan \left(\frac{\Delta - \Omega}{\kappa/2} \right) \quad (\text{I.92})$$

such that we can define the overall and differential phase shifts as

$$\bar{\phi}[\Omega] = \phi_+[\Omega] + \phi_-[\Omega] = \arctan \frac{4\Omega\kappa}{(\frac{\kappa}{2})^2 + \Delta^2 - \Omega^2} \quad \Delta\phi[\Omega] = \phi_+[\Omega] - \phi_-[\Omega] = \arctan \frac{4\Delta\kappa}{(\frac{\kappa}{2})^2 - \Delta^2 + \Omega^2} \quad (\text{I.93})$$

In the two-photon formalism, this asymmetric phase shift translates into a frequency-dependent rotation of the quadratures.

The transfer matrix is expressed as

$$\mathbf{T}_r[\Omega] = \frac{1}{(\kappa/2 - i\Omega)^2 + \Delta^2} \begin{pmatrix} (\kappa/2)^2 - \Delta^2 + \Omega^2 & -\kappa\Delta \\ +\kappa\Delta & (\kappa/2)^2 - \Delta^2 + \Omega^2 \end{pmatrix} \quad (I.94)$$

$$\kappa\Gamma\mathbf{M}_\Delta^{-1}\Gamma^{-1} - \mathbf{1} = \frac{1}{(\kappa/2 - i\Omega)^2 + \Delta^2} \begin{pmatrix} (\kappa/2)^2 - \Delta^2 + \Omega^2 & -\kappa\Delta \\ +\kappa\Delta & (\kappa/2)^2 - \Delta^2 + \Omega^2 \end{pmatrix}$$

such that the covariance matrix is given by

$$\mathbf{S}_{\text{ref}}[\Omega] = \begin{pmatrix} S_{pp}^{\text{ref}}[\Omega] & S_{pq}^{\text{ref}}[\Omega] \\ S_{qp}^{\text{ref}}[\Omega] & S_{qq}^{\text{ref}}[\Omega] \end{pmatrix} \quad (I.95)$$

where we won't write the full expressions of the matrix elements for brevity. The key point is that the off-diagonal terms are non zero, meaning that the reflected quadratures are correlated. This is the frequency-dependent rotation mechanism described above.

This configuration is used in our experiment to measure the squeezing spectrum of the OPO, as the

I.2.5 Non Linear Cavities

We now turn to the description of optical cavities in which a $\chi^{(2)}$ medium is embedded within. This non linear medium can be used both for sum frequency generation, or difference frequency generation. The generic Hamiltonian describing a degenerate $\chi^{(2)}$ parametric process is

$$H = \hbar\omega_p \hat{b}^\dagger \hat{b} + \hbar\omega_0 \hat{a}^\dagger \hat{a} + \frac{i\hbar\epsilon}{2} (\hat{b} \hat{a}^\dagger 2 - \hat{b}^\dagger \hat{a}^2) \quad (I.96)$$

where we assumed perfect phase matching for simplicity, that is $\epsilon \in \mathbb{R}$. In our experiment with squeezed light, we do use both as to first generate a pump field using a Second Harmonic Generation (SHG) scheme, then use the generated field to *pump* a degenerate Optical Parametric Oscillator (OPO). The equations of motion of both fields are very similar in their structure, yet different in their phenomenology. Here we outline the main results and predictions for both.

Second Harmonic Generation

The SHG scheme consists in shining a laser field at frequency ω_0 onto the cavity, and the non linear medium generates a field at frequency $\omega_p = 2\omega_0$, that is, two photons at ω_0 described by operator \hat{a} , are converted into a single photon at ω_p described by operator \hat{b} . The input

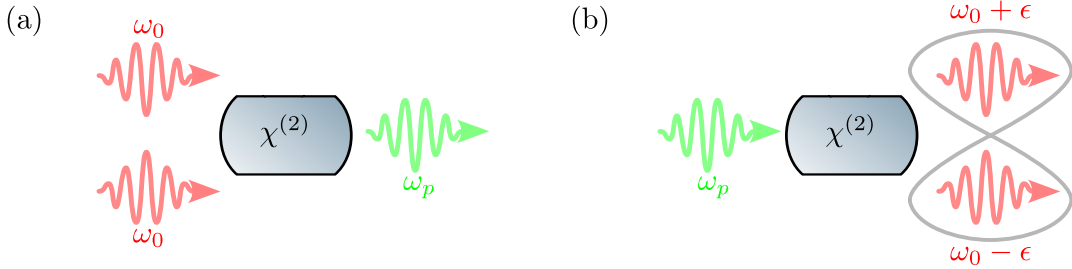


Fig. I.7 Diagrams of $\chi^{(2)}$ non linear processes. (a) Second Harmonic Generation ($2\omega_0 = \omega_p$). (b) Parametric Down Conversion. The outgoing photons are entangled.

field is thus \hat{a}_{in} at ω_0 , while the input fields at ω_p are vacua $\hat{b}_{\text{in}} = \delta b_l = \delta \hat{b}_{\text{vac}}$. We restrain the theoretical description to our experiment, where the end mirror reflectivity is ~ 1 for our generated green beam, as seen in the figure below $\kappa_{2,b} = 0$. We will not derive the noise spectra for this scheme as they are not of interest in this work, displaying standard vacuum type fluctuations in both the pump and second harmonic field.

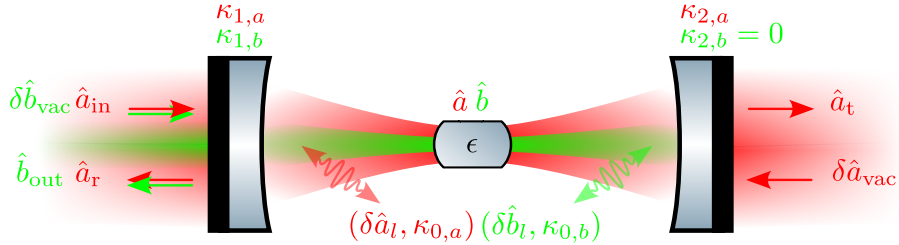


Fig. I.8 Cavity diagram for the Second Harmonic Generation. \hat{a} 's are the various fields at play, κ 's are the various couplings involved, with $\delta\hat{a}$'s the associated fluctuations, similar as in Fig I.4, now considering both the infrared pump, and the generated green beam.

We rather focus on the mean field solution. The scalar part of the QLE on resonance for both fields are given by

$$\begin{aligned} 0 &= -\frac{\kappa_a}{2} \bar{\alpha} + \epsilon \bar{\alpha}^* \bar{\beta} + \sqrt{\kappa_{1,a}} \bar{\alpha}_{\text{in}}, \\ 0 &= -\frac{\kappa_b}{2} \bar{\beta} + \frac{\epsilon}{2} \bar{\alpha}^2. \end{aligned} \tag{I.97}$$

where subscript a and b refer to the ω_0 and ω_p fields respectively. Solving for the $\bar{\beta}$ field and computing the output field $\bar{\beta}_{\text{out}}$ from the input mirror using the input-output relations,

yields an output intensity of

$$|\bar{\beta}_{\text{out}}|^2 = \frac{\kappa_a^2 \kappa_{1,b}^2}{4 \varepsilon^2} \left[\left(1 + \frac{108 \varepsilon^2 \kappa_{1,a}}{\kappa_a^3 \kappa_b} |\bar{\alpha}_{\text{in}}|^2 \left(1 + \sqrt{1 + \frac{\kappa_a^3 \kappa_b}{54 \varepsilon^2 \kappa_{1,a} |\bar{\alpha}_{\text{in}}|^2}} \right) \right)^{1/6} - \left(1 + \frac{108 \varepsilon^2 \kappa_{1,a}}{\kappa_a^3 \kappa_b} |\bar{\alpha}_{\text{in}}|^2 \left(1 + \sqrt{1 + \frac{\kappa_a^3 \kappa_b}{54 \varepsilon^2 \kappa_{1,a} |\bar{\alpha}_{\text{in}}|^2}} \right) \right)^{-1/6} \right]^4. \quad (\text{I.98})$$

This cumbersome expression can be simplified in two limits. In the low input power limit, the output power scales quadratically with the input power, whereas at high powers it scales as $|\alpha_{\text{in}}|^{4/3}$.

Pseudo linear behaviour: For intermediate powers, the output power scales almost linearly with the input power, which is precisely the regime in which we will operate. The crossover between these regimes is set by the non linear gain ϵ and the cavity decay rates $\kappa_{a,b}$.

Optical Parametric Oscillation & Amplification

For this scheme, we consider a pump field with frequency $\omega_p = 2\omega_0$. A first key difference from the SHG scheme can be highlighted by the fact that we are now pumping at $2\omega_0$, such that pairs of entangled photons are generated at $\omega_0 + \epsilon$ and $\omega_0 - \epsilon$, with ϵ a sideband frequency allowed by the cavity bandwidth, hence conserving energy.

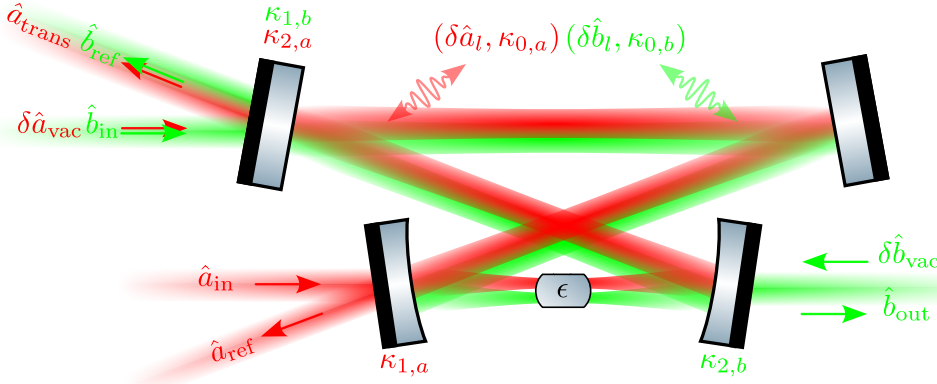


Fig. I.9 Cavity diagram for the Optical Parametric Oscillator. \hat{a} 's are the various fields at play, κ 's are the various couplings involved, with $\delta\hat{a}$'s the associated fluctuations, similar as in Fig I.4, now considering both the green pump, and the generated infrared squeezed beam. The beams are shifted for illustrative purposes but share the same optical axis in the experiment.

We further consider the pump is not *depleted*, such that we can change \hat{b} to its mean field value $|\bar{\beta}|e^{i\bar{\varphi}_b}$, and we disregard the \hat{b} fluctuations in the equations of motion for simplicity. A careful and complete derivations could also be carried out by keeping all terms in the equations of motion, but it is not serving our purpose here so we will these assumptions to lighten the notation. The total non linear gain is defined as $g = \epsilon|\bar{\beta}|$, and the QLEs for the steady state and fluctuation parts of the \hat{a} field yields:

$$\begin{cases} 0 = -\left(\frac{\kappa}{2} - i\Delta\right)\bar{\alpha} + ge^{i\bar{\varphi}_b}\bar{\alpha}^* + \sqrt{\kappa_1}\bar{\alpha}_{\text{in}} \\ \delta\dot{\hat{a}}(t) = -\begin{pmatrix} \kappa/2 - i\Delta & -ge^{i\bar{\varphi}_b} \\ -ge^{-i\bar{\varphi}_b} & \kappa/2 + i\Delta \end{pmatrix}\delta\hat{a}(t) + \sqrt{\kappa_1}\delta\hat{a}_{\text{in}}(t) + \sqrt{\kappa_2}\delta\hat{a}_{\text{vac}}(t) \end{cases} \quad (\text{I.99})$$

Mean field solution (Static case): Assuming a real input field $\bar{\alpha}_{\text{in}} = |\bar{\alpha}_{\text{in}}|$, the transmitted field is given by:

$$\bar{\alpha}_{\text{t}} = \frac{\sqrt{\kappa_1\kappa_2}}{\kappa/2} \frac{1 + i\frac{\Delta}{\kappa/2} + xe^{i\bar{\varphi}_b}}{1 + \left(\frac{\Delta}{\kappa/2}\right)^2 - |x|^2} |\bar{\alpha}_{\text{in}}| \quad (\text{I.100})$$

where we define the normalised pump parameter $x = 2g/\kappa \in \mathbb{R}$. This normalised pump parameter also equals the ratio of the pump field amplitude by the pump field threshold often written B/B_{thr} . For a resonant cavity, the expression reduces to the well known parametric amplification/deamplification scheme

$$\bar{\alpha}_{\text{t}} = \frac{\sqrt{\kappa_1\kappa_2}}{\kappa/2} \frac{1 + xe^{i\bar{\varphi}_b}}{1 - |x|^2} |\bar{\alpha}_{\text{in}}| \quad (\text{I.101})$$

in which the amplification or deamplification processes are set by the phase of the pump $\bar{\varphi}_b$. In the absence of a non linear medium $x = 0$ we recover the standard cavity results shown above. The threshold is defined at $x = 1$, where the rate of generation of entangled pairs exceeds the rate at which they leak from the cavity. In other words, x is unity when the round trip gain equals the round trip losses. That's precisely the point where the no depletion approximation breaks down, as illustrated by the divergence seen in transmitted field at this very value (how could one obtain a diverging field from a pump field with a finite number of photons). We also notice two special cases, when $\bar{\varphi}_b = \{0, \pi\}$, coinciding with the amplification and the deamplification processes respectively.

Fluctuations solution: The general expression of the QLE in Fourier space is given by

$$\tilde{\mathbf{M}}_{\Delta} \delta\hat{\mathbf{a}}[\Omega] = \sqrt{\kappa_1} \delta\hat{\mathbf{a}}_{\text{in}}[\Omega] + \sqrt{\kappa_2} \delta\hat{\mathbf{a}}_{\text{vac}}[\Omega] \quad (\text{I.102})$$

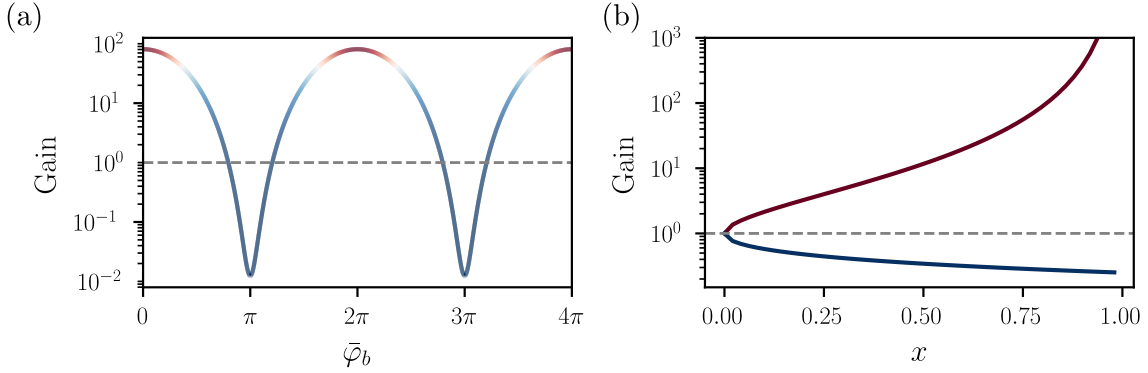


Fig. I.10 *add pump phase colorbar* Classical amplification-deamplification of an infrared seed in an Optical Parametric Oscillator below threshold. (a) Gain of the infrared seed as a function of the green pump phase. The color variations correspond to the pump phase. (b) Amplification-Deamplification of an infrared seed as a function of the normalized pump parameter x (< 1). The colors correspond to the ones on figure (a) (its extremes).

with

$$\tilde{\mathbf{M}}_{\Delta} = \begin{pmatrix} \kappa/2 - i(\Delta + \Omega) & -ge^{i\bar{\varphi}_b} \\ -ge^{-i\bar{\varphi}_b} & \kappa/2 + i(\Delta - \Omega) \end{pmatrix}$$

where we defined $\tilde{\mathbf{M}}_{\Delta}$ to not be confused with the matrix \mathbf{M}_{Δ} defined earlier for a simple cavity. Note that a genuine *frequency dependent* squeezing angle could be obtained by detuning the OPO cavity, but the frequency range over which the squeezing angle varies is limited by the cavity bandwidth, which is typically small compared to the frequency range of interest in our experiment. This phenomenon was realised experimentally few years ago [Vahlbruch2006], but is not the focus of our work.

In the context of our work, we will assume :

- the pump phase is locked to $\bar{\varphi}_b = \{0, \pi\}$ i.e. amplification or deamplification regime,
- the cavity is resonant $\Delta = 0$,

We further normalise all frequencies to the cavity bandwidth $\kappa/2$ such that $\Omega \rightarrow \Omega/(\kappa/2)$ and $g \rightarrow g/(\kappa/2) = x$, such that the off diagonal terms below can simply be written $\mp x$ factoring out the cavity bandwidth. We carry out the derivation for $\bar{\varphi}_b = 0$ (amplification) for simplicity, and the $\bar{\varphi}_b = \pi$ (deamplification) case is obtained by changing x to $-x$ in the final expressions. The matrix QLE in Fourier space is written as

$$\tilde{\mathbf{M}}_0 \delta \hat{\mathbf{a}}[\Omega] = \sqrt{\kappa_1} \delta \hat{\mathbf{a}}_{\text{in}}[\Omega] + \sqrt{\kappa_2} \delta \hat{\mathbf{a}}_{\text{vac}}[\Omega] \quad (\text{I.103})$$

with

$$\tilde{\mathbf{M}}_0 = \frac{\kappa}{2} \begin{pmatrix} 1 - i\frac{\Omega}{\kappa/2} & -x \\ -x & 1 - i\frac{\Omega}{\kappa/2} \end{pmatrix}$$

Transfer matrices and Spectra: As before with a simple cavity, the transmitted quadratures at resonance are then

$$\delta\hat{\mathbf{u}}_{\text{OPO}}[\Omega] = \mathbf{T}_{\text{OPO}}[\Omega]\delta\hat{\mathbf{u}}_{\text{in}}[\Omega] + \mathbf{L}_{\text{OPO}}[\Omega]\delta\hat{\mathbf{u}}_{\text{vac}}[\Omega] \quad (\text{I.104})$$

where we defined the transfer matrices for the input and loss ports as

$$\mathbf{T}_{\text{OPO}}[\Omega] = \sqrt{\kappa_1\kappa_2}\mathbf{\Gamma}\tilde{\mathbf{M}}_0^{-1}\mathbf{\Gamma}^{-1}, \quad \mathbf{L}_{\text{OPO}}[\Omega] = \kappa_2\mathbf{\Gamma}\tilde{\mathbf{M}}_0^{-1}\mathbf{\Gamma}^{-1} - \mathbf{1}....$$

After a bit of algebra, the covariance matrix of the transmitted field at $\bar{\varphi}_b = 0$ is then computed as

$$\mathbf{S}_{\text{OPO}}^0[\Omega] = \begin{pmatrix} 1 + \frac{\kappa_2}{\kappa} \frac{4x}{(1-x)^2 + \left(\frac{\Omega}{\kappa/2}\right)^2} & 0 \\ 0 & 1 - \frac{\kappa_2}{\kappa} \frac{4x}{(1+x)^2 + \left(\frac{\Omega}{\kappa/2}\right)^2} \end{pmatrix} \quad (\text{I.105})$$

On a side note, when deriving the noise spectra for the intracavity field, the maximum amount of squeezing is limited to 3dB, while the transmitted field can feature arbitrarily high squeezing levels. This is interpreted as additional correlations between vacuum fluctuations being reflected at the output port of the OPO and the squeezed field leaking from this very same output port, allowing for strong squeezing.

The perfect squeezer: Starting from (I.105), in the idealized limit of perfect escape efficiency ($\eta_{\text{esc}} = 1$) and for analysis frequencies much smaller than the cavity bandwidth ($\Omega/\kappa \rightarrow 0$), the expression simplifies to

$$\mathbf{S}_{\text{OPO}}^0[\Omega] = \begin{pmatrix} \frac{(1+x)^2}{(1-x)^2} & 0 \\ 0 & \frac{(1-x)^2}{(1+x)^2} \end{pmatrix} \quad (\text{I.106})$$

Introducing the standard squeezing parameter r through the relation $x = \tanh \frac{r}{2}$, one can

rewrite the numerator and denominator as

$$1 + \tanh \frac{r}{2} = \frac{e^{+\frac{r}{2}}}{\cosh \frac{r}{2}}, \quad 1 - \tanh \frac{r}{2} = \frac{e^{-\frac{r}{2}}}{\cosh \frac{r}{2}},$$

such that

$$\frac{(1 \pm \tanh \frac{r}{2})^2}{(1 \mp \tanh \frac{r}{2})^2} = \left(\frac{e^{\pm \frac{r}{2}}}{e^{\mp \frac{r}{2}}} \right)^2 = e^{\pm 2r}.$$

Thus when $\bar{\varphi}_b = \{0, \pi\}$, in the lossless, low-frequency limit the transmitted noise levels reduce to the well-known parametric result

$$\mathbf{S}_{\text{OPO}}^0[\Omega] = \begin{pmatrix} e^{+2r} & 0 \\ 0 & e^{-2r} \end{pmatrix} \quad \text{and} \quad \mathbf{S}_{\text{OPO}}^\pi[\Omega] = \begin{pmatrix} e^{-2r} & 0 \\ 0 & e^{+2r} \end{pmatrix} \quad (\text{I.107})$$

where we can now establish that an amplified field ($\bar{\varphi}_b = 0$) corresponds to a squeezed phase quadrature and an anti-squeezed amplitude quadrature, while a deamplified field ($\bar{\varphi}_b = \pi$) corresponds to a squeezed amplitude quadrature and an anti-squeezed phase quadrature. Later on, we will use this idealized expression to describe how squeezed light interacts with a mechanical resonator whose frequency is much smaller than the OPO bandwidth.

Losses: Squeezing is very sensitive to optical losses, which couple uncorrelated vacuum fluctuations into the squeezed field and degrade the squeezing level. The escape efficiency $\eta_{\text{esc}} = \kappa_2/\kappa$ of the OPO cavity is one such loss mechanism, but there are many others in a real experiment: propagation losses, mode-mismatch, non-unity quantum efficiency of the photodetectors, etc. One can then distinguish between *intracavity* losses, which are accounted for in the escape efficiency, and *extracavity* losses, which we denote by η_{ext} and lump all other loss mechanisms into a single effective loss. The effect of these losses can be modeled as a beam-splitter mixing the squeezed field with vacuum fluctuations, such that the lossy covariance matrix is given by

$$\mathbf{S}_{\text{det}}[\Omega] = (1 - \eta) \mathbf{S}_{\text{OPO}}^{\bar{\varphi}_b}[\Omega] + \eta \mathbf{1} \quad (\text{I.108})$$

This expression is actually true for any Gaussian state suffering from losses.

Frequency dependence: Similarly to what was seen earlier considering general quantum states, squeezing at an arbitrary angle θ can be obtained by rotating the covariance matrix. However, one can now make the squeezing angle frequency dependent above as

$$\mathbf{S}_{\text{OPO}}^\theta[\Omega] = \mathbf{R}(\theta[\Omega]) \mathbf{S}_{\text{OPO}}^0[\Omega] \mathbf{R}^\dagger(\theta[\Omega]). \quad (\text{I.109})$$

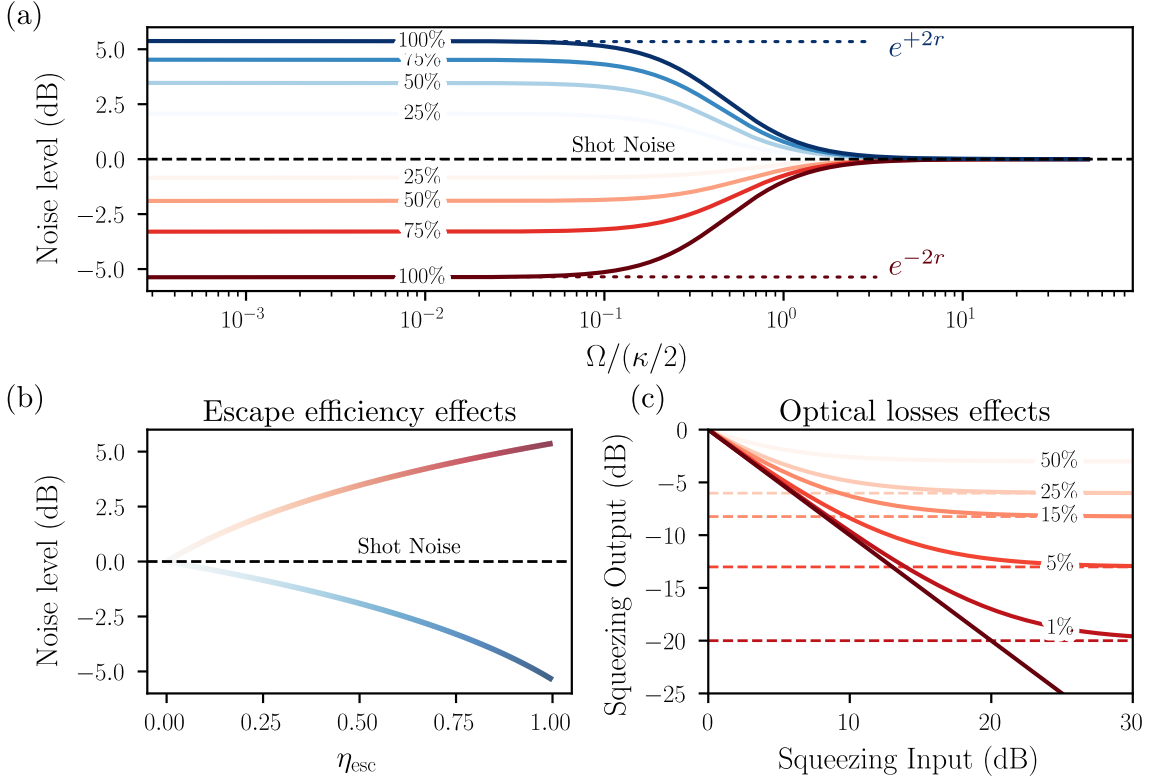


Fig. I.11 Squeezing degradation properties of a non perfect OPO. (a) Squeezing-Antisqueezing levels obtained as a function of frequency (in cavity linewidth unit). The squeezing-antisqueezing levels are maximised at 100% escape efficiency and inside the cavity linewidth (see dark red and dark blue curves). (b) Squeezing-antisqueezing levels as a function of the escape efficiency. (c) Output Squeezing level as a function of the Input Squeezing level (right at the OPO output) considering various optical loss values (extrinsic losses).

where $\theta[]$ The $\mathbf{S}[\Omega]$ can either be the full cavity one, or the idealized one. As already mentionned, the mechanical frequencies of interest will be deep in the OPO bandwidth such that we will use the ideal squeezer expression (I.107) in addition with extrinsic losses (I.108). The explicit of the covariance matrix at a frequency dependent angle is then

$$\mathbf{S}_{\text{OPO}}^\theta[\Omega] = \begin{pmatrix} \cosh 2r + \sinh 2r \cos 2\theta[\Omega] & -\sinh 2r \sin 2\theta[\Omega] \\ -\sinh 2r \sin 2\theta[\Omega] & \cosh 2r - \sinh 2r \cos 2\theta[\Omega] \end{pmatrix} \quad (\text{I.110})$$

I.2.6 Optomechanical Cavities

We now turn to standard optomechanical cavities. As in the simple FP case, we consider a cavity mode, in which we now allow one of the the coupler (traditionnaly the output coupler), to be itself a *mechanical* harmonic oscillator with annihilation operator \hat{c} , effective

mass m , angular frequency Ω_m and damping rate Γ_m . In canonical optomechanical systems the mechanics operators are usually denoted as \hat{b} but in our case it would be redundant with the operators describing the pump field in non linear systems. The position can be expressed in terms of our bosonic operators as $\hat{x} = x_0(\hat{c} + \hat{c}^\dagger)$ with $x_0 = \sqrt{\hbar/(2m\Omega_m)}$ the resonator's zero point fluctuations.

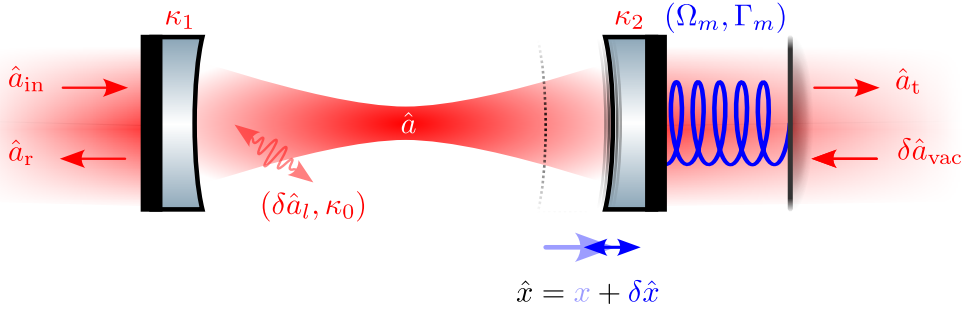


Fig. I.12 *Diagram generic optomechanical system.* \hat{a} 's are the various fields at play, κ 's are the various couplings involved, with $\delta\hat{a}$'s the associated fluctuations. \hat{x} is the quantum position operator of the mechanical resonator which linearly shifts the cavity resonance frequency.

Mechanics & Radiation Pressure Force

The equation of motion of such an oscillator are given by

$$m \ddot{x} = -m \Omega_m^2 \hat{x} - m \Gamma_m \dot{\hat{x}} + \hat{F} \quad (\text{I.111})$$

where \hat{F} is the total force acting on the oscillator. In Fourier space, we recover the standard linear response form

$$\hat{x}[\Omega] = \chi[\Omega] \hat{F}[\Omega] \quad \text{with} \quad \chi[\Omega] = \frac{1}{m(\Omega_m^2 - \Omega^2 - i\Gamma_m \Omega)} \quad (\text{I.112})$$

where $\chi[\Omega]$ is the susceptibility linearly relating the position $\hat{x}[\Omega]$ to the external force $\hat{F}[\Omega]$. This susceptibility can also be written as

$$\chi[\Omega] = |\chi[\Omega]| e^{i\phi_m[\Omega]} \quad (\text{I.113})$$

with

$$\text{with } \phi_m[\Omega] = \arctan \left(\frac{\Gamma_m \Omega}{\Omega_m^2 - \Omega^2} \right) \quad \text{and} \quad |\chi[\Omega]| = \frac{1}{m \sqrt{(\Omega_m^2 - \Omega^2)^2 + (\Gamma_m \Omega)^2}}.$$

Similarly to the simple Fabry-Perot cavity (being a driven damped harmonic oscillator

too), we can define the analog of the Finesse, namely the quality factor, defined as

$$Q = \frac{\Omega_m}{\Gamma_m} \quad (\text{I.114})$$

which is the number of oscillations before the resonator's energy is damped by a factor $1/e$. On resonance, the susceptibility is purely imaginary and reads $\chi[\Omega_m] = -iQ/(m\Omega_m^2)$.

As before, the position is also linearized considering small quantum fluctuations compared to its mean value, such that we write $\hat{x} = x + \delta\hat{x}$. Importantly, the total position fluctuation $\delta\hat{x} = \sum \delta\hat{x}_i$ is the sum of individual fluctuations that can arise from various sources, such as a the zero point fluctuations, thermal fluctuations or radiation pressure induced fluctuations. In the following we will only consider a radiation pressure induced fluctuations $\delta\hat{x}_{\text{RPN}}$, such that $\delta\hat{x} = \delta\hat{x}_{\text{RPN}}$.

Due to the continuous yet discrete photon *hits* at a rate exceeding the resonator frequency, the resonator *feels* an effective force. This radiation pressure force is expressed as

$$\hat{F} = 2\frac{\hbar k_L}{\tau_c} \hat{a}^\dagger \hat{a} = 2\frac{\hbar k_L}{\tau_c} |\bar{\alpha}|^2 + 2\frac{\hbar k_L}{\tau_c} |\bar{\alpha}| \delta\hat{p} + \mathcal{O}(\delta\hat{a}^\dagger \delta\hat{a}) \quad (\text{I.115})$$

where $k_L = 2\pi/\lambda$ is the laser wavevector, and $\tau_c = 2L/c$ is the cavity round-trip time, and we neglect second order terms. This force then features a static component shifting the resonator away from its equilibrium position, that be the x component, as well as a fluctuating component $\delta\hat{F} \propto \delta\hat{p}$ jittering the resonator around its mean displacement, that's $\delta\hat{x}_{\text{RPN}}$. The position mean value and its fluctuations under radiation pressure can therefore be expressed to first order as

$$x = \frac{2\hbar k_L |\bar{\alpha}|^2}{\tau_c} \chi[0], \quad \delta\hat{x}_{\text{RPN}}[\Omega] = \frac{2\hbar k_L |\bar{\alpha}|}{\tau_c} \chi[\Omega] \delta\hat{p}[\Omega]. \quad (\text{I.116})$$

Optomechanical QLE

Considering an optomechanical cavity of length L at rest, such that the mean resonator position is initialy 0, the bare cavity free spectral range is given by $\omega_{\text{FSR}} = \pi c/L$ and the cavity frequency $\omega_c = N\omega_{\text{FSR}}$. Injecting light inside this cavity then shifts the mechanical resonator position as seen above, which in turn changes the cavity length $L \rightarrow L+x$, thus its frequency. Writing the Hamiltonian, we simply Taylor expand to first order in \hat{x} the cavity frequency $\omega_c(\hat{x}) = \omega_c + \hat{x} \partial\omega_c/\partial x$ such that we have:

$$\hat{H} = -\hbar\Delta\hat{a}^\dagger \hat{a} + \hbar G\hat{x} \hat{a}^\dagger \hat{a} + \hbar\Omega_m \hat{c}^\dagger \hat{c} \quad (\text{I.117})$$

where $G = \partial\omega_c/\partial x = -\omega_c/L$. One can also identify a useful identity by considering the radiation pressure force (I.115) and the Hamiltonian above, such that

$$\hat{F}_{\text{rad}} = -\frac{\partial\hat{H}}{\partial\hat{x}} = -\hbar G\hat{a}^\dagger\hat{a} \Rightarrow G = -2\frac{k_L}{\tau_c} \quad (\text{I.118})$$

consistent with our previous expression of G such that we rewrite the position fluctuation as $\delta\hat{x}_{\text{tot}}[\Omega] = -\hbar G|\bar{\alpha}|\chi[\Omega]\delta\hat{p}[\Omega]$. Plugging in the QLE and ignoring vacuum and loss fluctuations for notational simplicity, the field's equation are written as

$$\begin{cases} 0 = -\left(\frac{\kappa}{2} - i\bar{\Delta}\right)\bar{\alpha} + \sqrt{\kappa_1}|\bar{\alpha}_{\text{in}}| \\ \delta\dot{\hat{\mathbf{a}}}(t) = -\begin{pmatrix} \kappa/2 - i\bar{\Delta} & 0 \\ 0 & \kappa/2 + i\bar{\Delta} \end{pmatrix}\delta\hat{\mathbf{a}}(t) + iG\bar{\alpha}\delta\hat{x}\begin{pmatrix} +1 \\ -1 \end{pmatrix} + \sqrt{\kappa_1}\delta\hat{\mathbf{a}}_{\text{in}}(t) + \sqrt{\kappa_2}\delta\hat{\mathbf{a}}_{\text{vac}}(t) \end{cases} \quad (\text{I.119})$$

where we introduced the radiation pressure induced detuning $\bar{\Delta} = \Delta - Gx$ - that is, the mean resonator displacement shifts the cavity frequency, hence the detuning - and where we assume the input field to be real.

This so called *dispersive* coupling, where the cavity frequency $\omega_c(x)$ depends linearly on the resonator's position to firs order, is the hallmark of the optomechanical interaction. In the canonical model, the cavity linewidth κ do not depend on the resonator's position.

Mean field solution & Bistability: Writing the mean intracavity amplitude by keeping the *unperturbed* detuning Δ for clarity and substituting for the static displacement x , we get

$$\bar{\alpha} = \frac{\sqrt{\kappa_1}}{\kappa/2 - i\left(\Delta - \frac{\hbar G^2 |\bar{\alpha}|^2}{m_{\text{eff}}\Omega_m^2}\right)} |\bar{\alpha}_{\text{in}}| \quad (\text{I.120})$$

where the $|\bar{\alpha}|^2$ dependence in disguise in the mean mechanical displacement is the root of the bistable behaviour of optomechanical cavities. We show the induced hysteresis in figure ...

For moderate injected powers, this is the standard intracavity field formula where we simply relabel $\Delta - Gx \rightarrow \Delta$ to lighten the notation. When resonant, the intracavity field does not pick up any phase and is real i.e. $\bar{\alpha} = |\bar{\alpha}| = 2\sqrt{\kappa_1}/\kappa|\bar{\alpha}_{\text{in}}|$.

Optomechanical cavities do display optical ringdowns too, as detailed in the cavity sub-part above, but this is a purely optical phenomenon: the mechanics plays no role in the optical ringdwon (to first order?).

Fluctuations solution: As previously, going to Fourier space now yields

$$\mathbf{M}_{\bar{\Delta}} \delta \hat{\mathbf{a}}[\Omega] = i G \bar{\alpha} \delta \hat{x}[\Omega] \begin{pmatrix} +1 \\ -1 \end{pmatrix} + \sqrt{\kappa_1} \delta \hat{\mathbf{a}}_{\text{in}}[\Omega] + \sqrt{\kappa_2} \delta \hat{\mathbf{a}}_{\text{vac}}[\Omega] \quad (\text{I.121})$$

where we injected the mean field solution (??) in our equations assuming moderate input power to ignore bistable behaviour. We focus on the resonant case to derive our noise spectra, such that $\mathbf{M}_0 = (\kappa/2 - i\Omega)\mathbf{I}$ and the intracavity quadratures are

$$\delta \hat{\mathbf{u}}[\Omega] = \frac{2G|\bar{\alpha}|}{\kappa/2 - i\Omega} \delta \hat{x}[\Omega] \begin{pmatrix} 0 \\ 1 \end{pmatrix} + \frac{\sqrt{\kappa_1}}{\kappa/2 - i\Omega} \delta \hat{\mathbf{u}}_{\text{in}}[\Omega] + \frac{\sqrt{\kappa_2}}{\kappa/2 - i\Omega} \delta \hat{\mathbf{u}}_{\text{vac}}[\Omega] \quad (\text{I.122})$$

Writing explicitly our amplitude-phase quadratures then gives

$$\begin{aligned} \delta \hat{p}[\Omega] &= \frac{\sqrt{\kappa_1}}{\kappa/2 - i\Omega} \delta \hat{p}_{\text{in}}[\Omega] + \frac{\sqrt{\kappa_2}}{\kappa/2 - i\Omega} \delta \hat{p}_{\text{vac}}[\Omega] \\ \delta \hat{q}[\Omega] &= \frac{2G|\bar{\alpha}|}{\kappa/2 - i\Omega} \delta \hat{x}[\Omega] + \frac{\sqrt{\kappa_1}}{\kappa/2 - i\Omega} \delta \hat{q}_{\text{in}}[\Omega] + \frac{\sqrt{\kappa_2}}{\kappa/2 - i\Omega} \delta \hat{q}_{\text{vac}}[\Omega] \end{aligned} \quad (\text{I.123})$$

This expression highlights the fact that only the phase is affected by the resonator position fluctuations. Physically, this can be understood by considering first that a fluctuating field amplitude leads to a fluctuating radiation pressure force, which in turn *shakes* the mechanical resonator, which changes the phase of the field reflected. The reciprocal process does not happen: a fluctuating phase does not lead to a fluctuating radiation pressure force, hence the output amplitude fluctuations are unaffected by the mechanics.

Importantly, considering the field reflected off the cavity, we define the displacement to phase fluctuation transduction $\mathcal{C}[\Omega]$ such that

$$\delta \hat{q}_{\text{ref}}[\Omega] = \mathcal{C}[\Omega] \delta \hat{x}[\Omega] \quad \text{with} \quad \mathcal{C}[\Omega] = \frac{2\sqrt{\kappa_1}G|\bar{\alpha}|}{\kappa/2 - i\Omega} = \frac{\kappa_1}{\kappa} \frac{16\mathcal{F}\sqrt{\bar{I}_{\text{in}}}}{\lambda(1 - i2\Omega/\kappa)} \quad (\text{I.124})$$

where we plugged in useful experimental parameters \mathcal{F} , λ and \bar{I}_{in} . The prefactor κ_1/κ is the analog of the escape efficiency for optomechanical cavities, and is unity for single port cavities. We stress that the total phase fluctuations are the sum of various contributions, including the input phase fluctuations, the vacuum fluctuations entering from the loss port, and the position induced phase fluctuations, whether they arise from radiation pressure or other sources. This transduction factor will be used later to express the displacement sensitivity/spectra in terms of experimental parameters.

Plugging in the position fluctuations derived earlier ((I.116) and (I.115)) in the intracavity

phase fluctuations we get

$$\begin{aligned}\delta\hat{q}[\Omega] = & \frac{\mathcal{C}^2[\Omega]}{2\kappa_1} \hbar\chi[\Omega] \left(\sqrt{\kappa_1} \delta\hat{p}_{\text{in}}[\Omega] + \sqrt{\kappa_2} \delta\hat{p}_{\text{vac}}[\Omega] \right) \\ & + \frac{1}{\kappa/2 - i\Omega} \left(\sqrt{\kappa_1} \delta\hat{q}_{\text{in}}[\Omega] + \sqrt{\kappa_2} \delta\hat{q}_{\text{vac}}[\Omega] \right)\end{aligned}\quad (\text{I.125})$$

such that we can readily express the intracavity quadratures in matrix form as

$$\delta\hat{\mathbf{u}}[\Omega] = \begin{pmatrix} \frac{1}{\kappa/2 - i\Omega} & 0 \\ \frac{\mathcal{K}[\Omega]}{\kappa_1} & \frac{1}{\kappa/2 - i\Omega} \end{pmatrix} \left(\sqrt{\kappa_1} \delta\hat{\mathbf{u}}_{\text{in}}[\Omega] + \sqrt{\kappa_2} \delta\hat{\mathbf{u}}_{\text{vac}}[\Omega] \right). \quad (\text{I.126})$$

with

$$\mathcal{K}[\Omega] = \frac{\mathcal{C}^2[\Omega]}{2} \hbar\chi[\Omega] = \left(\frac{\kappa_1}{\kappa}\right)^2 \frac{128\hbar\mathcal{F}^2\bar{I}_{\text{in}}}{\lambda^2(1-i2\Omega/\kappa)^2} \chi[\Omega]$$

We then obtain the reflected and transmitted quadrature fluctuations

$$\begin{aligned}\delta\hat{\mathbf{u}}_{\text{ref}} &= \mathbf{T}_{\text{ref}}\delta\hat{\mathbf{u}}_{\text{in}} + \mathbf{L}_{\text{ref}}\delta\hat{\mathbf{u}}_{\text{vac}} \\ \delta\hat{\mathbf{u}}_{\text{trans}} &= \mathbf{T}_{\text{trans}}\delta\hat{\mathbf{u}}_{\text{in}} + \mathbf{L}_{\text{trans}}\delta\hat{\mathbf{u}}_{\text{vac}}.\end{aligned}\quad (\text{I.127})$$

where we defined the transfer matrices

$$\begin{aligned}\mathbf{T}_{\text{ref}} &= \begin{pmatrix} \frac{\kappa_1}{\kappa/2 - i\Omega} - 1 & 0 \\ \frac{\mathcal{K}[\Omega]}{\kappa_1} & \frac{\kappa_1}{\kappa/2 - i\Omega} - 1 \end{pmatrix} & \mathbf{L}_{\text{ref}} &= \begin{pmatrix} \frac{\sqrt{\kappa_1\kappa_2}}{\kappa/2 - i\Omega} & 0 \\ \sqrt{\frac{\kappa_2}{\kappa_1}} \mathcal{K}[\Omega] & \frac{\sqrt{\kappa_1\kappa_2}}{\kappa/2 - i\Omega} \end{pmatrix} \\ \mathbf{T}_{\text{trans}} &= \begin{pmatrix} \frac{\sqrt{\kappa_1\kappa_2}}{\kappa/2 - i\Omega} & 0 \\ \sqrt{\frac{\kappa_2}{\kappa_1}} \mathcal{K}[\Omega] & \frac{\sqrt{\kappa_1\kappa_2}}{\kappa/2 - i\Omega} \end{pmatrix} & \mathbf{L}_{\text{trans}} &= \begin{pmatrix} \frac{\kappa_2}{\kappa/2 - i\Omega} - 1 & 0 \\ \frac{\kappa_2}{\kappa_1} \mathcal{K}[\Omega] & \frac{\kappa_2}{\kappa/2 - i\Omega} - 1 \end{pmatrix}\end{aligned}$$

Convergence to VIRGO/LIGO notation: To sanity check this expression, we need to make sure we recover the standard expressions used in the LIGO/VIRGO community. This is we will assume the mechanical resonator is free, that is $\Omega_m \rightarrow 0$ and $\Gamma_m \rightarrow 0$. The susceptibility then reduces to $\chi[\Omega] = 1/M\Omega^2$, and we will consider sideband frequencies $\Omega \ll \kappa/2$ such that all terms in $\Omega/(\kappa/2)$ can be neglected. We also consider a single port cavity such that $\kappa_1 = \kappa$ and $\kappa_2 = 0$. The reflected quadrature fluctuations then read

$$\delta\hat{\mathbf{u}}_{\text{ref}} = \begin{pmatrix} 1 & 0 \\ \frac{32\omega_0 P_{\text{in}}}{ML^2\kappa^2\Omega^2} & 1 \end{pmatrix} \delta\hat{\mathbf{u}}_{\text{in}}. \quad (\text{I.128})$$

In GW papers, the pre factor will often be 8 (and not 32) as they use the cavity half width at half maximum rather than κ . We indeed recover the standard expression used in the GW community, which is a good sanity check of our derivation. We do stress however that this expression is only valid for a free mass, and that the full expression including the mechanical resonance is required to describe optomechanical cavities in general.

Reflected spectra: We can now compute the covariance matrix of the reflected quadratures, assuming vacuum fluctuations both at the input and at the loss port. We additionally consider a quasi single port cavity for simplicity $\kappa_1 \gg \kappa_2$, such that $\kappa_1 \sim \kappa$, as well as the bad cavity limit $\Omega \ll \kappa/2$. The reflected covariance matrix is then given by

$$\mathbf{S}_{\text{ref}} = \mathbf{T}_{\text{ref}} \mathbf{S}_{\text{in}} \mathbf{T}_{\text{ref}}^\dagger = \begin{pmatrix} 1 & \mathcal{K}[\Omega] \\ \mathcal{K}^*[\Omega] & 1 + |\mathcal{K}[\Omega]|^2 \end{pmatrix} \quad (\text{I.129})$$

where the off-diagonal entries are complex conjugates of each other, ensuring the covariance matrix is Hermitian as required. The diagonal terms are the amplitude and phase noise spectra respectively, while the off-diagonal terms quantify correlations between amplitude and phase. The presence of these correlations is the hallmark of optomechanical/ponderomotive squeezing i.e. using the non linear response of the resonator to squeeze light. This effect is not seen nor sought in our experiment, but is a very active field of research in the optomechanics community.

One now sees two essential components in the reflected phase spectrum. The first is the direct phase fluctuations, which is simply shot noise seen as 1. The second is the back-action term $\propto |\mathcal{K}[\Omega]|^2$, which is the phase fluctuations induced by the resonator motion driven by radiation pressure fluctuations.

I.3 Detection

Having layed out the theoretical framework to describe the optical fields interacting with our various cavities, we now turn to the detection schemes used to probe these fields. To detect the optical field reflected or transmitted from these optical systems, we will use two main techniques: direct detection and balanced homodyne detection.

I.3.1 Direct detection

Direct detection consists in measuring the intensity of the optical field impinging on a photodiode. We will detail three cases: the single field case, where only the signal field is incident on the photodiode, the case where a local oscillator (LO) field is added to the signal field,

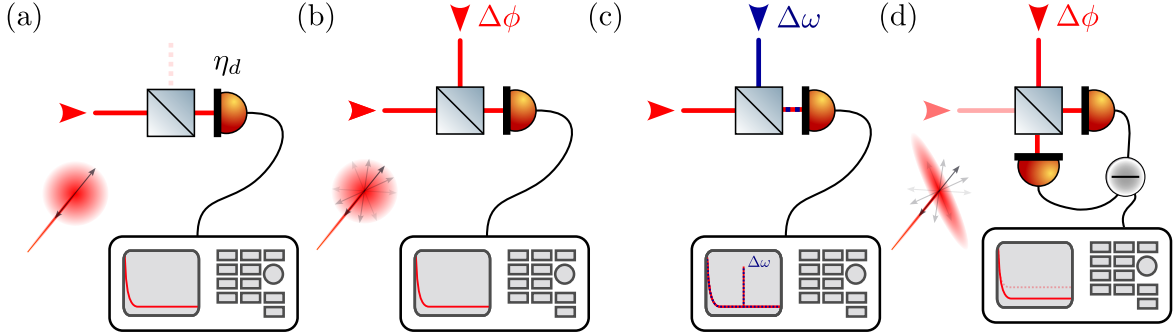


Fig. I.13 coucou

and finally the case where two beams at different slightly different wavelengths are incident on the photodiode.

Single field: The photocurrent operator, originating from the photoelectric effect is given by

$$\hat{I} = e \hat{a}^\dagger \hat{a} \quad (\text{I.130})$$

with e the electron charge. We introduce the quantum efficiency of the photodiode η_d to account for non unity detection efficiency, such that the detected field operator is written as

$$\hat{a} \rightarrow \sqrt{\eta_d} \hat{a} + \sqrt{1 - \eta_d} \hat{a}_{\text{vac}}$$

where \hat{a}_{vac} are vacuum fluctuations entering due to non unity detection efficiency. Assuming a real mean field $\bar{\alpha}$, photocurrent operator then reads

$$\hat{I} = \eta_d e \left(|\bar{\alpha}|^2 + \bar{\alpha} \delta p + \sqrt{\eta_d(1 - \eta_d)} \bar{\alpha} \delta p_{\text{vac}} \right) \quad (\text{I.131})$$

where we neglected second order terms. The photocurrent fluctuations in Fourier space are then given by

$$\delta \hat{I}[\Omega] = \eta_d e \bar{\alpha} \left(\delta p[\Omega] + \sqrt{\frac{1 - \eta_d}{\eta_d}} \delta p_{\text{vac}}[\Omega] \right) \quad (\text{I.132})$$

such that the photocurrent noise spectrum is

$$S_{II}[\Omega] = \eta_d^2 e^2 |\bar{\alpha}|^2 \left(S_{pp}[\Omega] + \frac{1 - \eta_d}{\eta_d} \right) \quad (\text{I.133})$$

where $S_{pp}[\Omega]$ is the amplitude quadrature noise spectrum of the incident field. This expression highlights that direct detection is only sensitive to amplitude quadrature fluctuations.

Two fields: Let's now consider an auxiliary field at the same frequency \hat{a}_{LO} , called the local oscillator (LO), which is a coherent field dephased from our real signal field \hat{a} by a phase ϕ_{LO} such that the total field impinging on the photodiode is $\hat{a}_{\text{tot}} = \hat{a} + \hat{a}_{\text{LO}}$. So far, we do not consider the LO to be consequently stronger than the signal field, as we will do in the homodyne detection. This coherent addition can be performed using a beam-splitter or a polarizing beam-splitter, depending on the experimental implementation. The mean field of the total field is then given by $\bar{\alpha}_{\text{tot}} = \bar{\alpha} + |\bar{\alpha}_{\text{LO}}|e^{i\phi_{\text{LO}}}$, and its fluctuations are $\delta\hat{a}_{\text{tot}} = \delta\hat{a} + \delta\hat{a}_{\text{LO}}$. For simplicity we will assume a quantum efficiency of 1 in the following. The photocurrent operator mean values is then given by

$$\bar{I} = e \left(|\bar{\alpha}|^2 + |\bar{\alpha}_{\text{LO}}|^2 + 2|\bar{\alpha}||\bar{\alpha}_{\text{LO}}| \cos \phi_{\text{LO}} \right) \quad (\text{I.134})$$

where we see the interference term between the signal and the LO: scanning the LO phase ϕ_{LO} (with a piezoelectric actuator) will lead to interference fringes on the mean photocurrent, which can be used to lock the LO phase. We won't developp the full expression of the photocurrent fluctuation spectrum here (see Annexe B), as they feature a cumbersome linear combination of the amplitude and phase quadrature noise spectra of both the signal and the LO fields, as well as cross correlation terms between the two fields (if any), which is not very interesting experimentally. However, we can already sense that adding a LO field allows to access phase quadrature fluctuations of the signal field, which was not possible with direct detection alone.

Let's consider 'slow' (hence low frequency) classical fluctuations of the LO phase $\delta\phi_{\text{LO}}(t)$ around a mean value $\bar{\phi}_{\text{LO}}$, such that $\phi_{\text{LO}}(t) = \bar{\phi}_{\text{LO}} + \delta\phi_{\text{LO}}(t)$ with $\delta\phi_{\text{LO}}(t) \ll 1$. Developing the photocurrent to first order in these classical fluctuations, the mean photocurrent fluctuations then reads

$$\delta\bar{I}(t) \propto \delta\phi_{\text{LO}}(t) \quad (\text{I.135})$$

such that slow phase fluctuations of the LO are directly transduced into photocurrent fluctuations. The classical phase noise of the LO can therefore pollute the photocurrent noise spectrum at low frequency, as well as limit the lock stability of the LO phase. Let's now consider the case where the LO is phase modulated at a frequency Ω_{mod} as seen previously

$$\alpha_{\text{LO}}(t) \approx \bar{\alpha}_{\text{LO}} \left(1 + i\epsilon_\phi \cos(\Omega_{\text{mod}} t) \right)$$

such that the mean photocurrent fluctuations are now given by

$$\delta\bar{I}(t) \propto \cos(\Omega_{\text{mod}} t) \delta\phi_{\text{LO}}(t) \quad (\text{I.136})$$

so that the LO phase noise is spectrally only transduced around the modulation frequency Ω_{mod} . Demodulating the photocurrent at Ω_{mod} then yields an error signal proportional to the LO phase fluctuations, which can be used to lock the LO phase to a desired value $\bar{\phi}_{\text{LO}}$, while rejecting low frequency phase noise of the LO.

Two fields at different frequencies: Finally, let's consider the case where the signal and LO fields are at slightly different wavelengths/frequencies, such that \hat{a} is at frequency ω_0 and \hat{a}_{LO} at frequency $\omega_0 + \omega_{\text{beat}}$. The total field impinging on the photodiode is then written as $\hat{a}_{\text{tot}} = \hat{a} + \hat{a}_{\text{LO}}e^{-i\omega_{\text{beat}}t}$ since our operators are defined in a frame rotating at ω_0 . The mean photocurrent is then given by

$$\bar{I} = e \left(|\bar{\alpha}|^2 + |\bar{\alpha}_{\text{LO}}|^2 + 2|\bar{\alpha}||\bar{\alpha}_{\text{LO}}| \cos(\omega_{\text{beat}}t + \phi_{\text{LO}}) \right) \quad (\text{I.137})$$

where we see that the interference term now oscillates at the beat frequency ω_{beat} . Demodulating the photocurrent at a frequency $\omega_{\text{ref}} \sim \omega_{\text{beat}}$, phase $\tilde{\phi}$, and low pass filtering the photocurrent then gives

$$\bar{I}_{\text{demod}} \propto \cos((\omega_{\text{beat}} - \omega_{\text{ref}})t + \phi - \tilde{\phi}). \quad (\text{I.138})$$

This very signal can then be used to lock the frequency of an auxiliary laser to the desired frequency offset ω_{ref} from the main laser. However, this signal featuring many zero crossings, one needs to tune the auxiliary laser frequency close enough to the desired offset so that it ensures the feedback loop locks to the correct zero crossing. This is generally done manually by scanning the auxiliary laser frequency until the right zero crossing is found, confirmed by monitoring the beatnote on a spectrum analyzer.

I.3.2 Balanced Homodyne Detection

Balanced homodyne detection (HD) is a common technique to measure arbitrary quadratures of an optical field with high sensitivity. It consists in mixing the signal field \hat{a} with a strong local oscillator (LO) field \hat{a}_{LO} on a 50:50 beam-splitter, and detecting the two output ports with identical photodiodes. The beamsplitter operation reads

$$\begin{cases} \hat{a}_{\text{out},1} = \frac{1}{\sqrt{2}}(\hat{a} + \hat{a}_{\text{LO}}) \\ \hat{a}_{\text{out},2} = \frac{1}{\sqrt{2}}(\hat{a} - \hat{a}_{\text{LO}}) \end{cases} \quad (\text{I.139})$$

The two photodiodes then measure the photocurrents $\hat{I}_1 = e \hat{a}_{\text{out},1}^\dagger \hat{a}_{\text{out},1}$ and $\hat{I}_2 = e \hat{a}_{\text{out},2}^\dagger \hat{a}_{\text{out},2}$. The BHD photocurrent is then defined as the difference between the two photocurrents

$\hat{I}_{\text{BHD}} = \hat{I}_1 - \hat{I}_2$, which reads

$$\hat{I}_{\text{HD}} = e (\hat{a}_{\text{LO}}^\dagger \hat{a} + \hat{a}^\dagger \hat{a}_{\text{LO}}) \quad (\text{I.140})$$

Assuming a real mean field for the signal $\bar{\alpha}$ and a phase shifted LO mean field $\bar{\alpha}_{\text{LO}} = |\bar{\alpha}_{\text{LO}}| e^{i\phi_{\text{LO}}}$, we can linearize the HD photocurrent to first order in the fluctuations as

$$\hat{I}_{\text{HD}} = 2e |\bar{\alpha}_{\text{LO}}| |\bar{\alpha}| \cos \phi_{\text{LO}} + e |\bar{\alpha}_{\text{LO}}| (\cos \phi_{\text{LO}} \delta \hat{p} + \sin \phi_{\text{LO}} \delta \hat{q}) \quad (\text{I.141})$$

where we recognise the mean photocurrent term in $2e |\bar{\alpha}_{\text{LO}}| |\bar{\alpha}| \cos \phi_{\text{LO}}$ as in the two fields direct detection case. This slowly varying mean photocurrent can be used to lock the LO phase ϕ_{LO} to a desired value, as previously described, with a piezoelectric actuator and phase modulation/demodulation scheme if needed. The HD photocurrent fluctuations in Fourier space are then given by

$$\delta \hat{I}_{\text{HD}}[\Omega] = e |\bar{\alpha}_{\text{LO}}| (\cos \phi_{\text{LO}} \delta \hat{p}[\Omega] + \sin \phi_{\text{LO}} \delta \hat{q}[\Omega]) \quad (\text{I.142})$$

such that the HD photocurrent noise spectrum reads

$$S_{II}^{\text{HD}}[\Omega] = e^2 |\bar{\alpha}_{\text{LO}}|^2 (\cos^2 \phi_{\text{LO}} S_{pp}[\Omega] + \sin^2 \phi_{\text{LO}} S_{qq}[\Omega] + 2 \sin \phi_{\text{LO}} \cos \phi_{\text{LO}} S_{pq}[\Omega]) \quad (\text{I.143})$$

where $S_{pp}[\Omega]$, $S_{qq}[\Omega]$ and $S_{pq}[\Omega]$ are respectively the amplitude, phase and cross correlation noise spectra of the signal field. By tuning the LO phase ϕ_{LO} , one can therefore measure arbitrary quadratures of the signal field with high sensitivity thanks to the strong LO field amplifying the signal fluctuations. This is the main advantage of HD over direct detection, where only amplitude quadrature fluctuations can be measured. To calibrate the HD detection efficiency, one can block the signal field, such that the LO now probes vacuum fluctuations only. This reference is then used to evaluate the squeezing level of the signal field when unblocked.

The practical implementation of these detection schemes and the associated locks are detailed in chapter 3.

Chapter II

Theory: Squeezed Light & Optomechanics

This chapter will cover the elementary concepts required to describe an membrane based optomechanical system in a quantum regime. We will first recall basics on optical field quantization as well describing coherent and squeezed light field, to then turn to the more specific frequency dependent squeezed light field. Secondly, we will cover the mathematical description of a mechanical resonator interacting with a generic coherent optical field, highlighting the differences with the seminal optomechanical system of a mirror on a spring. Finally, we will derive the equations of motions of a membrane based optomechanical system with frequency dependent squeezed optical fields.

Contents

II.1 Squeezed Light and Optomechanics	55
II.1.1 Standard Quantum Limit	55
II.1.2 Frequency Independent Squeezing in Optomechanical Cavities	58
II.1.3 Frequency Dependent Squeezing in Optomechanical Cavities	61
II.1.4 Filter Cavities for Frequency Dependent Squeezing	62
II.2 Cavity Optomechanics with Membrane based systems	63
II.2.1 Classical Description	63
II.2.2 Quantum Description	67

II.1 Squeezed Light and Optomechanics

We will now introduce the concept of Standard Quantum Limit (SQL) in the context of optomechanical measurements, and show how frequency dependent squeezed light can be used to surpass this limit.

For the rest of this section we will assume the following

- A cavity on resonance: $\Delta = 0$.
- A single port optomechanical cavity: $\kappa_1 \sim \kappa$.
- The unresolved sideband regime: $(\Omega, \Omega_m) \ll \kappa/2$.

II.1.1 Standard Quantum Limit

The question of interest is now:

what is the best displacement sensitivity one can achieve?

We start by recalling the reflected phase fluctuation of an optomechanical cavity from section I.2.5 under the aforementioned assumptions:

$$\delta\hat{q}_{\text{ref}}[\Omega] = \delta\hat{q}_{\text{in}}[\Omega] + \mathcal{K}[\Omega] \delta\hat{p}_{\text{in}}[\Omega] \quad \text{with} \quad \mathcal{K}[\Omega] = \frac{\mathcal{C}^2}{2} \hbar\chi[\Omega] = \frac{128\mathcal{F}^2\bar{I}_{\text{in}}}{\lambda^2} \hbar\chi[\Omega]$$

where \mathcal{C} is now positive and frequency independent. The resulting reflected phase spectrum reads

$$S_{qq}^{\text{ref}}[\Omega] = S_{qq}^{\text{in}}[\Omega] + |\mathcal{K}[\Omega]|^2 S_{pp}^{\text{in}}[\Omega] + 2 \operatorname{Re} [\mathcal{K}[\Omega] S_{pq}^{\text{in}}[\Omega]]$$

The phase to displacement transduction relation with an optomechanical escape efficiency of 1:

$$\delta\hat{q}_x = \mathcal{C}\delta\hat{x}[\Omega] = \frac{16\mathcal{F}\sqrt{\bar{I}_{\text{in}}}}{\lambda} \delta\hat{x}[\Omega]$$

Using these two relations, we can then express displacement fluctuations in terms of input amplitude and phase fluctuations, assuming the reflected field is a perfect probe of the mechanical resonator position fluctuations i.e. $\delta\hat{q}_{\text{ref}}[\Omega] = \delta\hat{q}_x[\Omega]$. This treatment is formally equivalent to considering the output phase as a statistical estimator of the position fluctuations being a stationary random process as done in quantum measurement theory [4]. We then write

$$\delta\hat{x}[\Omega] = \mathcal{C}^{-1} \delta\hat{q}_{\text{in}}[\Omega] + \frac{\mathcal{C}}{2} \hbar\chi[\Omega] \delta\hat{p}_{\text{in}}[\Omega] \tag{II.1}$$

such that the associated displacement spectrum reads

$$S_{xx}[\Omega] = \mathcal{C}^{-2} S_{qq}^{\text{in}}[\Omega] + \left(\frac{\mathcal{C}}{2} \hbar |\chi[\Omega]| \right)^2 S_{pp}^{\text{in}}[\Omega] + \hbar |\chi[\Omega]| \operatorname{Re} \left[e^{i\phi_m[\Omega]} S_{pq}^{\text{in}}[\Omega] \right] \quad (\text{II.2})$$

We then identify three contributions to the displacement spectrum:

- The first term is the laser shot noise (or imprecision noise) scaling inversely with the input power \bar{I}_{in} , arising from the input phase fluctuations $S_{qq}^{\text{in}}[\Omega]$ and given by

$$S_{xx}^{\text{SN}}[\Omega] = \frac{\lambda^2}{256\mathcal{F}^2 \bar{I}_{\text{in}}} S_{qq}^{\text{in}}[\Omega] \quad (\text{II.3})$$

- The second term is the radiation pressure noise (or backaction noise) scaling linearly with the input power \bar{I}_{in} , arising from the input amplitude fluctuations $S_{pp}^{\text{in}}[\Omega]$ driving the mechanical resonator via radiation pressure given by

$$S_{xx}^{\text{RPN}}[\Omega] = \frac{64\mathcal{F}^2 \bar{I}_{\text{in}}}{\lambda^2} \hbar^2 |\chi[\Omega]|^2 S_{pp}^{\text{in}}[\Omega] \quad (\text{II.4})$$

- The third term is a correlation term between amplitude and phase fluctuations $S_{pq}^{\text{in}}[\Omega]$, which can be non-zero for arbitrary squeezed states as seen in the previous section and given by

$$S_{xx}^{\text{cor}}[\Omega] = \hbar |\chi[\Omega]| \operatorname{Re} \left[e^{i\phi_m[\Omega]} S_{pq}^{\text{in}}[\Omega] \right] \quad (\text{II.5})$$

And we write the total displacement spectrum as the sum of these three contributions

$$S_{xx}[\Omega] = S_{xx}^{\text{SN}}[\Omega] + S_{xx}^{\text{RPN}}[\Omega] + S_{xx}^{\text{cor}}[\Omega] \quad (\text{II.6})$$

We now consider vacuum/coherent fluctuations such that $S_{qq}^{\text{in}}[\Omega] = S_{pp}^{\text{in}}[\Omega] = 1$ and $S_{pq}^{\text{in}}[\Omega] = 0$, so that the displacement spectrum simplifies to

$$S_{xx}[\Omega] = \mathcal{C}^{-2} + \left(\frac{\mathcal{C}}{2} \hbar |\chi[\Omega]| \right)^2 \quad (\text{II.7})$$

and we look at what noise dominates the displacement spectrum around the mechanical resonance $\Omega \sim \Omega_m$. In this frequency range, there are two frequencies at which the displacement noise contributions are equal, given by the condition $S_{xx}^{\text{SN}}[\Omega] = S_{xx}^{\text{RPN}}[\Omega]$, leading to the frequency Ω_{SQL} defined as

$$\Omega_{\text{SQL}}^{\pm} = \sqrt{\Omega_m^2 - \frac{\Gamma_m^2}{2}} \pm \frac{1}{2} \sqrt{\Gamma_m^4 - 4\Gamma_m^2 \Omega_m^2 + \left(\frac{\hbar \mathcal{C}^2}{m} \right)^2} \quad (\text{II.8})$$

and consistent with the LIGO/Virgo notation [[harry_advanced_2010](#), [aasi_enhanced_2013](#)]. Over the frequency range of interest $\Omega \in [\Omega_m - \Omega_{SQL}, \Omega_m + \Omega_{SQL}]$, the displacement noise is dominated by the radiation pressure noise, while outside this range, the noise is dominated by the shot noise. However, for every sideband frequency, there exists an optimal input power $\bar{I}_{in}^{SQL}[\Omega]$ at which both contributions are equal, minimizing the total displacement noise. This limit is called the Standard Quantum Limit (SQL) and is a direct consequence of Heisenberg's uncertainty principle applied to continuous position measurements [[braginsky_quantum_1992](#), 4]. This SQL intensity is given by

$$S_{xx}^{SN}[\Omega] = S_{xx}^{RPN}[\Omega] \implies \bar{I}_{in}^{SQL}[\Omega] = \frac{\lambda^2}{128\mathcal{F}^2\hbar|\chi[\Omega]|} \quad (\text{II.9})$$

such that plugging back in this SQL intensity in (II.7) gives the SQL displacement spectrum as

$$S_{xx}^{SQL}[\Omega] = \hbar|\chi[\Omega]| \implies S_{xx}^{SN}[\Omega] + S_{xx}^{RPN}[\Omega] \geq \hbar|\chi[\Omega]| \quad (\text{II.10})$$

which is the fundamental limit to continuous position measurements with coherent light. We also note that for high Q resonators, $\Omega_{SQL} \gg \Gamma_m$, so approximating the susceptibility by its real part holds over a relatively large frequency range but fails at resonance where the susceptibility is purely imaginary.

Thermal Noise

Thermal noise is a major limitation in optomechanical experiments, as it can mask the quantum effects one aims to observe. The mechanical resonator is indeed coupled to a thermal bath at temperature T , which drives the resonator into a thermal state with mean phonon occupation number $\bar{n}_{th} = k_B T / (\hbar\Omega_m)$ in the high temperature limit $k_B T \gg \hbar\Omega_m$. The position fluctuations induced by this thermal force is given by

$$S_{xx}^{th}[\Omega] = \frac{2\hbar}{1 - e^{-\hbar\Omega/k_B T}} \text{Im } \chi[\Omega] \simeq 2m\Gamma_m k_B T |\chi[\Omega]|^2 \quad \text{if } k_B T \gg \hbar\Omega \quad (\text{II.11})$$

where we used the identity $\text{Im } \chi[\Omega] = m\Gamma_m \Omega |\chi[\Omega]|^2$. At $T = 0K$, this reduces to the zero point fluctuations spectrum $S_{xx}^{ZPF}[\Omega] = m\Gamma_m \hbar\Omega_m |\chi[\Omega]|^2 < S_{xx}^{SQL}[\Omega]$, such that is often neglected in the total displacement spectrum. However, at finite temperature, the thermal noise can be much larger than the SQL. Therefore, the total displacement spectrum now reads

$$S_{xx}[\Omega] = S_{xx}^{SN}[\Omega] + S_{xx}^{RPN}[\Omega] + S_{xx}^{cor}[\Omega] + S_{xx}^{th}[\Omega] \quad (\text{II.12})$$

In order to experimentally probe these quantum limits without being limited by various technical noises, one would then need:

- A high finesse cavity, such that the shot noise $S_{xx}^{\text{SN}} \propto \mathcal{F}^{-2}$ level is low, and the radiation pressure noise $S_{xx}^{\text{RPN}} \propto \mathcal{F}^2$ is high. One should however ensure the cavity bandwidth κ is still much larger than the mechanical frequency Ω_m . This can be ensured by tuning the cavity length L and mirror transmissions.
- A low mass, low frequency, high quality factor mechanical resonator, such that the susceptibility modulus at resonance $|\chi[\Omega_m]| = Q/m\Omega_m^2$ is high, and it comes out of the shot noise level significantly.
- A low temperature environment, such that the thermal noise $S_{xx}^{\text{th}} \propto T$ is low and does not mask the quantum effects. This can be ensured by cryogenic cooling of the mechanical resonator, as well as using high quality factor resonators to reduce the mechanical linewidth Γ_m .

We now want to derive the displacement spectrum of an optomechanical system driven by a squeezed light field, whether frequency independent or dependent.

II.1.2 Frequency Independent Squeezing in Optomechanical Cavities

We first recall the (idealized) covariance matrices for both a phase squeezed field and an amplitude squeezed field

$$\mathbf{S}_{\text{OPO}}^0[\Omega] = \begin{pmatrix} e^{+2r} & 0 \\ 0 & e^{-2r} \end{pmatrix}, \quad \mathbf{S}_{\text{OPO}}^\pi[\Omega] = \begin{pmatrix} e^{-2r} & 0 \\ 0 & e^{+2r} \end{pmatrix}$$

For a phase squeezed field, the displacement spectrum reads

$$S_{xx}^0[\Omega] = \mathcal{C}^{-2}e^{-2r} + \left(\frac{\mathcal{C}}{2}\hbar|\chi[\Omega]|\right)^2 e^{+2r} \quad (\text{II.13})$$

while for an amplitude squeezed field, the displacement spectrum reads

$$S_{xx}^\pi[\Omega] = \mathcal{C}^{-2}e^{+2r} + \left(\frac{\mathcal{C}}{2}\hbar|\chi[\Omega]|\right)^2 e^{-2r} \quad (\text{II.14})$$

We then see that phase squeezing reduces the shot noise contribution but increases the radiation pressure noise contribution, while amplitude squeezing reduces the radiation pressure noise contribution but increases the shot noise contribution. The input cross correlations being zero, this is completely equivalent to the coherent state with a rescaled input intensity $e^{\pm 2r}\bar{I}_{\text{in}}$ (hidden in \mathcal{C}) for phase/amplitude squeezing respectively. However, neither of these two configurations can reduce both contributions simultaneously, and therefore cannot improve the SQL limit. This is illustrated in figure II.2.

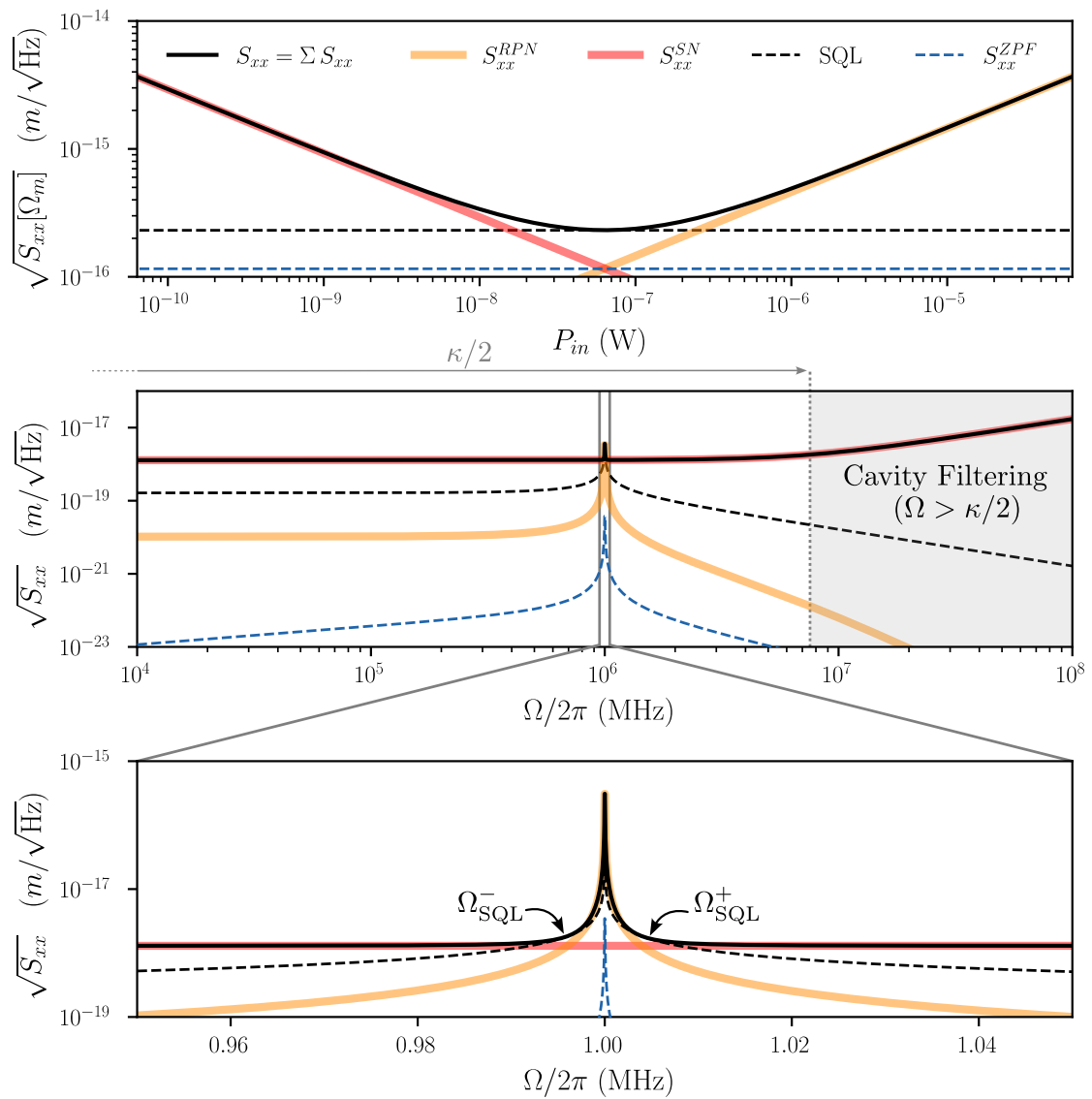


Fig. II.1 DYes

Now consider an input squeezed state with a frequency independent squeezing angle $\theta = \pi/4$ with covariance matrix

$$\mathbf{S}_{\text{OPO}}^{\pi/4}[\Omega] = \begin{pmatrix} \cosh 2r & -\sinh 2r \\ -\sinh 2r & \cosh 2r \end{pmatrix}.$$

The resulting displacement spectrum then reads

$$S_{xx}^{\pi/4}[\Omega] = \left(C^{-2} + \left(\frac{C}{2} \hbar |\chi[\Omega]| \right)^2 \right) \cosh 2r - \hbar |\chi[\Omega]| \sinh 2r \cos \phi_m[\Omega] \quad (\text{II.15})$$

and we seek the frequency range where the displacement spectrum is below the SQL, i.e. $S_{xx}^{\pi/4}[\Omega] < S_{xx}^{\text{SQL}}[\Omega]$. This condition is satisfied when

$$\tanh r < \cos \phi_m[\Omega] < 1 \quad (\text{II.16})$$

Because $\tanh r$ tends to 1 as r increases, the frequency range where the displacement spectrum is below the SQL decreases with increasing squeezing factor r . Furthermore, due to the interplay between quadrature correlations and the projection of the $\pi/4$ ellipse onto the output quadrature axis, acting as an effective increase of the shot noise floor with effective intensity $\bar{I}_{\text{in}} \cosh^{-1} r$, there is an effective range of r above which the displacement spectrum is always above the SQL (for a fixed input intensity). This is illustrated in figure II.2.

Additionally, and as seen in Fig ..., the optimal angle to maximally reduce the displacement spectrum varies with frequency, being 0 at frequencies outside the resonator's bandwidth, $\pi/2$ at the mechanical resonance frequency Ω_m , and about $\pm\pi/4$ at $\Omega_m \pm \Omega_{\text{SQL}}$.

This motivates the use of frequency dependent squeezed states to reduce the displacement spectrum below the SQL over a broad frequency range, where every sideband frequency needs to be rotated by a different angle to minimize the displacement spectrum. More specifically, sideband noises contributing to both shot noise and radiation pressure noise need to be correlated in a frequency dependent manner to optimally cancel the total displacement noise in the vicinity of the mechanical resonance.

II.1.3 Frequency Dependent Squeezing in Optomechanical Cavities

We now consider a squeezed state with a frequency dependent angle whose covariance matrix is given by

$$\mathbf{S}_{\text{OPO}}^{\theta}[\Omega] = \begin{pmatrix} \cosh 2r + \sinh 2r \cos 2\theta[\Omega] & -\sinh 2r \sin 2\theta[\Omega] \\ -\sinh 2r \sin 2\theta[\Omega] & \cosh 2r - \sinh 2r \cos 2\theta[\Omega] \end{pmatrix}$$

The resulting displacement spectrum then reads

$$\begin{aligned} S_{xx}[\Omega] = & \mathcal{C}^{-2}(\cosh 2r - \sinh 2r \cos 2\theta[\Omega]) \\ & + \left(\frac{\mathcal{C}}{2}\hbar|\chi[\Omega]|\right)^2 (\cosh 2r + \sinh 2r \cos 2\theta[\Omega]) \\ & - \hbar|\chi[\Omega]| \sinh 2r \sin 2\theta[\Omega] \cos \phi_m[\Omega] \end{aligned} \quad (\text{II.17})$$

As shown in the annex, picking the squeezing angle as

$$2\theta[\Omega] = \arctan \left[\frac{2|\mathcal{K}[\Omega]| \cos \phi_m[\Omega]}{1 - |\mathcal{K}[\Omega]|^2} \right] \quad (\text{II.18})$$

minimizes the displacement spectrum at every sideband frequency, leading to

$$\begin{aligned} S_{xx}[\Omega] = & \cosh 2r \left(\mathcal{C}^{-2} + \left(\frac{\mathcal{C}}{2}\hbar|\chi[\Omega]|\right)^2 \right) \\ & - \sinh 2r \sqrt{\left(\mathcal{C}^{-2} - \left(\frac{\mathcal{C}}{2}\hbar|\chi[\Omega]|\right)^2 \right)^2 + \left(\hbar|\chi[\Omega]| \cos \phi_m[\Omega] \right)^2}. \end{aligned} \quad (\text{II.19})$$

This broadband reduction of the displacement spectrum below the SQL is illustrated in figure ???. However, for a resonant optomechanical cavity i.e. $\Delta = 0$, it is impossible to beat the SQL at the mechanical resonance, where the susceptibility is purely imaginary $\phi_m[\Omega_m] = \pi/2$.

Convergence to VIRGO/LIGO notation: We once again show that this general treatment converges to the one used in the context of gravitational wave detectors. In the free mass regime, $\mathcal{K}[\Omega]$ is real, such that $\phi_m[\Omega] = 0$. One can then rewrite the optimal squeezing angle as

$$2\theta[\Omega] = \arctan \left[\frac{2\mathcal{K}[\Omega]}{1 - \mathcal{K}^2[\Omega]} \right] = 2 \arctan \mathcal{K}[\Omega] \quad (\text{II.20})$$

where we used the identity $\arctan 2x/(1 - x^2) = 2 \arctan x \pmod{\pi}$, such that this comes down to the expression used in the context of gravitational wave detectors [harry_advanced_2010,

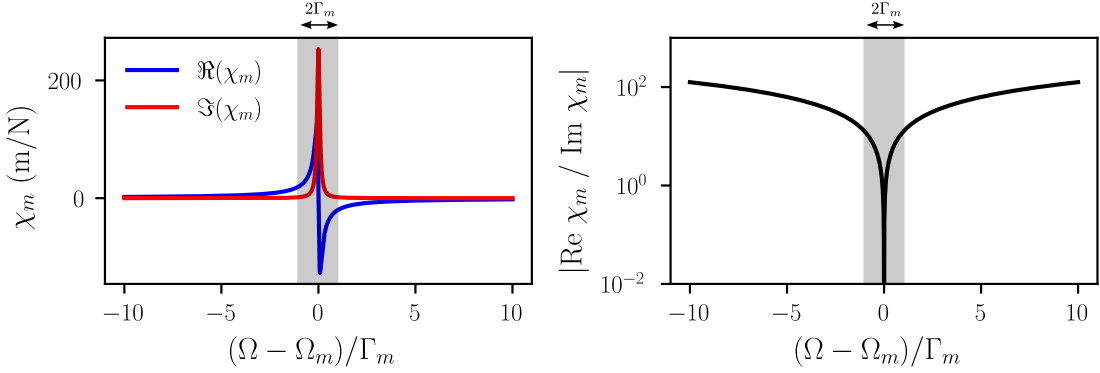


Fig. II.2 DYes

aasi_enhanced_2013]. Furthermore, the mechanical frequency and damping rate will be significantly smaller than the $\hbar\mathcal{C}^2/m$ term such that using the free-mass susceptibility $\chi[\Omega] = -1/m\Omega^2$ boils down the the SQL frequency to the known expression

$$\Omega_{\text{SQL}} = \sqrt{\frac{\hbar\mathcal{C}^2}{2m}} \implies \mathcal{K}[\Omega] = \left(\frac{\Omega_{\text{SQL}}}{\Omega}\right)^2 \quad (\text{II.21})$$

The displacement spectrum then reduces to the common expression

$$S_{xx}[\Omega] = \mathcal{C}^{-2} \left(1 + \left(\frac{\Omega_{\text{SQL}}}{\Omega}\right)^2\right) e^{-2r} \quad (\text{II.22})$$

which is the free-mass approximation result used in the GW community.

II.1.4 Filter Cavities for Frequency Dependent Squeezing

To generate frequency dependent squeezed states, one can use a detuned optical cavity called a filter cavity [5]. The principle is to reflect a frequency independent squeezed state off a single sided detuned cavity, such that only the sidebands resonant with the cavity will undergo a phase shift, effectively rotating the squeezing ellipse by a frequency dependent angle. The transfer matrix for a single sideband from a detuned single port cavity was given by

$$\kappa M_{\Delta}^{-1}[\Omega] - \mathbf{1} = \begin{pmatrix} \frac{\kappa/2 + i(\Delta + \Omega)}{\kappa/2 - i(\Delta + \Omega)} & 0 \\ 0 & \frac{\kappa/2 - i(\Delta - \Omega)}{\kappa/2 + i(\Delta - \Omega)} \end{pmatrix}$$

We recall from section II.1.4 that the reflected quadratures from a detuned cavity are

given by

$$\mathbf{T}_r[\Omega] = \frac{1}{(\kappa/2 - i\Omega)^2 + \Delta^2} \begin{pmatrix} (\kappa/2)^2 - \Delta^2 + \Omega^2 & -\kappa\Delta \\ +\kappa\Delta & (\kappa/2)^2 - \Delta^2 + \Omega^2 \end{pmatrix}$$

such that the phase picked up by sidebands at frequency Ω is given by

$$\phi_{fc}[\Omega] = \arctan\left(\frac{2\Delta\kappa}{\kappa^2/4 - \Delta^2 + \Omega^2}\right) \quad (\text{II.23})$$

II.2 Cavity Optomechanics with Membrane based systems

II.2.1 Classical Description

To gain intuition and derive elementary parameters used in the next section, we first describe the classical fields propagating in a three mirror cavity where a membrane with complex amplitude reflection and transmission coefficients $r_m = |r_m|e^{i\phi_r}$ and $t_m = |t_m|e^{i\phi_t}$ is placed between two high reflectivity mirrors of amplitude reflection coefficients ~ -1 . The membrane splits the cavity in two sub-cavities of lengths L_1 and L_2 , with $L = L_1 + L_2$ the total cavity length. The membrane is initially at mean position $x = 0$, and is modelled as a thin dielectric slab of thickness d and refractive index n , with amplitude reflection and transmission coefficients r_m and t_m given by [thompson_strong_2008]

$$r_m = \frac{(n^2 - 1) \sin knd}{2in \cos knd + (n^2 + 1) \sin knd}, \quad t_m = \frac{2n}{2in \cos knd + (n^2 + 1) \sin knd}. \quad (\text{II.24})$$

In the lossless case, we will assume the index of refraction n is real, such that $|r_m|^2 + |t_m|^2 = 1$. The right-moving mean field amplitudes in the left and right sub-cavities are denoted $\bar{\alpha}_L$ and $\bar{\alpha}_R$, while the left-moving mean field amplitudes are denoted $\bar{\alpha}'_L$ and $\bar{\alpha}'_R$. The cavity fields are then related by

$$\begin{aligned} \bar{\alpha}_R &= t_m \bar{\alpha}_L + r_m \bar{\alpha}'_R \\ \bar{\alpha}'_L &= t_m \bar{\alpha}'_R + r_m \bar{\alpha}_L. \end{aligned} \quad (\text{II.25})$$

In this case, energy conservation i.e. $|\bar{\alpha}_L|^2 + |\bar{\alpha}'_R|^2 = |\bar{\alpha}'_L|^2 + |\bar{\alpha}_R|^2$ imposes that $2(\phi_t - \phi_r) = \pi$ such that we can chose $r_m = |r_m|$ and $t_m = i|t_m|$. We rewrite the the cavity fields by injecting the identities $\bar{\alpha}_L = -\bar{\alpha}'_L e^{2ikL_1}$ and $\bar{\alpha}'_R = -\bar{\alpha}_R e^{2ikL_2}$ such that we get the useful system

$$\begin{aligned} (1 + |r_m|e^{2ikL_2})\bar{\alpha}_R &= -i|t_m|e^{2ikL_1}\bar{\alpha}'_L \\ (1 + |r_m|e^{2ikL_1})\bar{\alpha}'_L &= -i|t_m|e^{2ikL_2}\bar{\alpha}_R. \end{aligned} \quad (\text{II.26})$$

Resonance Frequencies

By eliminating the right and left fields in the above system, we arrive at the transcendental equation [6]

$$-\cos kL = |r_m| \cos(k\Delta L), \quad \text{with} \quad \Delta L = L_2 - L_1. \quad (\text{II.27})$$

Following the method in Sankey et al. [7], we now proceed to derive the cavity resonance frequencies as a function of the membrane position x around its mean position $x = 0$. We will also always consider a long cavity such that $L \gg \lambda, x$. The cavity sublengths considering a non zero mean membrane position are then $L_1 \rightarrow L_1 + x$ and $L_2 \rightarrow L_2 - x$. It follows that $\Delta L \rightarrow \Delta L - 2x$. We will consider the effect of this displacement on the cavity wavenumbers/frequencies as a perturbation $k(x) = k_N + \delta k(x)$ with $k_N = N\pi/L$, that is the membrane displacement does not change the longitudinal mode index N but modulates it by at most π/L (or equivalently by one empty cavity FSR in the frequency domain). We will omit the x dependency in both k and δk for ease of notation. It then follows that terms in $k L$ and $k x$ can be expanded as

$$\cos(kL) = (-1)^N \cos(\delta k L) \quad \text{and} \quad \cos(kx) \sim \cos(k_N x)$$

where we assumed that $\delta k x \sim 0$. The transcendental equation becomes

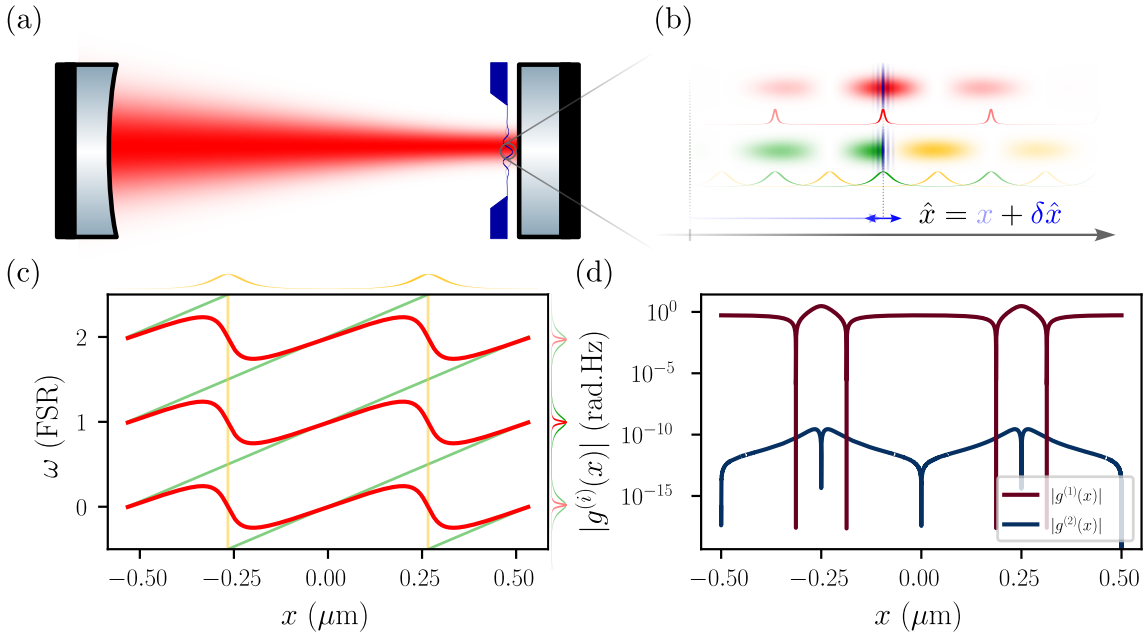
$$(-1)^{N+1} \cos(\delta k L) = |r_m| \cos(k_N \Delta L) \left[\cos(\delta k \Delta L) \cos(2k_N x) + \sin(\delta k \Delta L) \sin(2k_N x) \right] \quad (\text{II.28})$$

and where we simplified the sines terms already equal to zero. We will now consider the Membrane At The Edge (MATE) model where $L_1 \sim L \gg L_2 \rightarrow \Delta L \sim L$. Solving for δk reinjecting in the dispersion relation $\omega_c(x) = ck(x)$ leads to

$$\omega_c(x) \simeq \omega_{FSR} \left(N + \frac{1}{\pi} \arctan \left(-\frac{1 + |r_m| \cos 2k_N x}{|r_m| \sin 2k_N x} \right) \right) \quad (\text{II.29})$$

where $\omega_{FSR} = \pi c/L$ is the empty cavity free spectral range. When the laser is resonant with the cavity, we then substitute $N\omega_{FSR}$ and k_N by ω_0 and k the laser angular frequency and wavenumber. Taking the derivatives of these resonance frequencies with respect to the membrane position x gives the linear and quadratic dispersive optomechanical couplings $G^{(1)}(x) = \partial\omega_c/\partial x$ and $G^{(2)}(x) = \partial^2\omega_c/\partial x^2$ as

$$\begin{aligned} G^{(1)}(x) &= \frac{2|r_m|k_N\omega_{FSR}}{\pi} \frac{|r_m| + \cos(2k_N x)}{1 + |r_m|^2 - 2|r_m| \cos(2k_N x)} \\ G^{(2)}(x) &= -\frac{4|r_m|k_N^2\omega_{FSR}}{\pi} \frac{|r_m|(1 - |r_m|^2) \sin(2k_N x)}{(1 + |r_m|^2 - 2|r_m| \cos(2k_N x))^2} \end{aligned} \quad (\text{II.30})$$

Fig. II.3 $rrlist = 0.7, L = 3e-2,$

Cavity transmission and reflection

From the system in (II.26), and having derived just above the resonant cavity wavevectors k , we can compute the power ratio of the two sub-cavity fields as a function of x when the MATE system is on resonance. This is

$$\frac{|\bar{\alpha}_R|^2}{|\bar{\alpha}'_L|^2} = \frac{P_R}{P_L} = \frac{1 + 2|r_m| \cos(2kL_1 + 2kx) + |r_m|^2}{1 - |r_m|^2}. \quad (\text{II.31})$$

with $P_{L,R} \propto |\bar{\alpha}_{L,R}|^2$. It then follows that the the power fraction leaking from the left and right mirrors, i.e. the resonant reflection and transmission coefficients $R(\Delta = 0, x)$ and $T(\Delta = 0, x)$ are given by

$$\begin{aligned} R(\Delta = 0, x) &= \frac{|t_1|^2 P_L}{|t_1|^2 P_L + |t_2|^2 P_R} \\ &= \frac{|t_1|^2 (1 - |r_m|^2)}{|t_1|^2 (1 - |r_m|^2) + |t_2|^2 (1 + |r_m|^2 + 2|r_m| \cos 2kx)} \\ T(\Delta = 0, x) &= \frac{|t_2|^2 P_R}{|t_1|^2 P_L + |t_2|^2 P_R} \\ &= \frac{|t_2|^2 (1 + |r_m|^2 + 2|r_m| \cos 2kx)}{|t_1|^2 (1 - |r_m|^2) + |t_2|^2 (1 + |r_m|^2 + 2|r_m| \cos 2kx)} \end{aligned} \quad (\text{II.32})$$

and we get the expected relation $R(\Delta = 0, x) + T(\Delta = 0, x) = 1$.

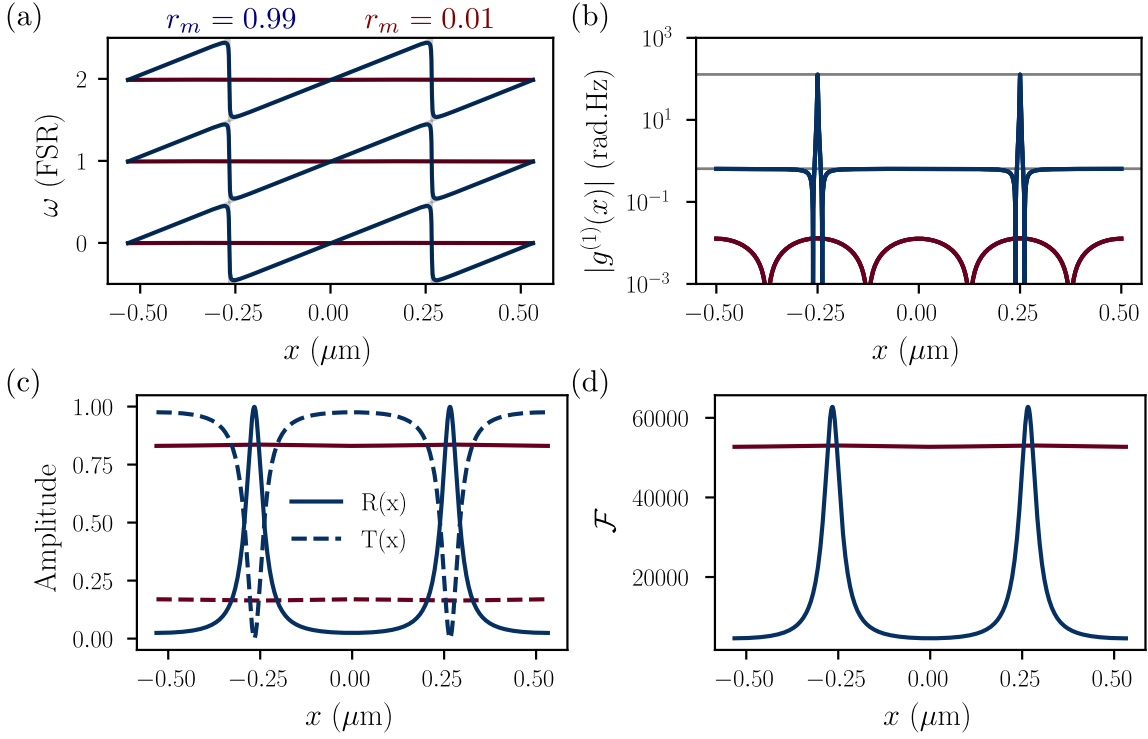


Fig. II.4 $rrlist = [0, 0.1, 0.9]$, $T1 = 100\text{ppm}$, $T2=20\text{ppm}$, $L = 2\text{e-}2$,

Cavity Linewidth and Finesse

To derive the position dependent cavity linewidth $\kappa(x)$ and finesse $\mathcal{F}(x)$, we once again resort to the Sankey et al. method [7]. The total energy stored in the cavity is given by

$$E = \frac{2(L_1 + x)}{c} P_L + \frac{2(L_2 - x)}{c} P_R \quad (\text{II.33})$$

and the rate at which energy leaves the cavity

$$\partial_t E = -|t_1|^2 P_L + -|t_2|^2 P_R \quad (\text{II.34})$$

such that the cavity energy decay rate is given by

$$\begin{aligned} \kappa(x) &= -\frac{\partial_t E}{E} = \frac{c(|t_1|^2 + |t_2|^2 P_R/P_L)}{2(L_1 + x) + 2(L_2 - x)P_R/P_L} \\ &= \frac{c|t_1|^2(1 - |r_m|^2) + c|t_2|^2(1 + |r_m|^2 + 2|r_m|\cos 2kx)}{2(L_1 + x)(1 - |r_m|^2) + 2(L_2 - x)(1 + |r_m|^2 + 2|r_m|\cos 2kx)}. \end{aligned} \quad (\text{II.35})$$

We can then derive the cavity finesse as

$$\mathcal{F}(x) = \frac{\pi c}{L\kappa(x)}. \quad (\text{II.36})$$

II.2.2 Quantum Description

We now turn to the quantum description of the membrane based optomechanical system. A question that naturally arises is how to describe best this three mirror cavity quantum mechanically: should we consider two independent optical modes in each subcavity, coupled by photon tunneling through the membrane? Or should we consider the whole cavity as a single optical mode, whose resonance frequency is modified by the membrane position (and given above)?

Two Cavity Mode Model

We start by looking at the two cavity model. Using the same tools as in section II.2, we can derive the QLE of a membrane based optomechanical system. The membrane position now turns into an operator such that $\hat{x} \propto \hat{c} + \hat{c}^\dagger$ with \hat{c} the mechanical annihilation operator as in the previous section. As seen above, the membrane position modifies the resonance frequencies of the two subcavities, such that they both depend on the membrane position as $\omega_L(x)$ and $\omega_R(x)$ but with inverse trend: when one cavity shortens and its FSR increases, the other lengthens and its FSR decreases. To first order, we can linearize the resonance frequencies as

$$\omega_L(\hat{x}) \simeq \omega_L + G_L \hat{x}, \quad \omega_R(\hat{x}) \simeq \omega_R + G_R \hat{x}, \quad (\text{II.37})$$

with $\omega_{L,R}$ the unperturbed resonance frequencies of the subcavities and $G_L = \omega_L/L_1$ and $G_R = -\omega_R/L_2$ their respective optomechanical couplings. The whole system features a network of optical modes varying linearly with the membrane position, coupled by the membrane transmission.

In Vincent Dumont's PhD work, quadratic points (where $G^{(1)} = 0$ and $G^{(2)} \neq 0$) were the centerfold of the study, in the high membrane reflectivity regime [[dumont_cavity_2017](#)]. It was then sufficient to consider two optical modes coupled by photon tunneling through the membrane.

However, in our case, we focus on the sole dispersive coupling regime in the MATE configuration, and we additionally consider a low membrane reflectivity. The optimal point to do so is when the first long cavity is on resonance, and when the short one is anti-resonant. With a lowered reflectivity, the coupling between subcavity modes increases, lead-

ing to larger mode splittings at the avoided crossings, until the two subcavities are fully hybridized into new cavity modes spanning both subcavities [**thompson_strong_2008**, **thompson_coupling_2013**].

The short cavity being precisely at an anti-node, it is equally probable for the tunneled photons from the long cavity to populate two short cavity modes on either side of the anti-node. We then need to describe the system by a single long cavity mode coupled to two short cavity modes, as illustrated in figure II.5. We introduce the annihilation operators \hat{a}_L for the long cavity mode, and \hat{a}_{R+} and \hat{a}_{R-} for the two short cavity modes on either side of the anti-node. The Hamiltonian of this system can then be written as

$$\begin{aligned}\hat{H} = & \hbar(\omega_L + G_L x) \hat{a}_L^\dagger \hat{a}_L + \hbar(\omega_{R-} - G_R x) \hat{a}_{R-}^\dagger \hat{a}_{R-} + \hbar(\omega_{R+} - G_R x) \hat{a}_{R+}^\dagger \hat{a}_{R+} & (= \hat{H}_\gamma) \\ & + \hbar\Omega_m \hat{c}^\dagger \hat{c} & (= \hat{H}_m) \\ & + \hbar G_L \hat{a}_L^\dagger \hat{a}_L \delta\hat{x} - \hbar G_R (\hat{a}_{R+}^\dagger \hat{a}_{R+} + \hat{a}_{R-}^\dagger \hat{a}_{R-}) \delta\hat{x} & (= \hat{H}_{\text{OM}}) \\ & - \hbar J [\hat{a}_L^\dagger (\hat{a}_{R+} + \hat{a}_{R-}) + (\hat{a}_{R+}^\dagger + \hat{a}_{R-}^\dagger) \hat{a}_L] & (= \hat{H}_{\text{tun}})\end{aligned}$$

where $J = c|t_m|/2\sqrt{L_1 L_2}$ is the photon tunneling rate through the membrane [**thompson_strong_2008**], and where we linearized the position as before as $\hat{x} = x + \delta\hat{x}$. The first line describes the free evolution of the subcavity modes, the second one the mechanical resonator, the third the optomechanical interaction between the membrane position and the subcavity modes, and the last the photon tunneling through the membrane. As before, the commutation relations are given by

$$[\hat{a}_L, \hat{a}_L^\dagger] = [\hat{a}_{R\pm}, \hat{a}_{R\pm}^\dagger] = [\hat{c}, \hat{c}^\dagger] = 1 \quad \text{and} \quad [\hat{a}_L, \hat{a}_{R\pm}] = [\hat{a}_L, \hat{a}_{R\pm}^\dagger] = 0$$

We will only consider the photonic part of the Hamiltonian, as to put it in matrix form such that we can diagonalize it and work in the basis of the new eigenmodes. Furthermore, we go the frame rotating at frequency $\omega_0 = \omega_{R-} = \omega_L$ i.e. when the long cavity mode is degenerate with the left short cavity mode, such that the photonic Hamiltonian becomes

$$\hat{H}_\gamma = \hbar G_L x \hat{a}_L^\dagger \hat{a}_L - \hbar G_R \left(x + \frac{\lambda}{4} \right) \hat{a}_{R-}^\dagger \hat{a}_{R-} + \hbar \left(\omega_{FSR} - G_R \left(x - \frac{\lambda}{4} \right) \right) \hat{a}_{R+}^\dagger \hat{a}_{R+} \quad (\text{II.38})$$

and we can rewrite both the photonic and tunneling hamiltonian i.e. the photonic manifold in matrix form as

$$\hat{H}_\gamma + \hat{H}_{\text{tun}} = \hbar \begin{pmatrix} \hat{a}_L^\dagger & \hat{a}_{R-}^\dagger & \hat{a}_{R+}^\dagger \end{pmatrix} \mathbf{M} \begin{pmatrix} \hat{a}_L \\ \hat{a}_{R-} \\ \hat{a}_{R+} \end{pmatrix} \quad (\text{II.39})$$

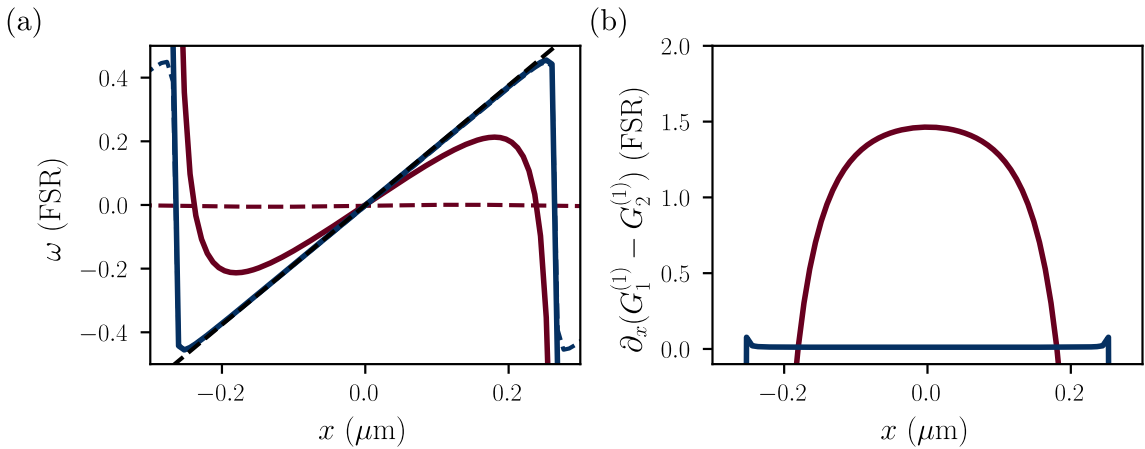


Fig. II.5 0.01, 0.99

with

$$\mathbf{M} = \begin{pmatrix} G_L x & -J & -J \\ -J & -G_R(x + \lambda/4) & 0 \\ -J & 0 & \omega_{FSR} - G_R(x - \lambda/4) \end{pmatrix}.$$

One could then diagonalize this 3×3 matrix to get the new eigenmodes of the system, and rewrite the optomechanical interaction in this new basis. In the limit where the membrane transmittivity is high such that $|t_m| \sim 1$ and $|r_m| \ll 1$, the tunneling rate J becomes much larger than both optomechanical couplings $\tilde{G}_{L,R} x$ and the free spectral range ω_{FSR} . The cumberstone expression of the eigenmodes is not displayed here, but is equivalent to considering an system's eigenstate described by a annihilation operator \hat{a} with optomechanical coupling $G^{(1)}(x)$ and decay rate $\kappa(x)$ as derived in the previous section. The system's Hamiltonian can then be written as

$$\hat{H} = \hbar\omega_c(x = \lambda/4)\hat{a}^\dagger\hat{a} + \hbar\Omega_m\hat{c}^\dagger\hat{c} + \hbar G^{(1)}(x)\hat{a}^\dagger\hat{a}\hat{x} \quad (\text{II.40})$$

Single Mode Model

If the membrane is more transmissive than reflective, one could ask if the system could be described by a single optical mode, whose resonance frequency is weakly perturbed by the membrane position as derived in the previous section. In this case, the Hamiltonian of the system reads

$$\hat{H} = \hbar\omega_c(x)\hat{a}^\dagger\hat{a} + \hbar\Omega_m\hat{c}^\dagger\hat{c} \quad (\text{II.41})$$

where $\omega_c(x)$ is given by the expression derived above. This description is then matching the two mode model in the limit of highly reflective membranes as seen in figure ??, as well as

in the limit of low reflectivity membranes where the subcavities are fully hybridized.

Comparison to Single Mode Model

Since we are interested in the dispersive coupling regime in the MATE configuration with a low reflectivity membrane, such that we will operate the system where the linear dispersive coupling is dominant over quadratic dispersive coupling and dissipative coupling, we need to compare which model is best suited to describe the system.

Obviously the two mode model breaks down in the limit of low reflectivity membranes where the subcavities are fully hybridized, and the single mode model is then more appropriate. In the opposite limit of highly reflective membranes, both models converge to the same description as seen above. Regarding the radiation pressure force acting on the membrane, in the two mode model, the radiation pressure force is given by the sum of the forces exerted by each subcavity mode as $\hat{F}_{rp} = -\hbar G_L \hat{a}_L^\dagger \hat{a}_L + \hbar G_R (\hat{a}_{R+}^\dagger \hat{a}_{R+} + \hat{a}_{R-}^\dagger \hat{a}_{R-})$. In the single mode model, the radiation pressure force is given by $\hat{F}_{rp} = -\hbar \partial \omega_c(x) / \partial x \hat{a}^\dagger \hat{a}$. In the limit of highly reflective membranes, the two mode model radiation pressure force is then more appropriate since the optical mode is split in two subcavity modes, each exerting a force on the membrane. In the opposite limit of low reflectivity membranes where the subcavities are fully hybridized and where we focus on the dispersive coupling regime, it would genuinely be of no interest when studying radiation pressure effects, and a relevant description of the radiation pressure force is tricky to derive (because there are actually photons in both subcavities, but the model breaks down). In our middle ground case of moderately reflective membranes, we will assume the optical mode is mostly localized in the long cavity mode such that the single mode description is valid, and that the radiation pressure force is given by the derivative of the cavity resonance frequency with respect to the membrane position as seen in the textbook case of a single mirror cavity. The same QLEs as in the previous chapter can then be derived and used in our case.

Chapter III

Experimental Methods

This chapter essentially covers feedback control techniques used in Chapter IV and V. It is thought as a practical guide to the implementation of various locking schemes using the LKB *home grown* control software PyRPL. The chapter begins with a general introduction to feedback control, PI controllers and error signal requirements. It then details specific locking techniques used in this work, with an emphasis on experimental aspects. For in depth technical description of the PyRPL working principle, we refer the reader to Chapter III or Leonard Neuhaus thesis [[Neuhauser_Thesis_2021](#)], as well as the PyRPL documentation [[PyRPL_Docs](#)] and original article [[PyRPL_Article](#)]. Some figures are adapted from this last reference (with authorization)

Contents

III.1 Feedback control	72
III.1.1 Overview	72
III.1.2 Proportion-Integral (PI) Controllers	73
III.1.3 PyRPL overview	75
III.1.4 IQ modules	77
III.2 Locking techniques	79
III.2.1 Temperature Lock	80
III.2.2 Optical phase Lock	80
III.2.3 Cavity Locks	81
III.2.4 Offset Frequency Locks and Phase Lock Loop	84

III.1 Feedback control

A central aspect of experimental quantum optics is the ability to stabilize various parameters of an optical setup against environmental fluctuations. These parameters include cavity lengths, laser frequencies, optical phases, and temperatures of nonlinear crystals, which all undergo unwanted drifts and noise due to thermal, acoustic, and mechanical perturbations. To achieve this stabilization, feedback control systems are employed, which rely on generating an error signal that quantifies the deviation from a desired setpoint. This error signal is then processed by a controller to compute a corrective feedback signal that drives an actuator to counteract the disturbance and maintain the parameter at its target value.

III.1.1 Overview

A feedback control loop then aims to stabilize the behaviour of a physical system that is continuously subject to disturbances. When the system may be linearized around its operating point, its response to a harmonic perturbation at angular frequency ω_0 is fully characterized by its complex transfer function $G(\omega)$. We denote by $V_{\text{exc}}(t)$ the real excitation applied to the system, taken to be sinusoidal,

$$V_{\text{exc}}(t) = A_{\text{exc}} \cos(\omega_0 t), \quad (\text{III.1})$$

with amplitude A_{exc} . In the frequency domain the system is described by its complex transfer function

$$G(\omega) = |G(\omega)| e^{i\phi(\omega)}, \quad (\text{III.2})$$

which specifies the amplitude response $|G(\omega)|$ and the phase shift $\phi(\omega)$ experienced by a sinusoid at frequency ω . The relation between input and output is expressed most naturally in complex notation. Writing the excitation as the real part of a complex exponential,

$$V_{\text{exc}}(t) = \text{Re}\left\{ A_{\text{exc}} e^{i\omega_0 t} \right\} \implies V_{\text{meas}}(t) = \text{Re}\left\{ G(\omega_0) A_{\text{exc}} e^{i\omega_0 t} \right\}$$

so that explicitly

$$V_{\text{meas}}(t) = |G(\omega_0)| A_{\text{exc}} \cos(\omega_0 t + \phi(\omega_0)). \quad (\text{III.3})$$

Thus the physical output remains real, while the complex transfer function $G(\omega_0)$ determines how the amplitude and phase of the input harmonic are modified.

In-phase and quadrature decomposition.

It is convenient to decompose the transfer function into its in-phase (I) and quadrature (Q) components such that Eq. (III.3) can be written as

$$V_{\text{meas}}(t) = I(\omega_0) \cos(\omega_0 t) + Q(\omega_0) \sin(\omega_0 t), \quad (\text{III.4})$$

which forms the basis of IQ demodulation. By multiplying $V_{\text{meas}}(t)$ by $\cos(\omega_0 t)$ and $\sin(\omega_0 t)$ and low-pass filtering the results with a filter $H_f(\omega)$ with a cutoff frequency $\omega_f \ll \omega_0$, one obtains the slowly varying quadratures $I(t)$ and $Q(t)$, from which the complex baseband signal

$$s_{\text{meas}}(t) = I(\omega_0) + i Q(\omega_0) \quad (\text{III.5})$$

is constructed.

Obviously, realistic excitation signals are never pure sinusoids, such that they can be decomposed into a superposition of harmonic components

$$V_{\text{exc}}(t) = \text{Re} \left\{ \int_0^\infty \frac{d\omega}{2\pi} A_{\text{exc}}(\omega) e^{i\omega t} \right\}.$$

where $A_{\text{exc}}(\omega)$ is the complex amplitude of the component at angular frequency ω . Demodulating the measured signal at a frequency ω_0 and low pass filtering it yields a measured signal given by

$$\begin{aligned} s_{\text{meas}}(t) &= \int_0^\infty \frac{d\omega}{2\pi} G(\omega - \omega_0) H_f(\omega) A_{\text{exc}}(\omega - \omega_0) e^{i\omega t} \\ &= I(t) + i Q(t) \end{aligned} \quad (\text{III.6})$$

such that the IQ demodulation produces time-dependent quadratures $I(t)$ and $Q(t)$, whose complex combination $s_{\text{meas}}(t)$ represents the slowly varying complex envelope.

In a feedback loop, a relevant observable derived from $s_{\text{meas}}(t)$ is fed into the controller and is denoted $s_{\text{in}}(t)$. Depending on the application, $s_{\text{in}}(t)$ may correspond to one of the quadratures, the reconstructed phase, or any real-valued function of (I, Q) .

III.1.2 Proportion-Integral (PI) Controllers

Now that both quadratures are accessible through the IQ demodulation, and that we obtained a signal $s_{\text{in}}(t)$ relevant for the control task at hand, we need to extract an error signal $\varepsilon(t)$ that quantifies the deviation from a desired setpoint at which we wish to *lock* the system.

It is typically expressed as the difference between a measured signal and its reference value:

$$\varepsilon(t) = s_{\text{in}}(t) - s_{\text{ref}}, \quad (\text{III.7})$$

where $s_{\text{in}}(t)$ is the physical quantity monitored in the experiment, and s_{ref} is the target value.

For effective feedback stabilization, this error signal must satisfy several essential criteria listed below.

High SNR: Near the setpoint, $\varepsilon(t)$ should exhibit a high SNR to ensure robust locking and minimize the influence of technical and electronic noise.

Linearity and antisymmetry: The error signal should be linear and antisymmetric in a neighborhood of the operating point. Small deviations from the setpoint should produce a proportional response in $\varepsilon(t)$, with opposite signs for deviations of opposite direction.

Monotonicity and uniqueness: The slope $\partial\varepsilon/\partial x$, where x denotes the control parameter (e.g., cavity length or laser frequency), should be monotonic and unambiguous near the lock point to avoid multiple equilibrium points and ensure stable locking behavior.

Steep slope near the setpoint: A steeper slope improves sensitivity to small deviations and enhances lock accuracy, although it must be balanced against potential noise amplification.

Bandwidth compatibility: The spectral content of $\varepsilon(t)$ must be compatible with the bandwidth of the actuator and the dynamics of the system. For example, in the case of a piezoelectric transducer, which acts as a low-pass mechanical element, the error signal high-frequency components won't be compensated by the actuator.

A standard way to achieve this stabilization is to use a Proportion-Integral (PI) controller. The PI controller computes the feedback signal $u(t)$ from the error signal $\varepsilon(t)$ according to:

$$s_{\text{out}}(t) = K_P \varepsilon(t) + K_I \int_0^t \varepsilon(\tau) d\tau \quad (\text{III.1})$$

where K_P and K_I are the proportional and integral gains, respectively. The proportional term $K_P \varepsilon(t)$ responds to the current error and primarily acts on mid-frequency deviations, enabling rapid corrections. The integral term $K_I \int \varepsilon(\tau) d\tau$ accumulates past errors and is most effective at low frequencies, helping to eliminate long-term drifts and steady-state off-

sets.

In classical control theory, PID (Proportional-Integral-Derivative) controllers are designed to stabilize dynamic systems by combining three terms: a proportional term for immediate response, an integral term to eliminate steady-state error, and a derivative term that anticipates future error based on the rate of change. However, in practical experimental setups—particularly in quantum optics—PI control (Proportional-Integral) is typically sufficient and even preferable to full PID control. The derivative term, which acts predominantly at high frequencies, is generally unnecessary and can be counterproductive. This is because the feedback actuator is often a piezoelectric transducer, which exhibits non-zero capacitance. Combined with the finite output impedance of the control electronics, this forms a natural low-pass filter that significantly attenuates high-frequency components of the feedback signal. As a result, any derivative term—which primarily targets high-frequency correction—would be both ineffective due to this filtering and potentially harmful by injecting high-frequency noise into the loop.

Therefore, PI control offers a balanced and robust approach: the integral term suppresses low-frequency drifts (typically below a few Hz to tens of Hz), the proportional term corrects intermediate-frequency deviations (up to a few kHz), and high-frequency components (above the mechanical resonance or actuation bandwidth) are naturally filtered out and deliberately left uncorrected. This allows for stable feedback while preserving high-frequency signals—such as thermal noise or mechanical sidebands—which carry essential physical information for analysis and measurement.

III.1.3 PyRPL overview

With the rise of digital signal processing, many feedback control systems have transitioned from analog electronics to software-based implementations. One such powerful and flexible platform is PyRPL (Python Red Pitaya Lockbox), an open-source software suite designed for real-time digital signal processing and feedback control using the Red Pitaya (RP) hardware and developed in our team. PyRPL provides a user-friendly interface for implementing various control algorithms, including PI controllers, and is now widely used in experimental physics laboratories across the world [[PyRPL_Article](#), [PyRPL_Docs](#)]. While we refer the reader to Leonhard Neuhaus' thesis [[Neuhauser_Thesis_2021](#)] and the PyRPL documentation [[PyRPL_Docs](#)] for an in-depth technical description of the PyRPL working principle, we will concisely summarize the main performance metrics and high abstraction blocks relevant for this work.

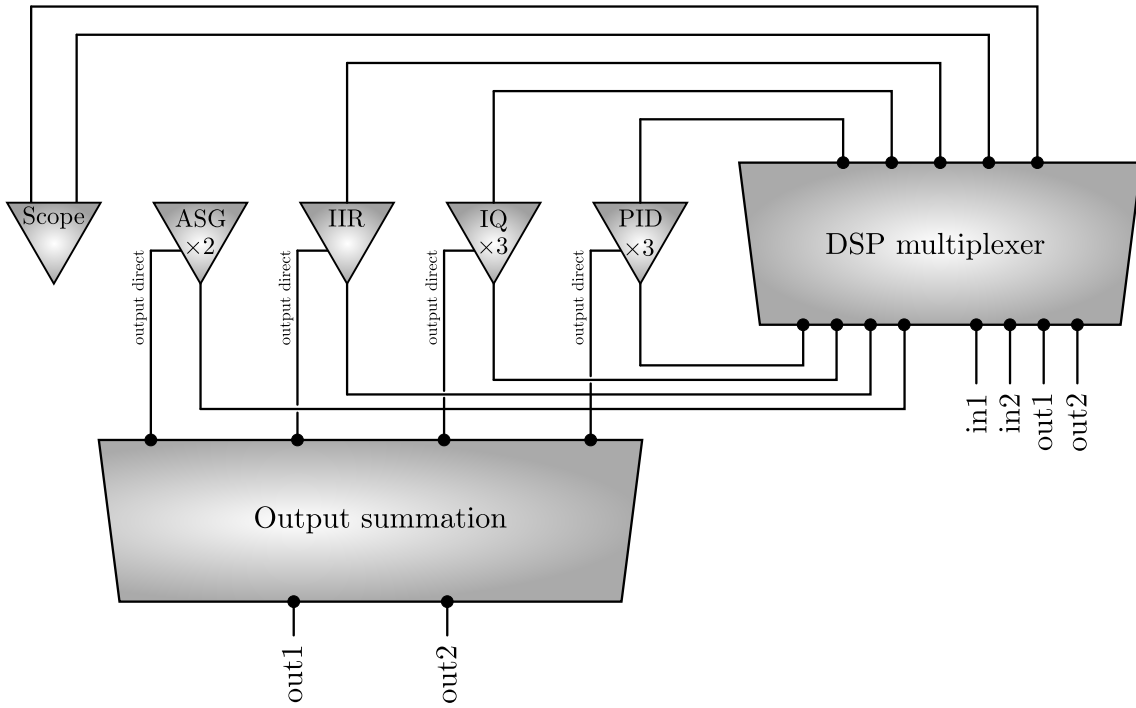


Fig. III.1 coucou

Red Pitaya is a compact FPGA-based platform that combines high-speed analog-to-digital (ADC) and digital-to-analog (DAC) converters with a powerful FPGA for real-time signal processing. The onboard ADCs and DACs operate at a 125 MHz sampling rate with 14-bit nominal resolution, which enables the digitization and synthesis of signals up to about 60 MHz according to the Nyquist criterion. In practice, the effective resolution is about 12 bits for the ADC and 11 bits for the DAC, which remains more than sufficient for precision photodetection, modulation, and error-signal processing in quantum optics. A notable limitation is the digitization noise floor, as well as the noise added from the voltage shifter, bounding the output to $\pm 1V$. Sensible improvement of the order of 5 dBm/Hz can be achieved in the 100 Hz - 1 MHz frequency range by unsoldering the voltage shifter circuit, as well as taking of the regulator from the board and powering the Red Pitaya with a low noise external voltage source. Taking the voltage offset off actually makes the output range 0-2V, ideal as to not feed (high voltage amplified) negative voltages to our piezoelectric actuators (which would kill them). This modification was performed on all RPs used in this work, bringing the noise floor down to 140dBm/Hz at 1MHz. In the frequency range relevant to experimental quantum optics (from a few kHz to a few hundred kHz), the RP noise floor is remarkably close—within 10–15 dB—to that of high-end laboratory lockboxes

and diagnostic instruments. Above 1 MHz, however, professional RF analyzers remain significantly quieter and cleaner. 10dB for a fraction of the cost is a fair trade off in our opinion.

PyRPL leverages this hardware to implement various digital signal processing tasks. The modules available in PyRPL are a scope, a spectrum analyser, 2 Arbitrary Signal Generators (ASG), 3 PID controllers, 3 IQ modules, an Infinite Impulse Response (IIR) filter module, and 4 pulse width modulation modules (pwm). These modules can be interconnected in a flexible manner to create complex feedback loops tailored to specific experimental needs, by simply rerouting the signal flow either in a programmatic way using the PyRPL Python API, or graphically through the PyRPL GUI. The signal flow architecture is illustrated in figure III.1, where one can see how the various modules can be interconnected. This makes PyRPL a very versatile and cheap tool for monitoring and piloting a wide range of experimental setups.

An additional experimental tricks to circumvent the number of output issues (2 DAC channels only) is to use the slow analog outputs of the RP, which need to be soldered manually to BNC/SMA outputs. These outputs send 4 0-1.8V signals synthesized from filtered pwm signals, have a sensibly noisier floor as well as a limited bandwidth (up to \sim 100kHz only), but are very useful for sending DC offsets as well as slow feedback signals. Additionally, we make extensive use of minicircuits bias tess to direct both slow and RF signals to the same output, as to be able to artificially double the number of output channels (2 RF + 2 DC).

III.1.4 IQ modules

We now turn more specifically to the PyRPL IQ modules, which can be used for various purposes. Using the Python API or the GUI, one can select which input channel (in1 or in2) is fed to the IQ module. Similarly, one can chose to which output channel (out1 or out2) the processed signal is sent. In between, various registers allow the user to manipulate the input signal as desired. The latent available operations of the mpdule are illustrated in figure III.2. The input signal can first be high pass filtered to eventually remove DC offsets. It is then mixed with the $\cos \omega_0 t$ and $\sin \omega_0 t$ signals discussed above, with an additional phase shift ϕ that can be set by the user. They are then lowpass filtered to yield the in-phase and quadrature components $I(t)$ and $Q(t)$. Finally, these quadratures can be manipulated in various ways before being sent to the output channel, or sent to other modules such as the scope or the spectrum analyzer for diagnostic purposes.

Filters: setting the various registers as in fig III.3(a), one can choose to lowpass, highpass

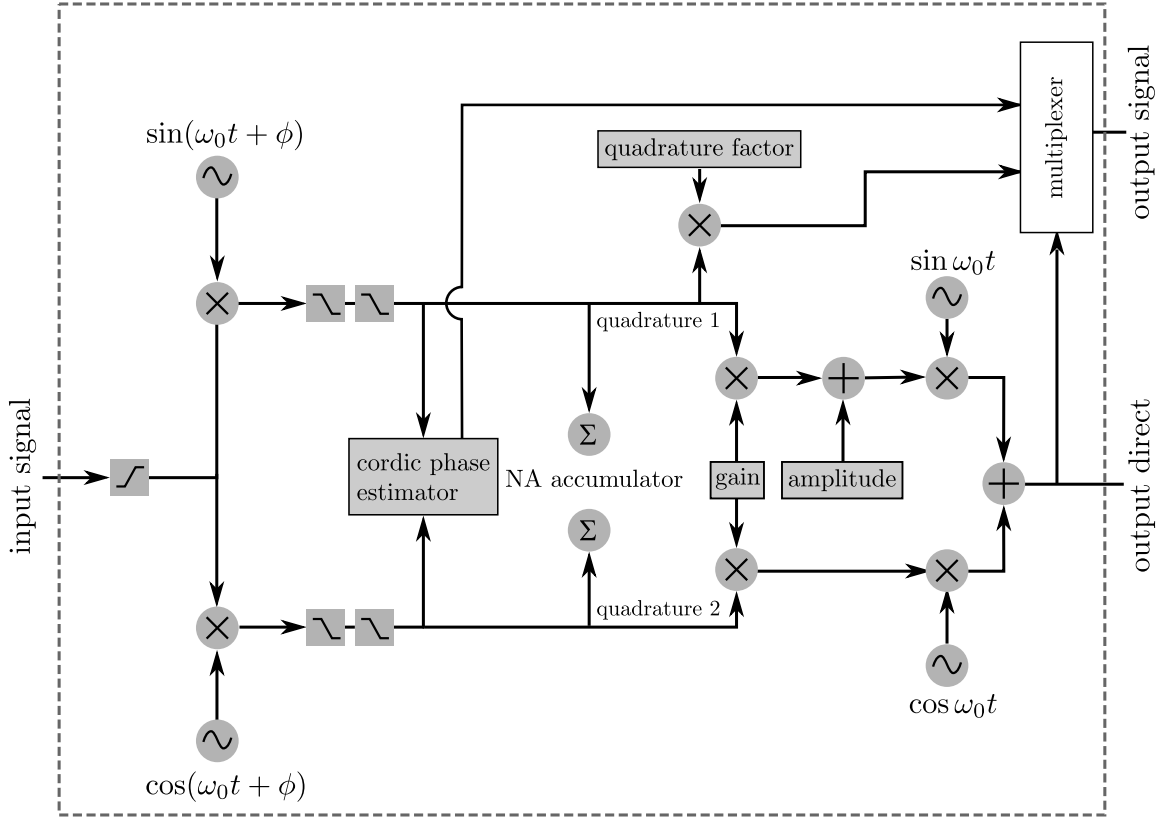


Fig. III.2 Basic working principle of the IQ module in PyRPL. One can set any register value using either the GUI or the Python API to manipulate the input signal as desired.

or bandpass an input signal by choosing the cutoff frequencies the filter orders.

Network Analyzer: by setting the registers as in fig III.3(b), one can use the IQ module as a network analyzer. The input signal is swept over a user-defined frequency range, and the in-phase and quadrature components are recorded at each frequency step. This allows to reconstruct the complex transfer function of a system connected to the input channel, which is very useful for characterizing the response of feedback loops.

Phase Lock Loop: by setting the registers as in fig III.3(c), one can use the IQ module as a phase lock loop (PLL). The phase of the input signal is continuously monitored through the IQ demodulation, and a feedback signal is generated. This error signal then needs to be routed to the PID modules to lock the phase to a desired reference value. This is particularly useful for stabilizing optical phases in interferometric setups, as well as implemental frequency offset locks and PLLs.

Error Signals - Lock-in Detection: by setting the registers as in fig III.3(d), one can use the IQ module to generate error signals for feedback control. The user can select which quadrature (I or Q) is sent to the output channel, as well as apply additional processing such as scaling, offsetting, or filtering. A modulation with known phase relationship to the demodulated signal can be sent off to an EOM, and AOM or a PZT to implement locks. This allows to tailor the error signal to the specific requirements of the feedback loop, ensuring optimal performance and stability.

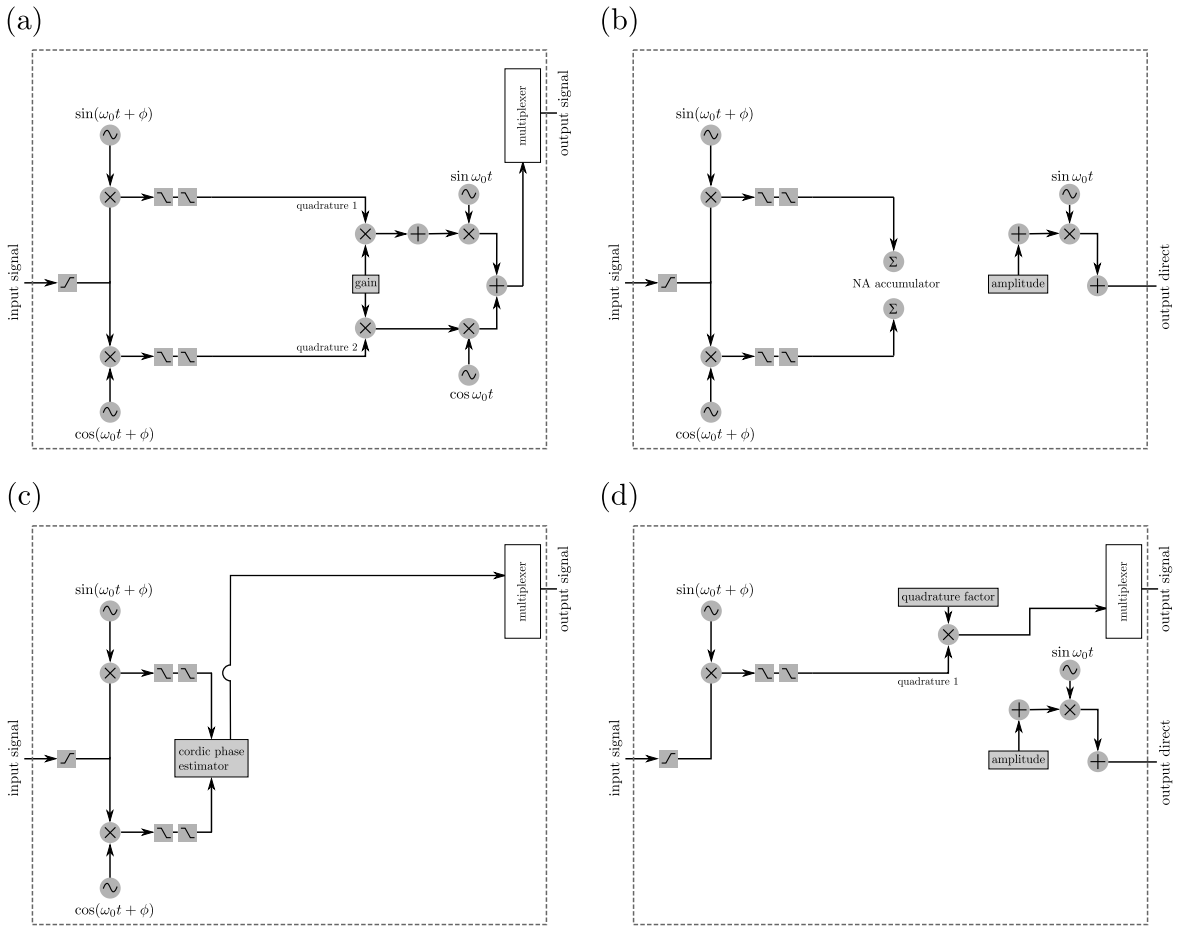


Fig. III.3 coucou

III.2 Locking techniques

We now proceed to give a list of the various locks used in this work, along with their practical implementation as well as their error signal expression. The details of the derivations of the error signals are given in Appendix B.

III.2.1 Temperature Lock

A first example of a PI lock used in this work is the temperature lock, which is used to stabilize the temperature of non linear crystals embedded inside optical cavities. The error signal is derived from a temperature sensor, such as a thermistor, which measures the temperature of the crystal and simply written as:

$$\varepsilon(\Delta T) \propto \Delta T \quad (\text{III.8})$$

where $\Delta T = T_{\text{meas}} - T_{\text{set}}$. The error signal is then fed into a PI controller, which adjusts the heating element, a peltier module in our case, to maintain the desired temperature setpoint. In the case of our SHG, temperature lock is actually performed using a commercial temperature controller provided along the PPLN crystal array provided by Covision. Similarly, the OPO crystal temperature is stabilized using a Thorlabs temperature controller (TED???) connected to a thermistor and a peltier module, the RP just allowing us to module the lock point by feeding an offset voltage to the temperature controller.

A full PyRPL lock has however been implemented on the quantum thermometry experiment led by Tristan Briant, and the details of this implementation can be found in the thesis of Emile Ferreux. The RP wiring diagram is shown in figure III.4.

The temperature lock is crucial for maintaining the phase matching conditions in nonlinear optical processes (developped in the next section), such as second-harmonic generation or optical parametric oscillation, where the efficiency of frequency conversion depends sensitively on the crystal temperature. By stabilizing the temperature, we ensure that the nonlinear interactions remain optimal, leading to consistent and reproducible results in experiments involving squeezed light generation or other nonlinear optical phenomena.

III.2.2 Optical phase Lock

Controlling the relative path length between two arms of an interferometer is a fundamental technique in quantum optics. The basic idea is to use the interference of light from two paths to lock the phase difference between them. Although not being the same experiential setups, Michelson interferometers, Mach-Zhender interferometers, and Local Oscillator stabilization error signals fall in the same category as they are derived from the same principle. Namely,

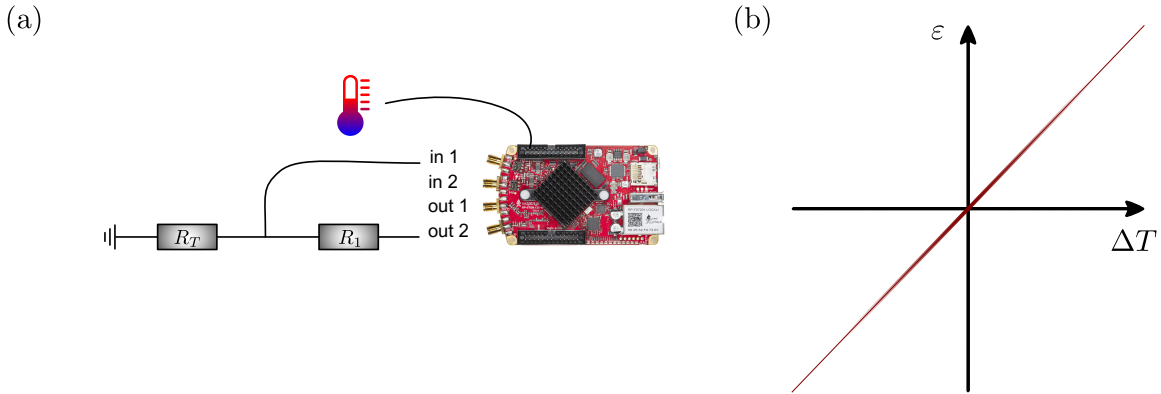


Fig. III.4 coucou

the error signal is proportional to the sine of the phase difference between the two arms:

$$\varepsilon(\Delta\phi) \propto \sin(\Delta\phi) \simeq \Delta\phi \quad (\text{III.9})$$

where $\Delta\phi = \phi_a - \phi_b$ is the phase difference between the two optical paths. Analogically, we would need to add an adjustable voltage offset, as to be able to tune the error signal to zero at the desired phase difference, before seeding this error signal to the PI block. Digitally, this is performed by adding a constant offset to the error signal, which can be adjusted to set the desired phase difference.

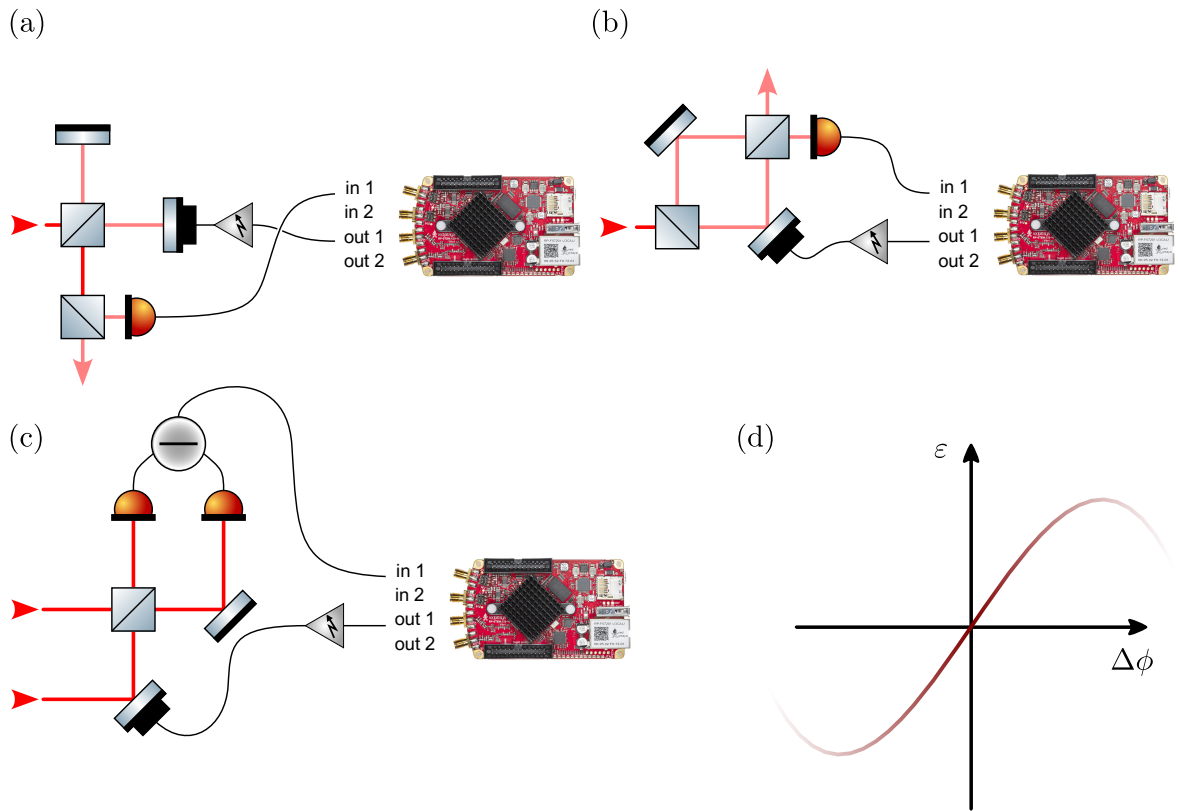
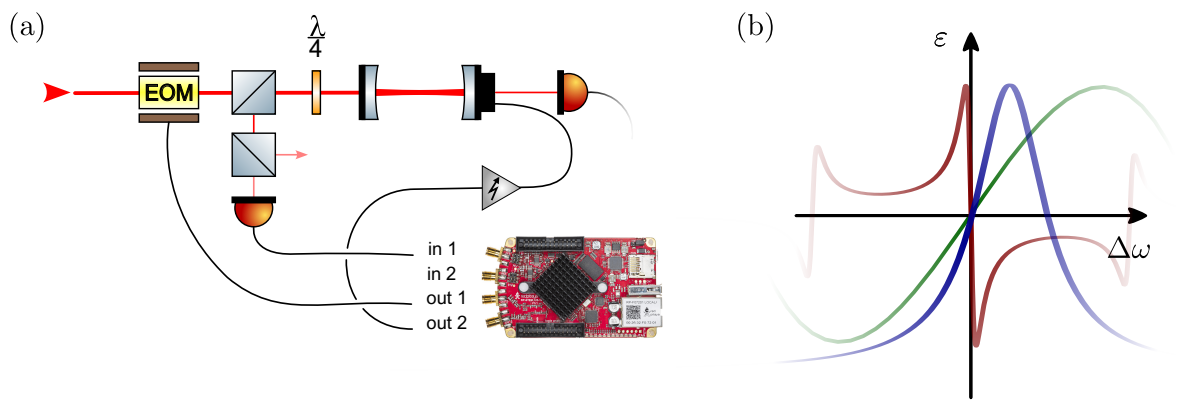
In practice, this is implemented by mounting a mirror on which one of the arms is reflected, and then using a piezoelectric transducer to control the position of the mirror, hence modulating the relative phase between the two optical paths. The piezo is then feedback controlled through a PI loop, which adjusts the voltage applied to the piezo to set the error signal to 0. The RP wiring diagram is shown in figure III.5.

III.2.3 Cavity Locks

We now turn to the locking of optical cavities, and will develop 3 techniques used in this work: the side of fringe lock, the dither lock and the Pound-Drever-Hall (PDH) lock. The RP wiring and the typical error signal shapes are shown in figure III.6.

Side of Fringe

A lorentzian dip does not qualify as a valid error signal to lock the cavity on resonance, according to the requirements listed above, as it is symmetric around resonance. However,

Fig. III.5 *coucou*Fig. III.6 *coucou*

by locking the cavity on the side of the resonance fringe, one can obtain a usable error signal that is linear and antisymmetric in a small neighborhood around the lock point. This technique is known as the *side of fringe* lock. The error signal near resonance is then given by

$$\varepsilon(\Delta\omega) \propto (\Delta\omega - \Delta_{\text{lock}}) \quad (\text{III.10})$$

where the Δ_{lock} is the detuning at which the cavity is locked. In PyRPL, calibrating the lorentzian dip in transmission or reflection allows to set the lock point in units of the cavity linewidth, which is very convenient. This would also allow to explore off resonant optomechanical effects, such as optical spring and damping.

The side of fringe lock is almost always used in this work as a preliminary step to bring the cavity close to resonance before engaging a more sophisticated lock such as PDH or dither lock. However, it is less robust and sensitive compared to other techniques, making it less suitable for long-term stabilization or high-precision applications.

Dither lock

A first technique to lock an optical cavity on resonance is the dither lock. The basic idea is to impose a small sinusoidal modulation modulating the cavity resonant frequency, typically by applying a phase modulation using an EOM, or by modulating the cavity length using a piezoelectric actuator. Linking this to the IQ section above, we would modulate the cavity at frequency $\omega_0 \lesssim \kappa$ with κ the cavity linewidth, and demodulate the reflected or transmitted signal at the same frequency using an IQ module. The error signal is then proportional to the in-phase or quadrature component of the demodulated signal, depending on the demodulation phase chosen. The error signal near resonance is then given by

$$\varepsilon(\Delta\omega) \propto \Delta\omega \quad (\text{III.11})$$

This technique is relatively simple to implement and can provide a robust lock, although it may introduce additional noise due to the imposed modulation. The modulation frequency and depth need to be carefully chosen to optimize the lock performance while minimizing the impact on the system's dynamics. This technique has the advantage of being implementable with the transmitted signal of the cavity (while PDH requires the reflected signal), since the modulation frequency is lower than the cavity linewidth (otherwise the sidebands would only be reflected).

Pound-Drever-Hall Lock

The second method to lock an optical cavity on resonance is the Pound-Drever-Hall (PDH) technique [Black_PDH_2001], which can be used to lock a laser frequency to a stable optical cavity, or conversely to lock the cavity length to a stable laser frequency. The method relies on imposing phase modulation sidebands on the laser field outside the cavity bandwidth this time, typically using an electro-optic modulator (EOM), and using these sidebands as phase-stable references. Because they lie far outside the cavity linewidth ($\Omega_{\text{mod}} \gg \kappa$), the sidebands are reflected nearly unchanged: $r(\omega_\ell \pm \Omega_{\text{mod}}) \approx 1$. In contrast, the carrier field near resonance acquires a frequency-dependent phase shift upon reflection, captured by the complex cavity reflection coefficient $r_c(\delta)$. The PDH error signal is obtained by detecting the reflected beam and demodulating the photocurrent at the modulation frequency, isolating the beat terms between carrier and sidebands. The resulting signal is proportional to the *imaginary part* of $r_c(\delta)$, which varies antisymmetrically with detuning and provides a zero-crossing error signal ideal for linear feedback. The error signal near resonance is then given by

$$\epsilon(\Delta\omega) \propto \Im(r_c(\Delta\omega)) \simeq \Delta\omega \quad (\text{III.12})$$

This imaginary component encodes the rapid phase dispersion near resonance that allows the system to discriminate the sign and magnitude of frequency deviations. In contrast, the real part of $r_c(\delta)$, being symmetric around resonance, does not yield a usable error signal. The PDH lock is generally preferred to the dither lock due to its superior sensitivity, larger linear range, and reduced susceptibility to technical noise.

The *demodulation phase* plays a critical role in selecting the appropriate quadrature of the signal for feedback. Since the beat signal between the carrier and sidebands has both in-phase and quadrature components, choosing the correct demodulation phase ensures that the extracted error signal aligns with the imaginary part of the reflection coefficient. A misaligned demodulation phase can lead to mixing of the symmetric (real) part into the error signal, thereby reducing sensitivity and introducing offset or distortion near the lock point. In practice, the demodulation phase is optimized empirically—either via a variable phase shifter in the electronic demodulation path or by adjusting the physical delay in the reference oscillator—to maximize the slope of the error signal at zero-crossing, corresponding to pure detection of the dispersive component.

III.2.4 Offset Frequency Locks and Phase Lock Loop

Finally, we discuss the implementation of frequency offset locks and phase lock loops (PLL) using the IQ modules in PyRPL. These techniques are essential for stabilizing the frequency offset and the relative phase of the beatnote between two lasers. The RP wiring diagram is

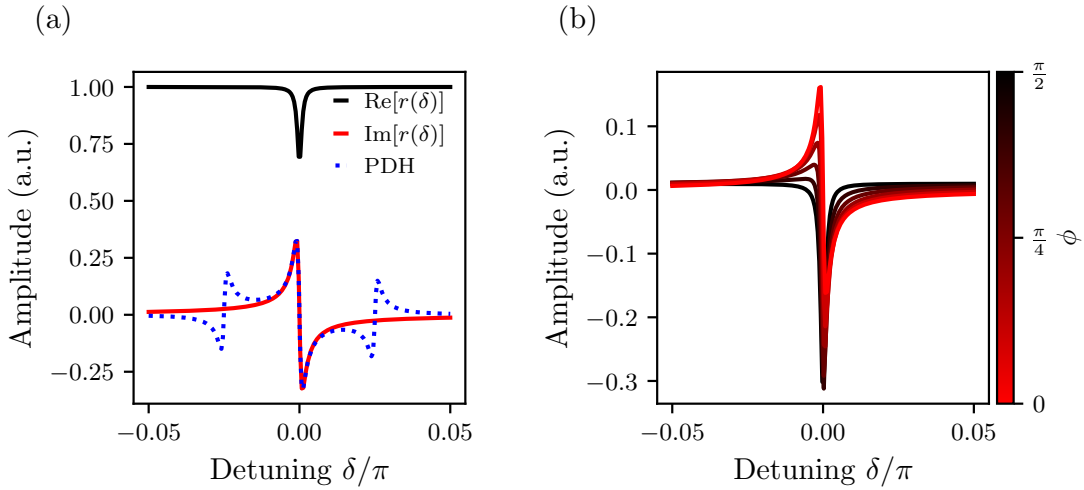


Fig. III.7 Schematic of the Pound-Drever-Hall (PDH) locking technique. The laser passes through an electro-optic modulator (EOM) generating phase modulation sidebands. The modulated beam is incident on the optical cavity, and the reflected light is detected by a photodiode (PD). The photocurrent is demodulated at the modulation frequency to produce the PDH error signal, which is fed to a PI controller driving the cavity actuator (e.g., piezo). Key components are labeled: EOM (electro-optic modulator), PD (photodiode), LO (local oscillator for demodulation), and PI (proportional-integral controller).

shown in figure III.8.

The basic principle is to detect the beatnote between two lasers on a fast photodiode,

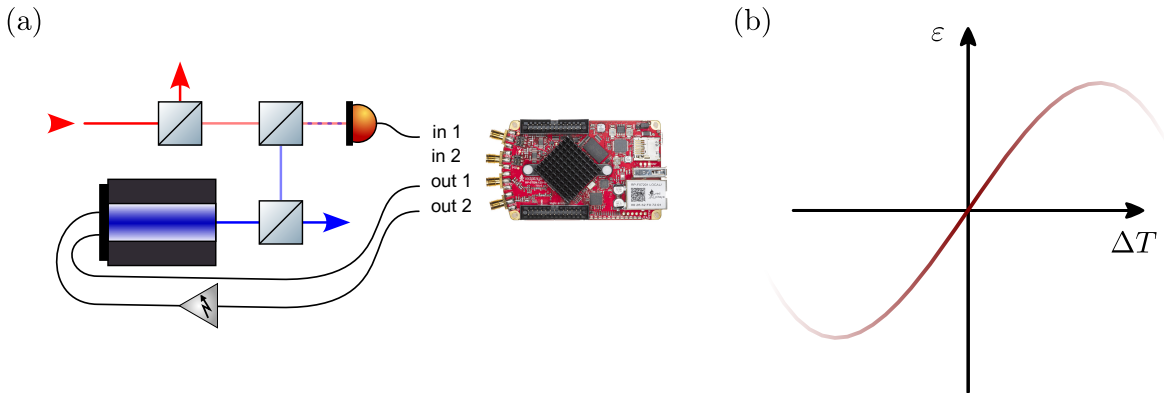


Fig. III.8 coucou

and to demodulate this signal using an IQ module at a frequency close to the desired offset frequency. The error signal is then derived from one of the quadratures of the demodulated

signal. The error signal near the lock point is then given by

$$\varepsilon(\Delta\omega_{\text{beat}}) \propto \Delta\omega_{\text{beat}} \quad (\text{III.13})$$

where $\Delta\omega_{\text{beat}} = \omega_{\text{beat}} - \omega_{\text{ref}}$ is the deviation of the beatnote frequency from the reference frequency. This error signal is then fed into a PI controller, which adjusts the frequency of one of the lasers (typically via a piezoelectric actuator or current modulation) to maintain the desired offset frequency.

As explained before, a high voltage piezoelectric actuator has a limited bandwidth, typically up to a few kHz, due to the naturally occurring lowpass filtering effect of the piezo capacitance and the output impedance of the driving electronics. To overcome this limitation, we resort to the so called floating ground technique, which consists in locking both the piezo actuator through a standard PI loop, as well as locking the piezo ground to a higher frequency without amplifying it (or using an Operational Amplifier with high bandwidth i.e. OP27? 37?). This technique effectively extends the bandwidth of the piezo actuator up to a few tens of kHz, allowing for more robust and stable locks. Additionally, the laser current or temperature (the case here), is also locked to ensure the piezo remains in its mid-range of operation. Although not detailed in figure III.8, the temperature can be locked using the PyRPL PWM module, such that the modulated pwm signal (duty cycle) is sent to the laser temperature controller. The heating element of the laser will then naturally lowpass filter the pwm signal, providing a smooth and stable temperature control. This dual feedback approach enhances the overall stability and performance of the frequency offset lock and PLL.

Chapter IV

Experiments: Optomechanics

This chapter will cover the experimental methods used in the development of optomechanical three-mirror cavity systems, focusing on the design, fabrication, and characterization of mechanical resonators within optical cavities. The methods are designed to enhance the sensitivity of measurements in quantum optics and optomechanics.

Contents

IV.1 System Description and Setup	88
IV.1.1 Previous LKB work and Motivation	88
IV.1.2 Specifications and Design	89
IV.1.3 Flexure Actuation	93
IV.1.4 Experimental Setup	95
IV.1.5 Alignment Procedures	97
IV.2 Experimental Characterization	97
IV.2.1 Cavity Scans	97
IV.2.2 Cavity Locking and Mechanical Characterization	106
IV.2.3 Bistability	109
IV.3 Design of an Optomechanical Fibered Cavity	109
IV.3.1 Design considerations	109

Over the past two decades, optomechanical systems have greatly benefited from advancements in optical coating technologies, enabling the realization of high-finesse cavities ($\mathcal{F} > 10^5$)[\[coating_review\]](#). Simultaneously, progresses in micro/nanofabrication allowed the making of mechanical structures with high Q factors ($> 10^6$)[\[nanofab_review\]](#). Despite these achievements, a significant challenge remained: fabricating mechanical elements that possess both high Q and high reflectivity, as optical, mechanical and thermal effects often degrade system performance and hinder ultra-sensitive measurements[\[optomech_challenges\]](#).

IV.1 System Description and Setup

IV.1.1 Previous LKB work and Motivation

Previous optomechanics experiments at LKB have primarily utilized Fabry–Pérot cavities with two mirrors, where the end mirror of the cavity was typically a HR mirror deposited on top of a mechanical structure featuring a mechanical mode of interest [[<empty citation>](#)].

Over Aurélien’s and Leonard’s PhD works, the group in collaboration with ONERA developed a platform based on a 1-mm-thick quartz micropillar with an effective mass of $33 \mu\text{g}$. The structure supports a fundamental compression mode oscillating at 3.6 MHz, with a mode shape as shown in Fig. ???. Using a dry-film photoresist technique, a $100 \mu\text{m}$ diameter high-reflectivity mirror was deposited on one end of the pillar. Careful design of the suspension has yielded mechanical quality factors up to 3×10^6 at room temperature and up to 7×10^7 below 1 K. When integrated into a $50 \mu\text{m}$ -long Fabry–Pérot cavity with a custom-fabricated coupling mirror, finesse exceeding 10^5 were achieved. Importantly, this compact cavity remains robust against vibrations of the dilution refrigerator and maintains alignment during cooldown, thereby providing a stable platform to study optomechanical effects in the intermediate mass regime. [limitations and why it didnt work](#)

Then over Rémi’s and Michael’s PhD, another resonator was developed in collaboration with Francesco Marin’s team, based on a suspended silicon disk. The device operates in a balanced mode, where the central disk vibrates in opposition to four surrounding counterweights. By adjusting the geometry, the resonance frequency was increased to 280 kHz, corresponding to an effective mass of about $110 \mu\text{g}$, bringing the system closer to the micropillar parameters. A HR mirror was then deposited on top using the same technique as the micropillar. Finesse of about ~ 50000 were then reached. At cryogenic temperature, optimized designs reached mechanical quality factors on the order of 1.2×10^6 .[limitations and why it didnt work](#)

Although the systems ended up being limited by various factors mentioned above (optical, mechanical and thermal effects) [<empty citation>], the parts designed over the years did feature a high level of passive stability as well as good thermalization properties. A pivotal solution, introduced by Regal, Kimble, Harris, and collaborators[Harris2008, 8], was to decouple these requirements by embedding a high- Q mechanical resonator within a high-finesse optical cavity, using the optical field to probe and control the resonator's dynamics.

IV.1.2 Specifications and Design

It was then decided to build on this design and extend it to a three-mirror cavity in a MATE configuration to benefit from this large linear and tunable coupling range as detailed in the previous chapter. That is the work Michael and myself undertook during my M2 internship and the following years of my PhD. This new three mirror cavity then needed to fulfill various requirements detailed in what follows.

High Finesse

Low loss mirrors were produced by **Jérôme DEGALLAIX** and **David HOFMAN** at the *Laboratoire des Matériaux Avancés* (LMA, Lyon) using ion-beam-sputtered (IBS) Bragg stacks made of Ta_2O_5 (high index, $n \approx 2.09$) and SiO_2 (low index, $n \approx 1.46$)[AmatoPhD, LMA_IBS]. The coatings were deposited in the LMA's *Veeco SPECTOR* chambers and subsequently annealed at 500°C for 10 hours to minimise both optical (absorption) and mechanical losses, following the recipe of Amato *et al.* [AmatoPhD]. ¹.

We supplied the LMA with a batch of substrates with various radii of curvature to explore different cavity geometries. The requested specifications are summarized in the table below. The total round-trip scatter and absorption losses are usually below 20 ppm, in agreement with the measurements reported (absoption ~ 0.7 ppm, scattering ~ 10 ppm)in Ref. [AmatoPhD].

Substrate type	Laseroptik ID	R	Front-side HR T	Back-side AR
Plane	S-00798	∞ (plane)	20 ± 45 ppm	$R \lesssim 100$ ppm
Plano-concave	S-00128	-25 mm	$100, 50 \pm 10$ ppm	$R \lesssim 100$ ppm
Plano-concave	S-00127	-15 mm	$100, 50 \pm 10$ ppm	$R \lesssim 100$ ppm
Plano-concave	S-00126	-10 mm	$100, 50 \pm 10$ ppm	$R \lesssim 100$ ppm

Table IV.1: Specifications of supplied Laseroptik substrates for different cavity geometries.

The quarter-wave design is centred at $\lambda = 1064$ nm for normal incidence. After annealing, the measured mechanical loss angle of the $\text{TiO}_2:\text{Ta}_2\text{O}_5/\text{SiO}_2$ stack is $\phi < 4 \times 10^{-4}$ at 1 kHz

¹Identical optics are used for the Advanced LIGO, Advanced Virgo and KAGRA interferometers[LIGO_optics].

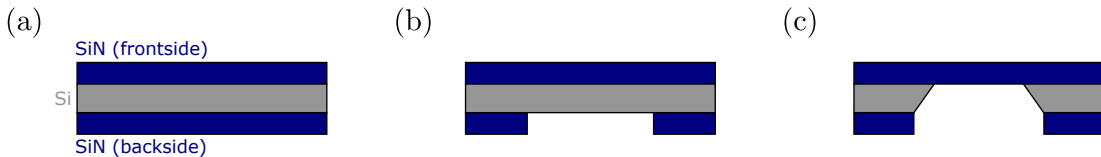


Fig. IV.1 *Fabrication steps of the SiN membrane resonator used in the MATE cavity. (a) starting from a silicon wafer coated with SiN on both sides. (b) lithography and RIE to open a square window in the top SiN layer. (c) KOH wet etching from the opened side until the cavity breaks through, leaving a free-standing SiN membrane. The membrane is then cleaned using HF to remove any residuals from the fabrication process.*

[link to mechanical damping needed](#), supporting cavity finesse in the range $200\,000 - 500\,000$ before excess scatter or absorption dominates[**AmatoPhD**].

High Q factor

Two different square membranes were used in the MATE cavities, both made of high-stress silicon nitride (Si_3N_4), a material known for its excellent mechanical properties, including high tensile stress and low intrinsic mechanical loss, making it ideal for optomechanical applications[**SiN_review**], and of nominal side lengths $l_n \times l_m = 500\,\mu\text{m} \times 500\,\mu\text{m}$.

The first membrane was made in-house at LKB by **Thibaut Jacqmin** and **Himanshu Patange** during Himanshu's PhD work. The silicon wafer was $350\,\mu\text{m}$ thick, and the SiN layers thicknesses was nominally 100 nm. Starting with the silicon wafer/chip coated with SiN on both sides, a photoresist is patterned by lithography to define a square window. Reactive-ion etching (RIE) then opens a square window through the top SiN layer. The exposed silicon is then wet-etched in KOH from the opened side until the cavity breaks through, leaving a released, free-standing SiN membrane spanning the opening. The membrane is then cleaned using HF to remove any residuals from the fabrication process. This very process etches the SiN layer as well, resulting in a final membrane thickness of less than 100nm. For detailed fabrication steps, refer to Himanshu's PhD thesis[**PatangePhD**]. We nonetheless succinctly display the fabrication steps in Fig IV.1.

The second membrane is a commercially Norcada® (NX10050AS)[**SiN_review**, **Norcada_datasheet**] SiN square membrane, specifically marketed as a *high Q* standard membrane for optomechanics applications. It features a Silicon frame of $200\,\mu\text{m}$ thickness, and a SiN layer of nominal thickness 50 nm. Regarding the quality factor, literature reports:

- **Room temperature.** Measurements on nominally identical Norcada membranes report quality factors $Q \sim 5 \times 10^6$ at $\approx 1\,\text{MHz}$ in $< 10^{-6}\,\text{mbar}$ vacuum [**SiN_review**,

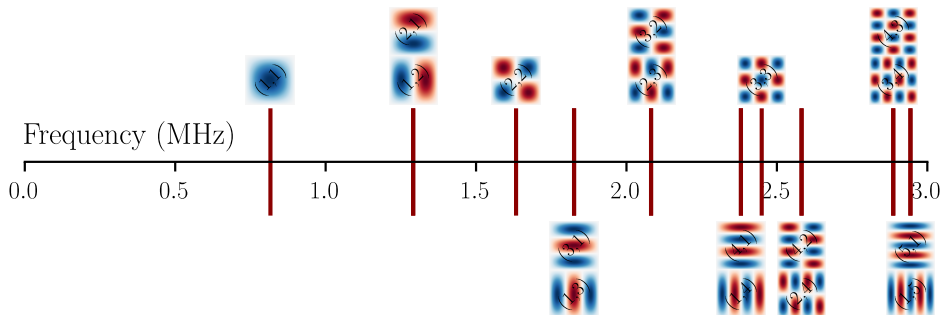


Fig. IV.2 Simulated mode shapes and frequencies of a square SiN membrane of side length $500\mu m$ under high tensile stress ($\sigma \sim 1 GPa$).

Norcada_datasheet].

- **Cryogenic operation.** Cooling to $T \lesssim 300$ mK reduces internal friction by an order of magnitude, with $Q > 10^7$ routinely observed [SiN_cryogenic].

The membrane's high stress, thin-film nature and dielectric composition make it fully compatible with ultra-high-vacuum environments and repeated cryogenic cycling, while introducing (a priori) negligible optical loss in the cavity. The expected mechanical mode structure can be derived from

$$f_{n,m} = \sqrt{\frac{\sigma}{4\rho} \left(\left(\frac{n}{l_n}\right)^2 + \left(\frac{m}{l_m}\right)^2 \right)} \quad (\text{IV.1})$$

with $\rho \sim 3 \text{ g/cm}^3$ the film mass density, $\sigma \sim 1 \text{ GPa}$, (n, m) the mode indices, and (l_n, l_m) the membrane side lengths. Considering a square membrane of identical side lengths of $500 \mu\text{m}$ yields a fundamental mode frequency at $f_{1,1} \sim 816 \text{ kHz}$, with the two higher order modes $(1, 2)$ and $(2, 1)$ degenerate at $f_{1,2} \sim f_{2,1} \sim 1.29 \text{ MHz}$ etc.. We display the first few mode shapes and expected frequencies in Fig. IV.2.

Optical alignment

The cavity is designed to be compatible with the Thorlabs® cage system. The input mirror is mounted on a 3 axis cage mount, allowing for easy alignment of the input mirror with respect to the cavity optical axis. Both the resonator and the back mirror are embedded within a custom-made holder, which is itself integrated into the cage system. The relative tilt between the resonator and the back mirror is adjusted using a set of 3 screws with a very fine thread, allowing for a fine alignment of the parallelism of the back cavity. The alignment procedure is detailed in section ??.

Dynamical range

The input mirror is glued to a PI Ceramic® P-016.00H ring-stack piezoelectric actuator using vacuum epoxy (Torr Seal®). Driven from 0 to +1000 V it provides a longitudinal stroke of 5 μm , a blocking force of 2.9 kN, as well as an unloaded resonance of 144 kHz, making it suitable for fast, low-noise cavity-length control.

The end-mirror–membrane assembly is mounted on a custom holder actuated by three PD080.31 piezo chips arranged mechanically in series. Each chip yields 2 μm of travel over a drive range of -20 to +100 V; the triple stack therefore supplies roughly 6 μm of coarse tuning while preserving high stiffness and sub-microsecond response. The effective range is lower than this owing to the fact the piezo is constrained within the holder. Furthermore, one should not constrain the piezo to much to avoid damaging it: it happened that the assembly was too tightly screwed in such that it ended up fracturing the piezo pushing against the back mirror holder. An easy workaround would be to add some elastic spacer between the piezo and the copper piece (like kapton tape for example).

Combining the 5 μm stroke of the front P-016.00H with the 6 μm range of the rear triple stack provides an overall cavity-length adjustment sufficient to scan few FSRs, as well as to tune the membrane position over a full wavelength, thus accessing allowing exploration of the three mirror cavity physics.

Compactness & Stability

The entire assembly is built as a cage system using standard Thorlabs® cage parts, allowing for a compact and stable assembly. The cage system also allows for (relatively) easy alignment of the mirrors, as well as easy access to the piezo actuators.

Vacuum and Cryogenic compatibility

The back cavity composed of the back mirror and the middle mirror is embedded inside an Oxygen Free Copper (OFHC) assembly with a circular geometry, eventually mitigating for transverse misalignment issues when going to cryogenic temperatures, the constraints compensating themselves radially with respect to the symmetry axis of the cavity assembly[[OFHC_review](#)]. Furthermore, the screws used to hold the assembly together are made of brass with a thermal expansion coefficient lower than that of the OFC, tightening up the cavity when reaching cryogenic temperatures. Thorlabs cage parts are compatible with moderate vacuum operation down to $\sim 10^{-7}$ mbar if properly degreased and ultrasound cleant, but a custom cryocompatible system to hold the input mirror would be needed for

operation at cryogenic temperatures.

The initial design of the cavity was made using Autodesk Fusion 360, allowing for a detailed 3D model of the entire assembly, including the piezo actuators, the mirrors and the cage system. The design was then exported to a STEP file format, which was used to manufacture the parts using a 3 axis CNC milling machine and a digital lathe. The pieces were machined by **Carounagarane DORE** and **Gael COUPIN** at the LKB mechanical workshop with $100\mu\text{m}$ tolerance. A detailed view of the cavity design and assembly is shown in Fig. IV.3.

IV.1.3 Flexure Actuation

One specificity of the MATE system is that the back cavity is significantly shorter than the front cavity, which would require high precision in both the machining of the copper pieces and the positioning of the resonator. In our case, we aim at a centimetric cavity which would require to position the membrane at roughly hundreds of microns from the back mirror, and parallel to the back mirror. Moving the membrane independently from the back mirror while maintaining a controllable tilt between both planes is therefore challenging.

A smart workaround was introduced by Jack Sankey and its group [9], where the authors introduced a flexure-tuned MATE system. The key innovation lies in actuating the membrane position by flexing its supporting silicon frame rather than translating the entire mount. This is done by mounting the back cavity in a semi-monolithic fashion, and 'locking' the silicon frame of the membrane using three screws with a fine thread, allowing for a fine adjustment of the angle of the membrane plane with respect to the back mirror plane. The piezos pushing on the back of the assembly then force the silicon frame constrained by the screws to bend, thus displacing the membrane with respect to the back mirror, as shown in Fig. IV.4. This approach preserves the cavity alignment for gentle flexures, while enabling continuous and wide-range tuning of both the membrane displacement and tilt.

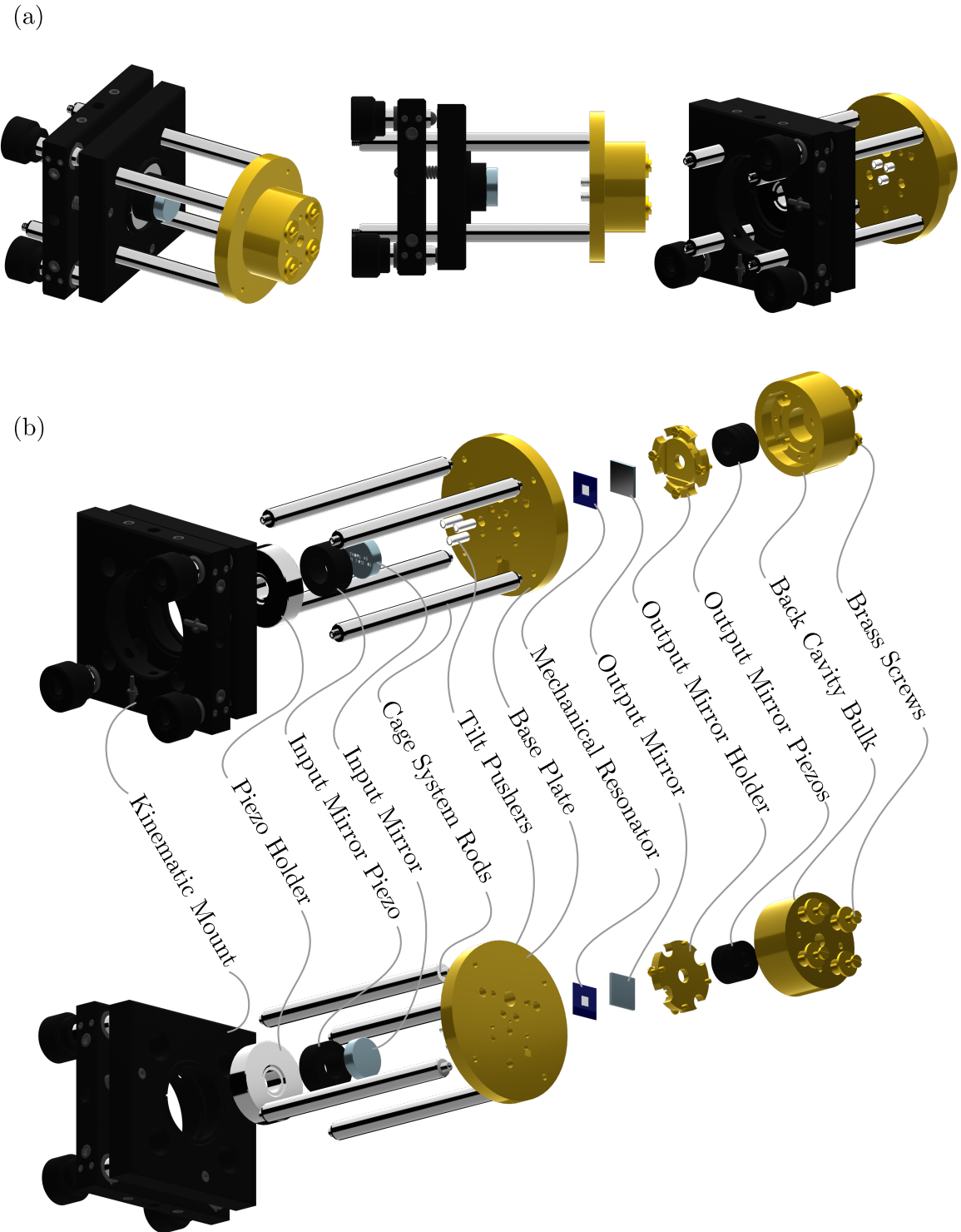


Fig. IV.3 Cavity design and assembly. (a) The figure shows the overall assembly of the MATE system from various views, highlighting the integration of the high-finesse mirrors, the membrane resonator embedded inside the back cavity copper assembly held to the input mirror Thorlabs holder through a cage system.(b) The exploded view details the arrangement of the mechanical and optical components, illustrating the modular design that facilitates alignment, stability, and compatibility with vacuum environments.

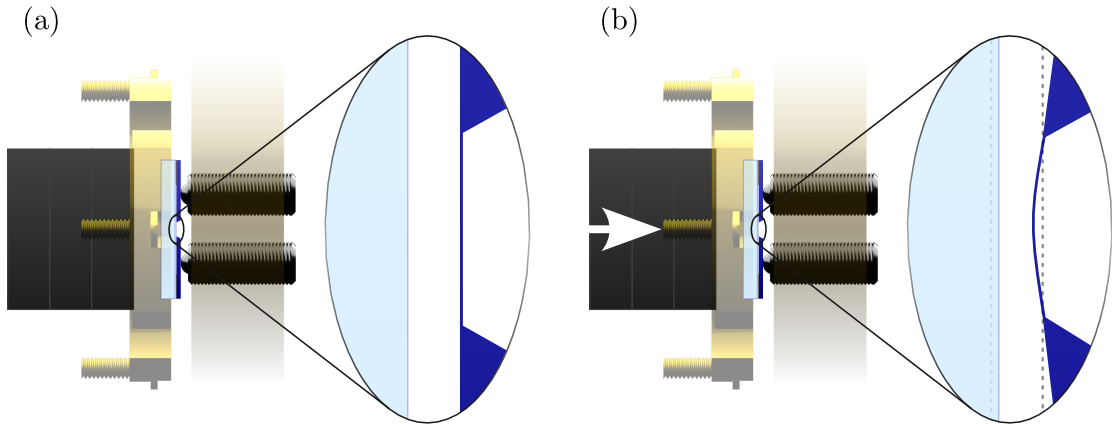


Fig. IV.4 Cavity design and assembly. (a) In this configuration (no voltage applied to the piezos), the screws are used to align the membrane plane with respect to the back mirror plane, ensuring a good parallelism between both planes. (b) Flexure tuning of the membrane position. When a voltage is applied to the piezos, they push on the back of the assembly, forcing the silicon frame to bend, thus displacing the membrane with respect to the back mirror. The two dashed lines show the initial positions of the back mirror and the membrane. This push shortens the overall cavity length (i.e. increasing the overall system's frequency), as well as the relative distance between the mirror and the membrane (i.e. changing the optomechanical coupling).

IV.1.4 Experimental Setup

The assembly is now to be integrated into the optical setup shown in Fig. IV.5. The source laser is a 1064nm Nd:YAG laser (Coherent Mephisto). We did not require the full optical power delivered by the laser, so a short optical path not detailed here splits the laser in 3 arms to eventually fiber couple some laser power and bring it to other experiments that would need 1064nm laser light.

The optical path then consists of :

- a first half waveplate and a beam splitter to adjust the total power injected into the experimental setup,
- a fibered electro-optics phase modulator (EOM Photline NIR-MPX-LN-10) to generate sidebands for the PDH locking of the cavity. It is polarization matched by using a fibered polarization controller to avoid Residual Amplitude Modulation noise (RAM) at the output (three blue circles on the optical layout).

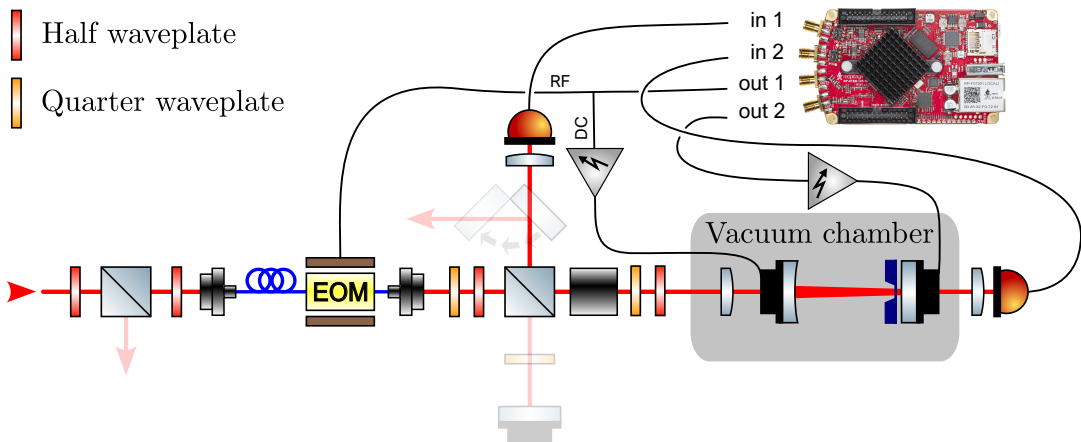


Fig. IV.5

- a fiber coupler to go from a guided optical mode to a free space optical mode, with the coupler adjusted such that the outputted beam is collimated and has a waist of about 1mm,
- a quarter waveplate to compensate for ellipticity of the output beam polarization, then a half waveplate and a beam splitter to adjust the powers injected into the cavity path and the prospective LO path, respectively,
- on the cavity path, a faraday rotator to ensure the cavity reflected beam to be deflected to an output port and not back into the fiber
- a lens to mode match the laser input mode to the cavity mode, with a focal length of 40 to 60mm depending on the input mirror radii of curvature. This lens is mounted on a x-y cage system translation mount, and is mounted inside the vacuum chamber that features AR coated windows to allow for optical access yet minimal parasite reflections.
- the cavity itself.
- two photodiodes (Thorlabs ???) to detect the reflected beam and the transmitted beam, respectively, with 40mm focal length lenses to focus the beam onto the photodiodes.

The optical path was designed to be as modular as possible, allowing for easy replacement of the components if needed, as well as additions of optical elements. For this reason, it features two faint additional optical paths as seen on Fig. IV.5, one for a prospective LO, and another to deflect the reflected beam to a Homodyne Detection setup using a flip mirror. Polarization optics would also need to be added on the Homodyne Detection path to mix the LO and the reflected beam, but this was not done during this thesis.

IV.1.5 Alignment Procedures

The optical setup is now to be aligned as to ensure a good mode matching between the laser input mode and the cavity mode. The steps are as follows, and the associated diagrams are shown in Fig. IV.6:

- **Step 1** (Fig. IV.6(a)): we position an iris diaphragm before our two injection mirrors mounted on (θ_x, θ_y) kinematic mounts. We then adjust the tilt of both mirrors i.e. *beam-walking*, such that the reflected beam is centered on the iris diaphragm: this is done by maximising the reflected signal on the reflection photodiode. This ensures the beam reflected by the output mirror (HR mirror) is at normal incidence. In a second time we tune the plane of the resonator using the three screws of the assembly. We monitor the Fizeau fringes in transmission with a camera (Allied Vision Alvium), and adjust the tilt such that no fringes are to be seen.
- **Step 2** (Fig. IV.6(b)): we then place the focusing lens in the optical path, and adjust its position such that we recover maximal power on the reflection photodiode. This lens is mounted on the (x-y) cage system translation mount, and positioned at a distance from the back mirror fixed by the cavity mode matching requirements (ref chap theory). The lens is then fixed in place using the cage system screws.
- **Step 3** (Fig. IV.6(c)): we add the input mirror on a (θ_x, θ_y) cage system mount, and adjust its position to get an input beam normal to the tangent of the concave mirror curvature. This is also done maximising the reflected power on the reflection photodiode. The mount (and thus the mirror) was also positioned at the appropriate distance from the back mirror to ensure optimal mode matching.
- **Step 4** (Fig. IV.6(d)): We scan the cavity length using the piezo actuator mounted on the input mirror, and monitor the cavity resonances using both the reflected and transmitted photodiodes. We finally fine tune the mode match by *beam-walking* the two injection mirrors. We can also play with the collimating lens at the fiber coupler (not shown on the diagram) as to fine tune for longitudinal mode matching. The cavity is now aligned and ready for operation.

IV.2 Experimental Characterization

IV.2.1 Cavity Scans

Once the cavity is aligned, we can scan the cavity length by driving the front mirror piezo with a triangular or a sine wave voltage. This signal is first amplified using a high voltage amplifier made by the LKB electronic workshop, which can deliver up to 1000V. The output

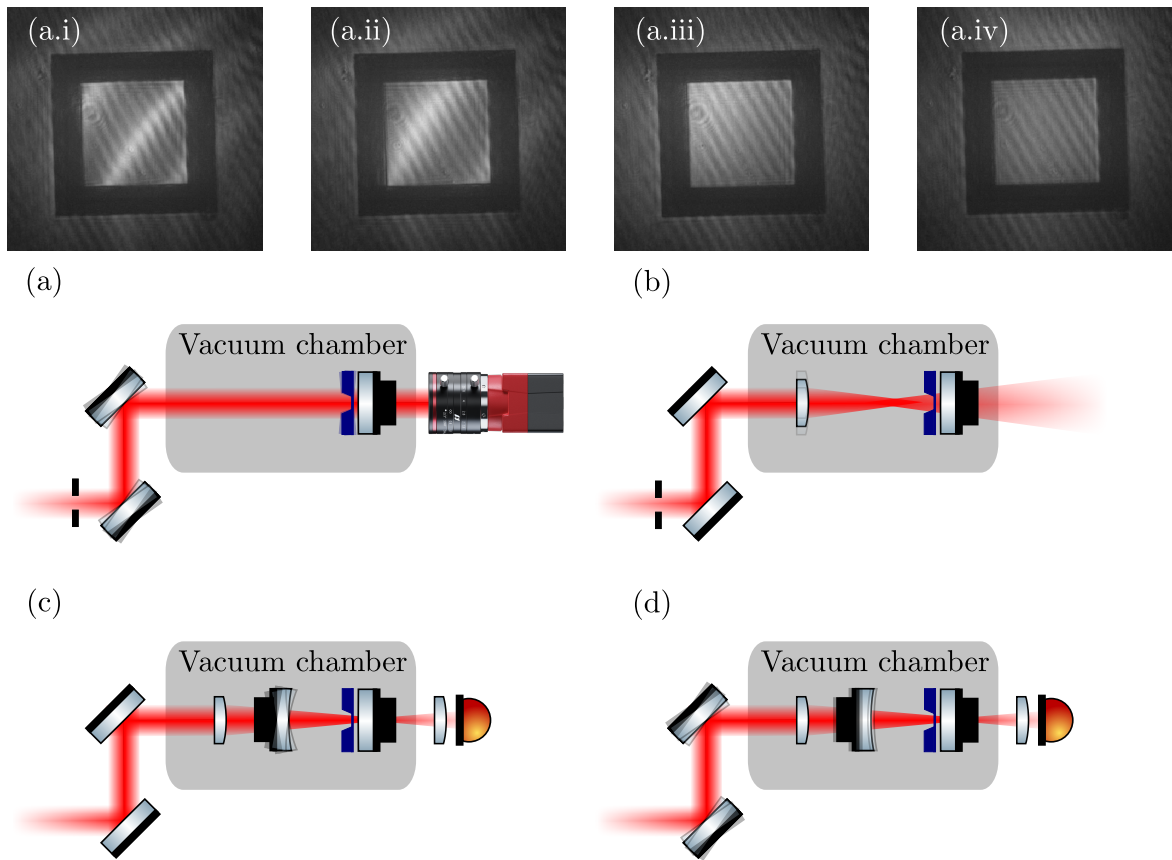


Fig. IV.6 Set up alignment procedure. (a) to (d) show the steps to align the cavity with respect to the optical path (detailed in the main text). The (a.i) to (a.iv) show what is seen on the camera for four different tilt positions where (a.iv) displays a 'good' tilt alignment: no visible fringes except for the dim fringes of the camera setup. These dim fringes are present when the beam is a normal incidence with the back mirror (use of the iris) and are believed to be interferences arising from reflections inside the camera objective as they are seen whatever the plane of focus is.

	Cavity I	Cavity II
Input mirror RoC (mm)	-25	
Back mirror RoC (mm)	∞	
Nominal input mirror T_1 (ppm)	100	
Nominal back mirror T_2 (ppm)	20	
Length L (mm)	17	24
FSR (GHz)	8.817	6.246

Table IV.2: Summary of relevant parameters for the two cavities used in this work.

impedance of the amplifier is a standard 50 Ohms, but the piezo in parallel at the end of the line with capacitance of about 15 nF low pass filters the signal at ~ 200 Hz. We can also modulated the back piezo actuators, in DC or AC, and a similar lowpass filtering occurs with a lower cutoff frequency ~ 50 Hz (3 piezo actuators in parallel with a capacitance of around 100 nF each).

We then monitor the cavity resonances using both the reflected and transmitted photodiodes and scanning the cavity over a large range, as to mode match the cavity to the TEM₀₀ mode. By beam walking, we optimally mode match the cavity such that higher order modes vanish in the photodiode noise floor and the reflected and transmitted signals are maximised, we can then perform finer scans to characterize the cavity parameters. We observed that putting the cavity under vacuum did sometimes misalign the cavity, such that even mode matching to our best ability using two mirrors outside the vacuum tank did not yield a perfect TEM₀₀ match. We also saw some membranes/phononic crystals break throughout the pumping process, most likely due to dust or degazing of the setup.

Once aligned and mode matched, we can proceed to the cavity characterization. Over the course of my PhD, few *functional* cavities were mounted inside the vacuum tank. We chose to only present the results for two of these, as to display various physical effects observed. The key parameters of these two cavities are summarized in Table IV.2. Both were mounted using 100ppm input mirrors, with a concave radius of curvature of -25mm, and a plane back mirror with a nominal transmission of 20ppm. Cavity I used the in-house fabricated membrane of nominal thickness 100nm, while cavity II used the commercial Norcada membrane of nominal thickness 50nm. The reason why we used the 100ppm input mirror rather than the 50ppm one was to ensure that the cavity linewidth would be larger than the mechanical resonance frequency of the membrane, such that we would be in the genuine unresolved sideband regime. Had we chosen the 50ppm mirror, the cavity linewidth would have been around 85kHz, an order of magnitude below the expected fundamental mechanical resonance frequency of the membrane at 861kHz (see above). A tradeoff is to be made here, as using a higher transmission input mirror reduces the intracavity power for a given input power, thus reducing radiation pressure effects.

Cavity resonances versus membrane position

We first scan the input mirror piezo with a linear ramp V_{SW} ranging from 0 to 500V at 10-50Hz, corresponding to a displacements of around $2\mu m$ (~ 4 FSRs). The back piezo actuating the membrane position was driven by a DC voltage V_{DC} ranging from 0 to 70V, with an associated stroke of $4\mu m$ (3 piezos). Knowing the FSR of the cavity, we calibrate the piezo displacement as a function of the applied voltage, and fit the resonances positions

using the theoretical model detailed in chapter 3. We modelled the front cavity length L_1 as well as the back cavity length L_2 as third order polynomials of the applied voltages V_{SW} and V_{DC} such that

$$\begin{aligned} L_1 &= a_0 + a_1 V_{SW} + a_2 V_{SW}^2 + a_3 V_{SW}^3 - \alpha V_{DC} \\ L_2 &= b_0 + b_1 V_{DC} + b_2 V_{DC}^2 + b_3 V_{DC}^3 \end{aligned} \quad (\text{IV.2})$$

where we introduced the coefficients a_i and b_i to be fitted, as well as a cross-coupling term αV_{DC} to take into account the fact that the back piezo actuators does change the front cavity length since the piezo pushing the back cavity assembly bends the silicon frame.

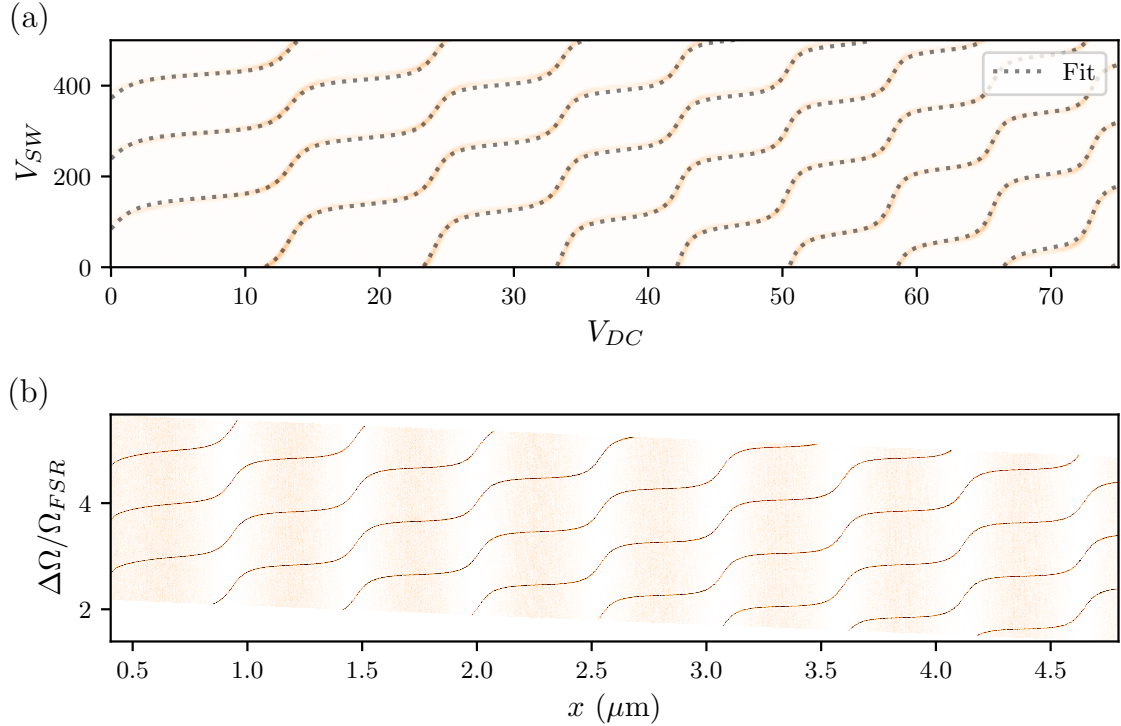


Fig. IV.7 Scans of cavity I over few FSRs. (a) Raw scan of the cavity transmission as a function of the applied voltage V_{SW} on the front piezo and V_{DC} on the back piezo. The dashed line displays the theoretical model using the fitted membrane reflectivity $|r_m|$. (b) Rescaled scan where the fitted polynomials are used to convert the sweep voltage into effective cavity detuning in FSR unit, and the DC voltage into effective membrane displacement in microns.

We show a typical raw scan in Fig. IV.7(a), as well as a rescaled one in Fig. IV.7(b), where we can see a good agreement between the experimental data and the theoretical model. This fits allow us to extract the membrane reflectivity $|r_m|$, from which we can compute the

power reflectivity and transmittivity of the membrane. This would tend towards using the single mode model as to describe radiation pressure in such a system.

Using (II.24) we can then estimate the membrane thickness to a surprisingly high accuracy with an error of less than 1nm. For cavity I, we found a thickness of $d = 86.9$ nm, while for cavity II we found $d = 41.1$ nm nm. For cavity I, the discrepancy with the nominal thickness of 100nm could be explained by the fabrication process used to make the membrane, i.e. the HF cleaning step at the end of the fabrication procedure etches the SiN layer at a rate of around 1nm/s. The membrane was cleaned for around 5 minute, such that we expected a thickness of around 90nm (it etches both sides of the membrane). For cavity II, the nominal thickness was 50nm, such that the discrepancy could be explained by fabrication tolerances.

From the fitted polynomials, we then extract the transfer functions of both piezo actuators, such that each measured observable can be mapped to an effective membrane displacement x rather than the applied voltages V_{SW} and V_{DC} . This gives us a displacement map shown in Fig. IV.8, where we can extract the cavity length variations $\Delta L = \Delta L_1(V_{\text{SW}}, V_{\text{DC}}) + \Delta L_2(V_{\text{DC}})$.

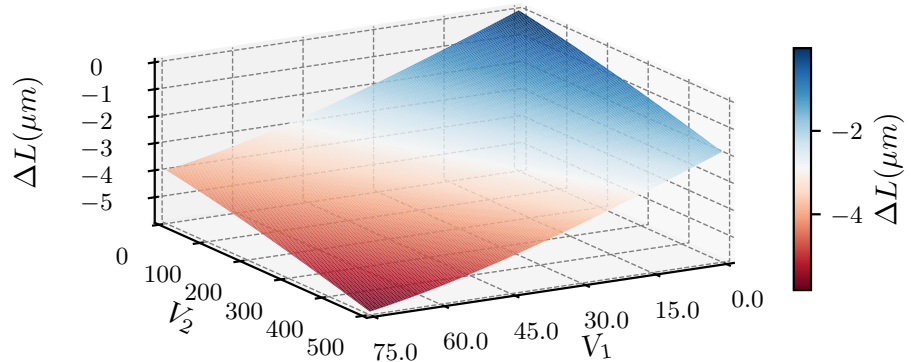


Fig. IV.8 Displacement map of cavity I. Using the fitted polynomials, we can convert the applied voltages V_{SW} and V_{DC} into effective displacements of the membrane with respect to the back mirror. The colormap shows the total cavity length variations $\Delta L = \Delta L_1 + \Delta L_2$ as a function of both piezo voltages.

Importantly, we see that, contrary to the model developed earlier, the back piezo actuation does change the front cavity length, with a non zero coupling coefficient α . This is expected from the flexure tuning mechanism, where pushing on the back of the assembly bends the silicon frame, thus shortening the overall cavity length. Knowing these ΔL_s variations, a natural next step would be to compensate the action of the back piezo on the long cavity length by adding a DC component to the front piezo voltage, such that the overall cavity length remains constant when tuning the membrane position. This would allow for a better decoupling of the membrane position and the cavity length, which would be useful for various experiments.

Slow and Fast Scans

As developed in I, scanning over a cavity resonance can be done in two different regimes, depending on the sweep rate of the cavity length with respect to the cavity linewidth. In the adiabatic limit where the sweep rate is much smaller than the cavity linewidth, the intra-cavity field adiabatically follows the input field, and the transmitted and reflected intensities follow lorentzian lineshapes. In the opposite limit where the sweep rate is much larger than the cavity linewidth, dynamical effects such as cavity ringdowns appear, where the intra-cavity field undergoes damped oscillations as the cavity length is swept over the resonance. This effect is visible both in transmission and reflection, as shown in Fig. IV.9. This effect can be used to extract the cavity linewidth/finesse by comparing the heights of the first two rebounds in transmission to their temporal spacings, as detailed in chapter I. We will come back to this point later, particularly regarding the accuracy of the finesse estimation.

To recover the lorentzian lineshapes, we first proceeded to apply slower sweep rates at the mHz level. This rendered the cavity sensitive to acoustic noise from the environment (the turbo pump for example), which did not yield quality lorentzian dips. We therefore kept the sweep rates at the 10-50Hz level, but drastically reduced the sweep amplitude to scan over a single resonance only. The classical EOM phase modulation sidebands is then used as a frequency reference to extract the cavity linewidth, as shown in Fig. IV.10 with a modulation frequency of 10 MHz. Having access to both transmitted and reflected intensities, and calibrating properly the photodiode response, we then have access to the η_T and η_R outcoupling coefficients defined in chapter 3.

Finesse

We now turn to the evaluation of the system's finesse as a function of the membrane displacement. We use two different methods to evaluate the finesse of the cavity and we compare them:

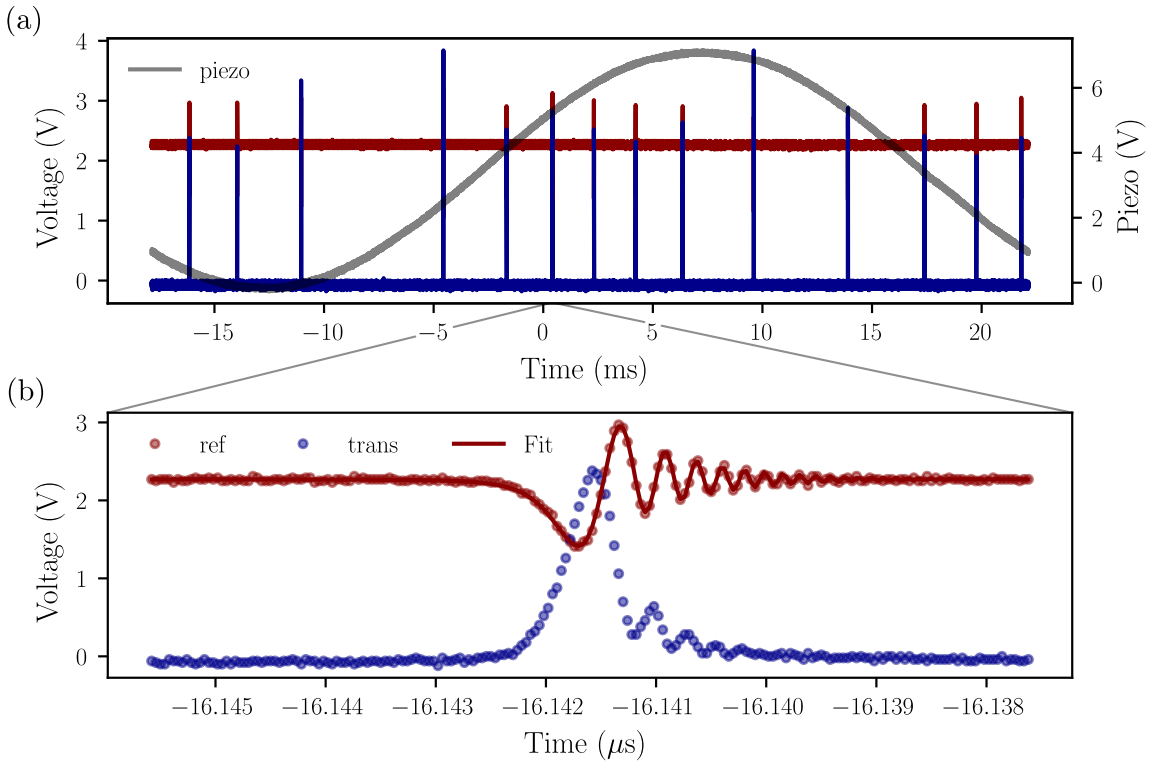


Fig. IV.9 Larges cavity scans of cavity II showing dynamical effects such as cavity ringdowns both in transmission and reflection. The sweep rate is much larger than the cavity linewidth, such that the intracavity field cannot adiabatically follow the input field. (a) Cavity transmission and reflection swept over few FSRs. The blue curve (transmission) is eventually a single column of the 2D color plots showing the cavity scan in Fig. IV.7(a). One can then actuate the back piezo to scan the membrane position as to see the cavity resonances shift. (b) Zoom on a single resonance showing cavity ringdown effects, with the fits used to compute the cavity linewidth and finesse.

- The first method would be to scan the cavity over a single resonance, and use the EOM sidebands as a frequency reference to extract the linewidth of the resonance. This method is less sensitive to piezo nonlinearities, assuming the piezo sweep is quasi linear over the resonance width.
- The second method would be to scan the cavity rapidly and observe a cavity ringdown, and compare the heights of the first two rebounds in transmission to their temporal spacings. This method is less sensitive to piezo nonlinearities, but requires a fast photodiode. Additionally we can vary the piezo sweep frequency to scan for various sweep rates and use a sine wave to sweep the cavity length such that the sweep rate is maximum at the sine zero crossing.

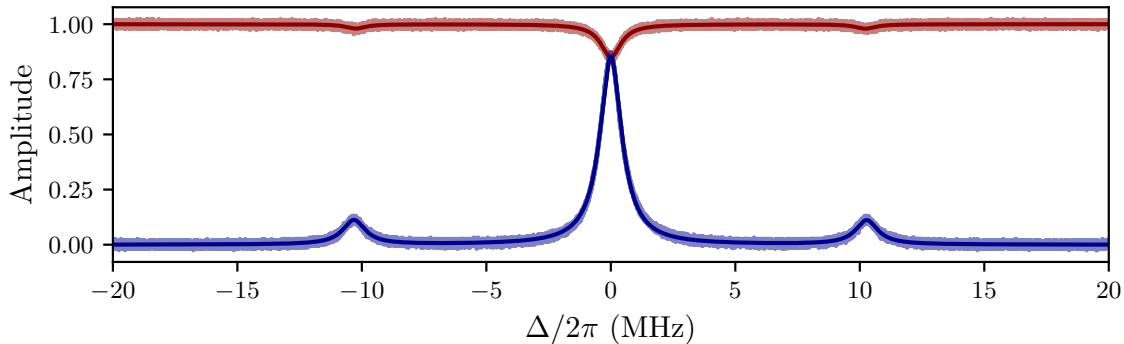


Fig. IV.10 Small amplitude scan of cavity II over a single resonance (with membrane mounted), showing the transmitted and reflected intensities as well as the EOM sidebands used as a frequency reference to extract the cavity linewidth. The modulation frequency is set to 10 MHz. The fits (solid lines) are used to extract the cavity linewidth and finesse.

We then evaluate the finesse of the empty cavity as well as the cavity with the membrane inserted, at various membrane positions. This allow for an evaluation of the losses introduced by the membrane insertion, as well as their position dependence i.e. position dependent linewidths/finesse. Assuming low scattering losses and absorption as reported in the literature for high-stress SiN membranes[SiN_review], we can attribute these excess losses to imperfect membrane alignment, i.e. remaining tilt between the membrane plane and the back mirror plane, imperfect mode matching to the cavity mode, and clipping loss due to the finite size of the membrane. The latter is not thought to be significant given the large size of the membrane with respect to the cavity mode waist, but could still contribute to few percents of the total losses.

The second method to estimate the cavity finesse turned out to be slightly disappointing, as it didn't yield consistent and reproducible results. Furthermore, numerical integration as to fit the measured data produces divergences (due to a low number of data points), which in turn forbids a proper estimation of the finesse. The reliable method was therefore taken to be the sideband method. A typical linear regression (detailed in Chap II) is still shown as an example in Fig. IV.11, but the results shown in Fig. IV.12 are only extracted from the sideband method.

The results from the first method are shown in Fig. IV.12, where we can see a good qualitative agreement with the theoretical model developped in chapter III. While cavity I featured an empty cavity finesse of 14 000, the insertion of the membrane reduced it to values ranging from 6 000 to 10 000 depending on the membrane position. Cavity II featured

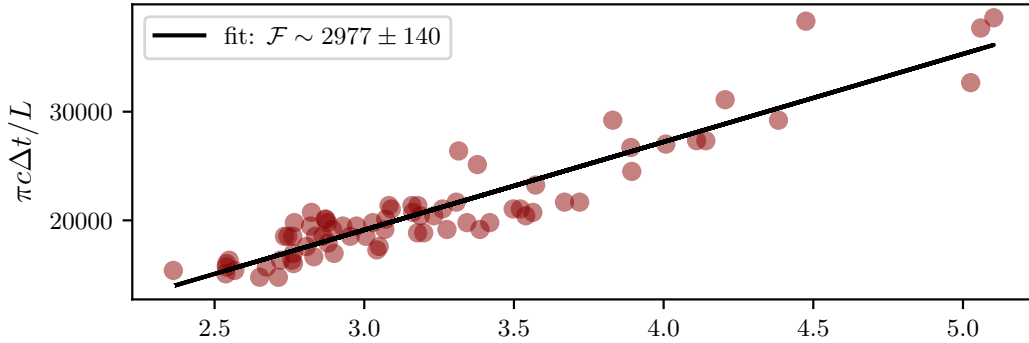


Fig. IV.11 Finesse measurement of cavity II using the ringdown method. The data points show a typical linear regression used to extract the cavity finesse from the heights of the first two rebounds in transmission as a function of their temporal spacing.

a lower empty cavity finesse of 12 780, which was further reduced to values ranging from 3 000 to 5 000 with the membrane inserted. These values are in line with other MIM/MATE systems reported in the literature[10, 9, 11], and could be improved by better membrane alignment (tilt and transverse position).

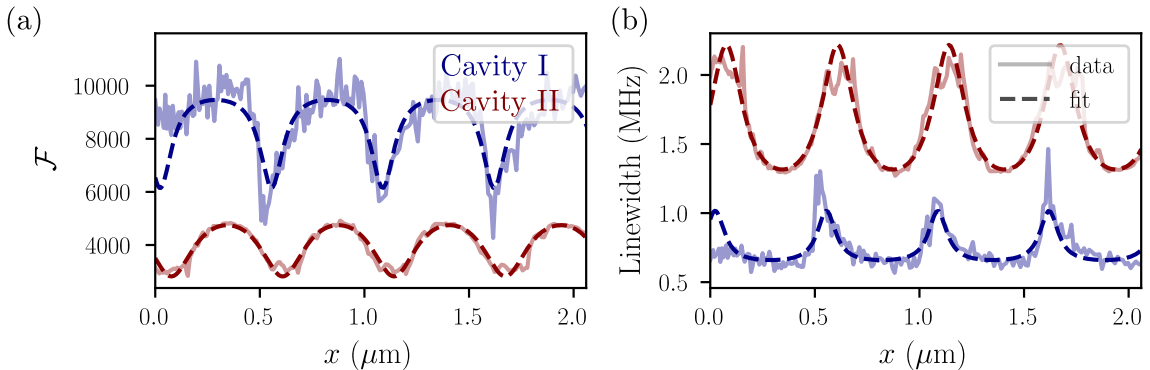


Fig. IV.12 Finesse measurement of the two cavities using the sideband method (a) and the associated linewidths (b). The finesse model in (II.35) has been changed as to account for the linear shifts underwent by all resonances as a consequence of the cavity shortening.

Cavity outcouplings

Monitoring the cavity transmission while scanning over resonances with the input piezo allows us to extract the transmission and reflections dips of the cavity at a given position (calibrated using the scans). We then fit these position dependent outcoupling transmittiv-

ties using the model developped in chapter III. The resulting scans for both cavities are shown in Fig ...

Interestingly, the second cavity displayed anomalous dips, seen as abrupt changes in the transmittivities. These have been reported years ago in Jack Harris lab [ref], and occur when two optical modes become degenerate at a given membrane position. This was verified experimentally, as the mode matching was de facto less qualitative in the second cavity than in the first one.

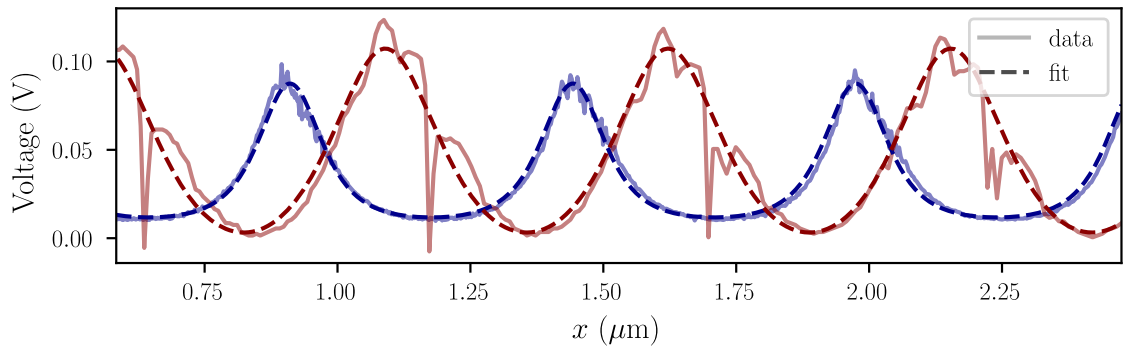


Fig. IV.13 Transmission outcoupling coefficients η_T extracted from the fits of the cavity resonances for both cavities I and II as a function of the membrane position.

Dispersive couplings

The next essential parameters central to MATE systems are the linear and quadratic dispersive couplings, as developped in chapter II. These are computed from the rescaled scans of the cavity resonances, giving access to the first and second derivative of the peak positions (once rescaled, expressed in FSR units) with respect to the membrane position. These are plotted in Fig IV.14, and we see that, although the second cavity featured a lower finesse, it does display a larger linear dispersive coupling. Due to the different cavity geometry/constraints. These were observed to vary greatly from one cavity to another, independently of the cavity finesse.

From these various characterization sequences, we extract the key parameters of the two cavities, summarized in Table IV.3.

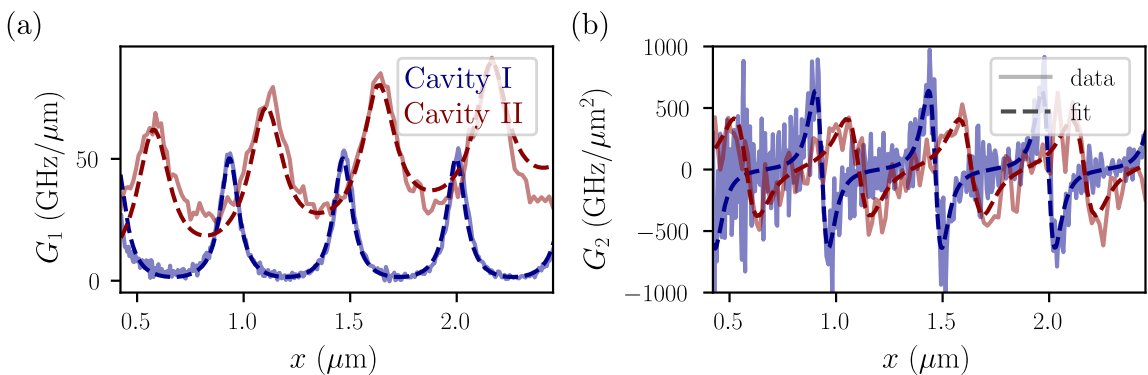
IV.2.2 Cavity Locking and Mechanical Characterization

One the cavity was characterized, we proceeded to lock it using the PDH technique detailed in chapter III. The whole lock was done using PyRPL, as to showcase its versatility and ease

	Cavity I	Cavity II
Empty cavity		
FSR (GHz)	8.817	6.246
Finesse \mathcal{F}	14 000	12 780
Linewidth (kHz)	630	489
Round-trip loss $T_1 + T_2 + \mathcal{L}$ (ppm)	449	492
Resonant reflection R(0)	0.76	0.85
T_1 (ppm)	396	455
$T_2 + \mathcal{L}$ (ppm)	53	37
MATE cavity		
Fitted reflectivity $ r_m $	0.54	0.33
Finesse \mathcal{F}	6 000 - 10 000	3 000 - 5 000
Linewidth (MHz)	0.88 - 2.20	1.25 - 2.10
Round-trip loss $T_1 + T_2 + \mathcal{L}_{\text{mem}}$ (ppm)	630 - 1570	1255 - 2095
Input power	$10\mu\text{W}$ - 50 mW	$10\mu\text{W}$ - 50 mW

Table IV.3: Summary of the measured parameters for the two cavities used in this work.

of use. The analogic signal was manipulated with standard MiniCircuits® RF components, as to amplify/filter/mix the signals as needed. The overall locking sequence is shown in Fig. IV.15, where we can see the various steps needed to lock the cavity. First, performing a fine scan over a cavity resonance as to recover a lorentzian lineshape. From this, we tune the error signal amplitude and demodulation phase as to optimize the PDH error signal. We then engage the lock by first locking on the side of the resonance dip. It was observed that at mW powers, locking on the blue side of the resonance was difficult. This could be explained by optomechanical heating of the membrane, as changing the side of the lock to

Fig. IV.14 *Linear and quadratic dispersive couplings extracted from the rescaled scans of cavity I and II. Units are given in $\text{GHz}/\mu\text{m}$ for G_1 and in $\text{GHz}/\mu\text{m}^2$ for G_2 , as rescaling by the zero point fluctuation in a cavity with a large number of photons obscures the true meaning of the vacuum optomechanical couplings.*

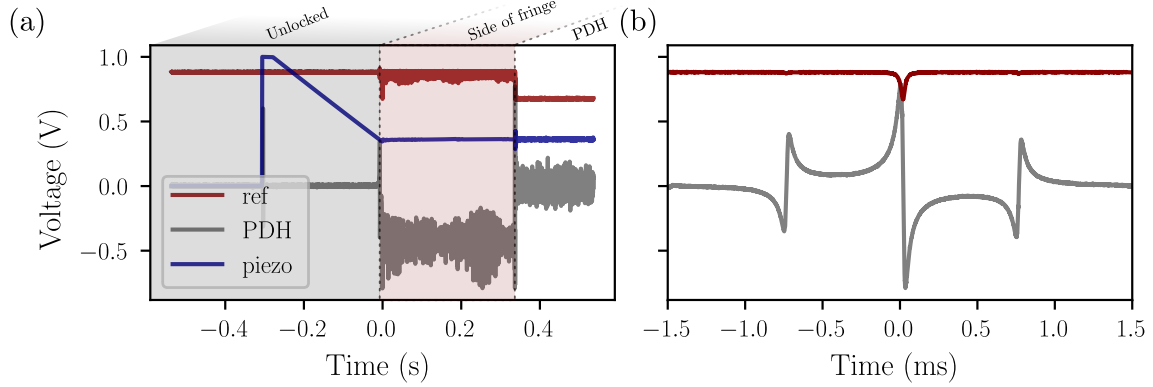


Fig. IV.15 *Lock sequence of the MATE cavity using the PDH technique. (a) Steps of the lock sequence, where we launch the side of fringe lock at approximately -0.3s. The red pitaya then sets its output voltage to 1 and starts PID control as to lock on the 0 of the error signal, which is achieved at time 0s. Being locked at a HWHM from resonance, launching the PDH lock then brings the cavity to resonance at time ~ 0.35 s. (b) Zoom on the error signal and reflected intensity during the lock sequence upon prior cavity scan. These traces are used to fine tune the error signal amplitude and demodulation phase as to optimize the PDH error signal.*

the red side made the lock more stable. Finally, we engage the PDH lock to lock onto the cavity resonance. The lock was found to be fairly robust, and could stay locked for hours without any intervention. The critical point in maintaining the lock was the input power i.e. the cavity circulating power. In terms of power range, locking at 1-50 μ W held the lock, while ramping the input power to 1-50 mW perturbed greatly the optomechanical system. We suspect that optomechanical heating, bistability and photothermal effects were playing a significant role in the lock stability.

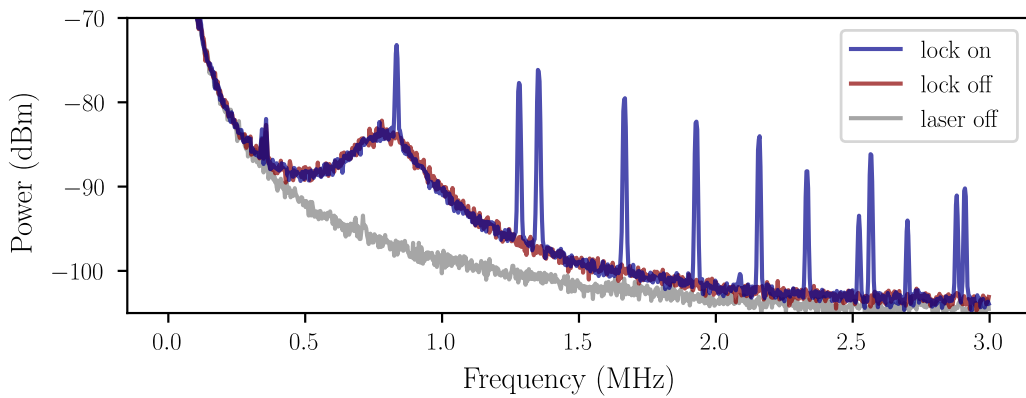


Fig. IV.16

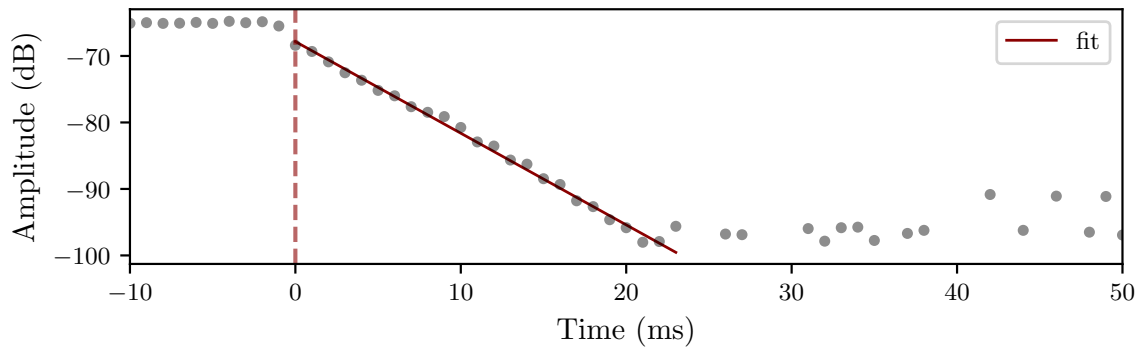


Fig. IV.17

IV.2.3 Bistability

IV.3 Design of an Optomechanical Fibered Cavity

IV.3.1 Design considerations

Chapter V

Experiments: Squeezed Light

This chapter will cover the experimental methods used in the development of frequency-dependent squeezing in optomechanical systems, focusing on the generation of squeezed light, optical locking techniques, and quadrature measurement methods. The methods are designed to enhance the sensitivity of measurements in quantum optics and optomechanics.

Contents

V.1	Optical Setup Overview	112
V.2	Cavity Resonances and Locks	113
V.2.1	IRMC Cavity	113
V.2.2	SHG Cavity	114
V.2.3	OPO Cavity	116
V.3	Spectral analysis	116
V.3.1	Detection of Squeezing and Anti-squeezing	116
V.3.2	Spectral Variation with Frequency	116
V.3.3	Optimal Quadrature Conditions	116
V.4	Filter Cavity Concept	116
V.4.1	Virgo Filter Cavity	116
V.4.2	Thermal effects in bichromatic locks	116

V.1 Optical Setup Overview

We first provide a general overview of the optical setup used to generate and manipulate squeezed light. Two lasers are used in this setup, to give flexibility as to produce bright squeezing directly from the OPO (one laser only), or produce vacuum squeezing to be mixed with a bright coherent field (two lasers). Both lasers are 1064nm Nd:YAG lasers (Coherent Mephisto and Mephisto S) as in the previous chapter. The full optical layout is shown in figure ???. The experiment was designed as to easily switch between the two configurations. Throughout this chapter, we will refer to three different optical cavities common to the two configurations: the infrared mode cleaner (IRMC) cavity, the SHG cavity, and the OPO cavity. Each of these cavities is central to the generation and manipulation of squeezed light, and their characterization is detailed in the following sections.

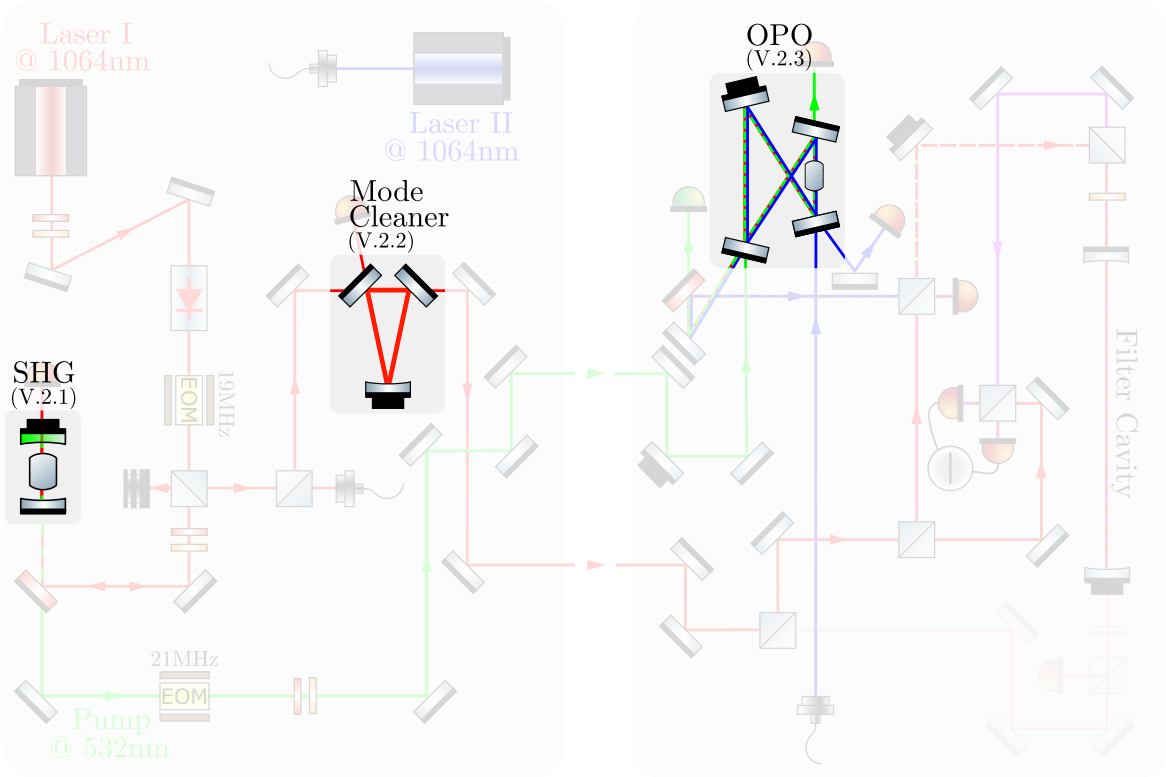


Fig. V.1

To generate bright squeezed light from an OPO, there are two configurations. The first one uses a single laser source, where the main laser beam is split into two paths. One path is directed to the SHG cavity to generate the second harmonic pump beam at 532nm, while the other path serves both for the Homodyne LO, as well as to seed the OPO with a bright field to be parametrically amplified or deamplified.

The second configuration employs two independent lasers: one dedicated to pumping

the SHG cavity and generating the 532nm pump beam, and the other serving as the LO for homodyne detection. This dual-laser setup allows for greater flexibility in controlling the relative phase and frequency between the pump and LO beams, which is crucial for optimizing squeezing measurements.

V.2 Cavity Resonances and Locks

V.2.1 IRMC Cavity

The first cavity presented here is the infrared mode cleaner (IRMC) cavity. The purpose of this cavity is to spatially filter the laser beam, ensuring a high-quality TEM00 mode profile, as well as *cleaning* the IR beam from any excess classical noise as developed in Chapter ???. It consists in a triangular cavity, with a round trip length of 99 cm, and a finesse of $\mathcal{F} = 300$. The input coupler has a transmission of 1.4%, while the other two mirrors are highly reflective. The cavity is designed to be overcoupled, with the input coupler transmission dominating the total round-trip losses. This configuration maximizes the transmission of the fundamental mode while effectively filtering out higher-order spatial modes and excess noise.

MCIR Cavity

The main reference cavity employed throughout this work is the MCIR cavity, whose relevant parameters are summarized in Table ???. It is a three mirror - *travelling wave* Fabry-Pérot resonator with a total round-trip length of $L = 84$ cm, corresponding to a free spectral range of $\text{FSR} = 357$ MHz. With a measured optical bandwidth of $\kappa/2\pi = 60$ kHz, the finesse reaches a value of $\mathcal{F} \approx 6000$, which ensures narrow resonances suitable for frequency stabilization and precision measurements. At resonance, the measured reflectivity is $R_0 \simeq 0.47$.

The cavity is formed by two mirrors of complementary characteristics. The curved end mirror has a radius of curvature RoC = −2 m, while both the input and output mirrors are plano with transmissions $T_{\text{in}} = T_{\text{out}} = 475$ ppm. Additional intracavity losses were estimated to be $P \approx 718$ ppm, as computed from Eq. (II.72), which assumes ideal mode matching of the laser to the cavity. From these values, one obtains a stable resonator with a well-defined mode geometry. The Gaussian beam waist at the cavity center is $w_0 = 578$ μm, calculated using the standard mode waist formula [ref:68].

The combination of high finesse, moderate cavity length, and relatively large mode waist makes the MCIR cavity particularly well-suited for applications requiring high spectral selectivity with minimal sensitivity to mirror surface imperfections or thermal effects. Its design parameters are optimized to balance transmission through the input and output couplers

with the unavoidable excess loss, ensuring a stable operation point for subsequent experiments.

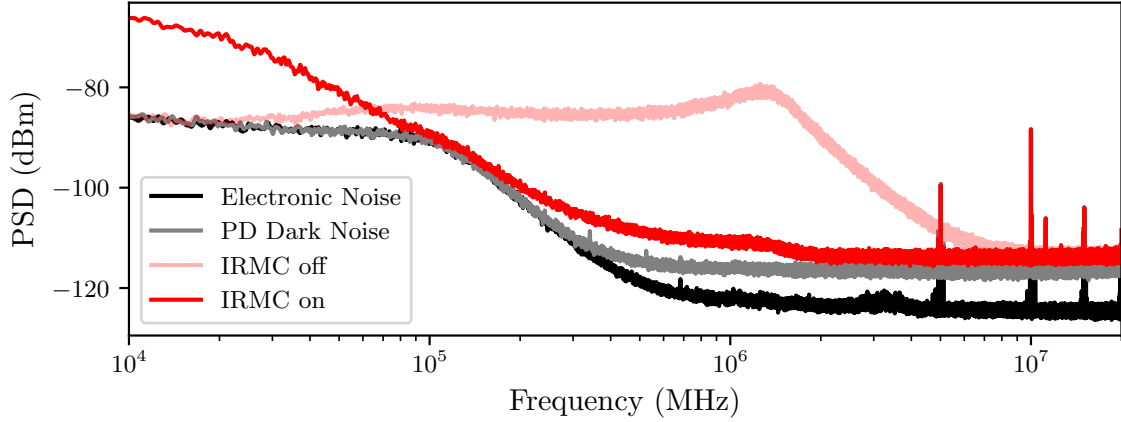


Fig. V.2

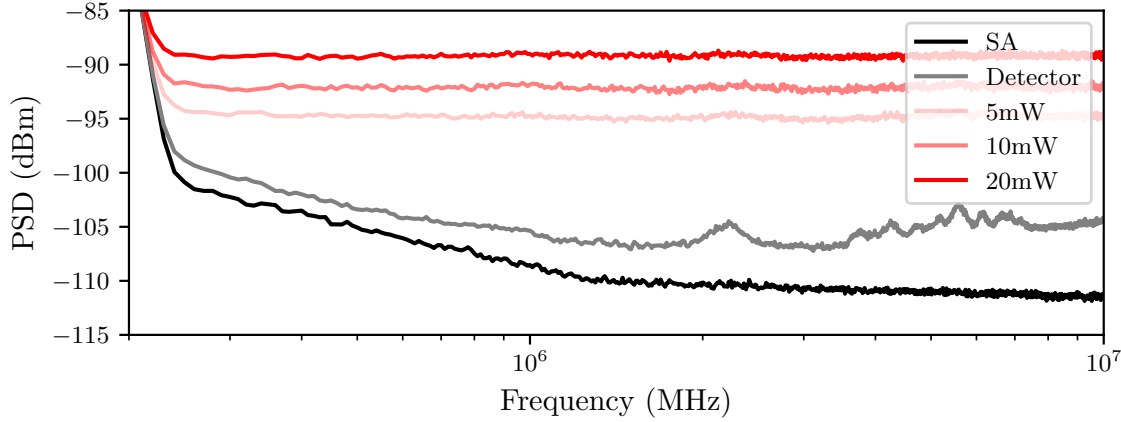


Fig. V.3

V.2.2 SHG Cavity

In order to generate a stable 532 nm pump beam for the OPO, we implemented and characterized a linear SHG cavity. The cavity is designed to resonantly enhance an incoming IR field at 1064 nm and convert it into its second harmonic through a periodically poled lithium niobate (PPLN) crystal. In what follows we detail the characterization sequence.

Cavity Scanning and Resonance Mapping. The cavity is linear, with a length of 45 mm, where both mirrors have a radius of curvature of 250 mm: $L < 2R$ so the cavity is

stable. The input coupler has a transmission of 10% at 1064 nm and less than 1% at 532 nm. The end mirror has a reflectivity of 99.9% for both 1064 nm and 532 nm. This results in a theoretical cavity finesse of approximately 60 at 1064 nm, while the finesse at 532 nm would be around 1, as no cavity buildup is desired at this wavelength. Initial characterization was performed by scanning the cavity length around resonance using a piezoelectric transducer on which the cavity output coupler was glued. The input infrared power was maintained at approximately 100 mW. The transmitted infrared signal and the generated green output were simultaneously monitored on fast photodiodes, while the PZT drive voltage was recorded to provide a calibrated frequency axis.

Typical traces of the transmitted IR beam are shown in Fig. ??(b)–(c). As the cavity length is swept, the cavity exhibits sharp IR resonance peaks, corresponding to successive TEM₀₀ modes of the cavity. At the same time, the green output rises only in coincidence with infrared resonances, confirming that efficient SHG occurs exclusively under resonant build-up of the fundamental field. The actual IR finesse was measured to be $\mathcal{F} = 35 \pm 0.6$, where the discrepancy is attributed to poor knowledge of the mirror parameters, as well as optical losses from the non linear medium. The polarization of the input beam is controlled by half and quarter waveplates as to maximize the output green power, and the symmetry of the resonance peaks in the scans further indicates negligible birefringence in the PPLN crystal.

Cavity Locking. While scanning is useful for diagnostics, stable operation of the OPO pump requires continuous locking of the cavity to resonance. To achieve this, we employed a dither lock technique. The infrared input beam was phase-modulated at $\Omega_{\text{mod}} = 19$ MHz using a free space EOM (Photline NIR-MPX-LN-10). The transmitted infrared beam is demodulated and provides an error signal suitable for feedback to the PZT actuator. The cabling of the RedPitaya and other elements are detailed in Chapter ??.

Nonlinear Crystal and Phase Matching. The nonlinear medium is a commercially available PPLN chip from Covision, with dimensions $10 \times 10 \times 1$ mm³ and five parallel poling periods. Each grating corresponds to a different quasi-phase-matching period, enabling SHG for pump wavelengths near 1064 nm across a wide temperature range. For our Nd:YAG source we selected the $\Lambda \simeq 6.9 \mu\text{m}$ grating, designed for SHG around 65°C. The crystal is AR coated at both 1064 nm and 532 nm, limiting intra-cavity facet losses.

The conversion efficiency usually follows a sinc-squared dependence on temperature. Due to the high IR power build-up in the cavity, thermal effects are observed, which distort the expected sinc² shape as reported in ... When locking the cavity, hence stabilizing intracavity power at (relatively) high IR intensity, the non-linear crystal undergoes heating due to the IR absorption. Immediately, its bulk starts to dilate, changing the quasi-phase matching

conditions.

After taking a rough quasi-phase matching curve not shown here, we identified the central peak and performed a fine scale scan of the crystal temperature at the IR input power allowing us to recover around 100mW of green power, necessary to pump the OPO below threshold. For an input IR power of around 200 mW, the generated green power as a function of temperature is shown in (a) of figure V.5, where we observed a tilt of the phase matching curve. The sinc^2 shape is however recovered when injecting an order of magnitude less IR power, but not useful to our purpose as it does not provide sufficient power for the OPO. The optimum is found at 58.37°C for the $6.90\ \mu\text{m}$ grating, with a measured phase-matching bandwidth $\Delta T \simeq 1.5^\circ\text{C}$ (FWHM).

Temperature-Induced Resonance Shifts. In addition to determining phase-matching, the crystal temperature modifies the effective optical length of the cavity. As the temperature increases, the refractive index $n(T)$ rises, effectively lengthening the cavity. When the cavity is locked, an increase in intracavity IR power induces heating of the PPLN, which shifts the resonance condition. This thermal feedback manifests as a tilt in the transmission traces during PZT sweeps at high input powers [Fig. ??(c)].

At moderate powers ($P_\omega < 200\ \text{mW}$) the effect is negligible, but at higher powers the thermo-optic shift dominates, causing a deviation from the ideal sinc^2 dependence of the conversion efficiency. Instead, the efficiency curve skews and broadens, and thermal lensing within the crystal degrades the spatial overlap of the intracavity mode. In practice, we observed that beyond $\sim 200\ \text{mW}$ of circulating IR power, the green output no longer increases linearly with P_ω , but saturates due to these thermal effects.

V.2.3 OPO Cavity

V.3 Spectral analysis

V.3.1 Detection of Squeezing and Anti-squeezing

V.3.2 Spectral Variation with Frequency

V.3.3 Optimal Quadrature Conditions

V.4 Filter Cavity Concept

V.4.1 Virgo Filter Cavity

V.4.2 Thermal effects in bichromatic locks

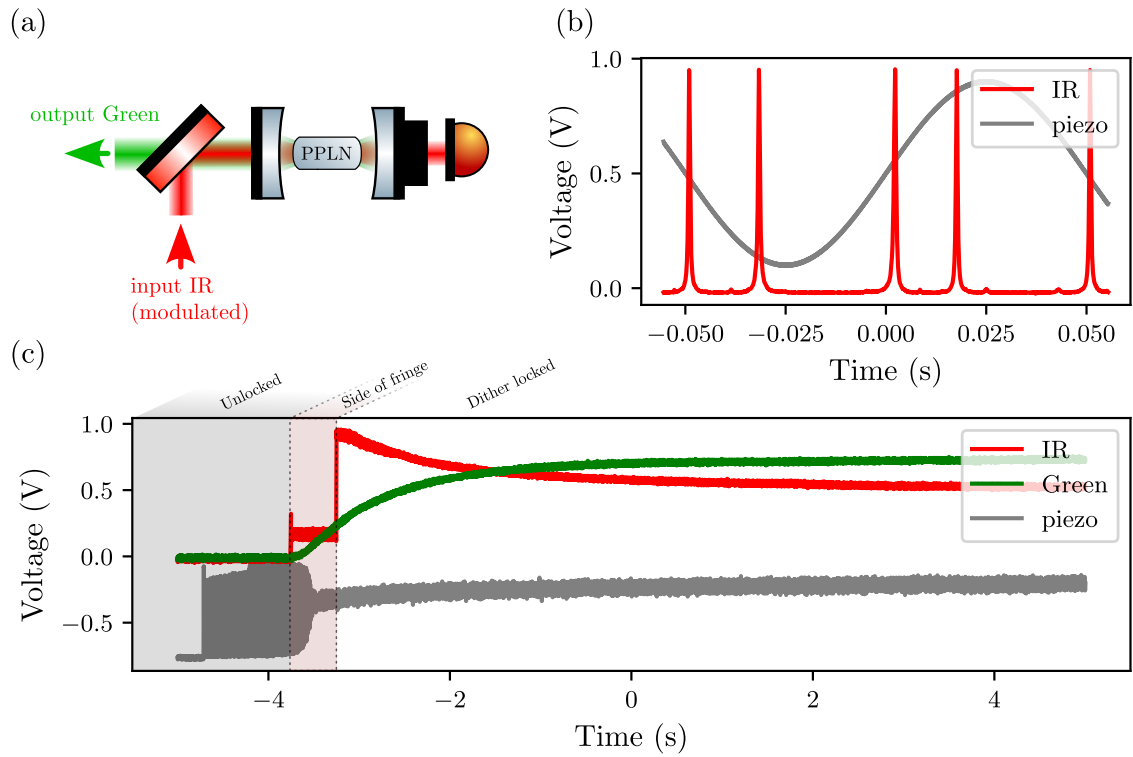


Fig. V.4

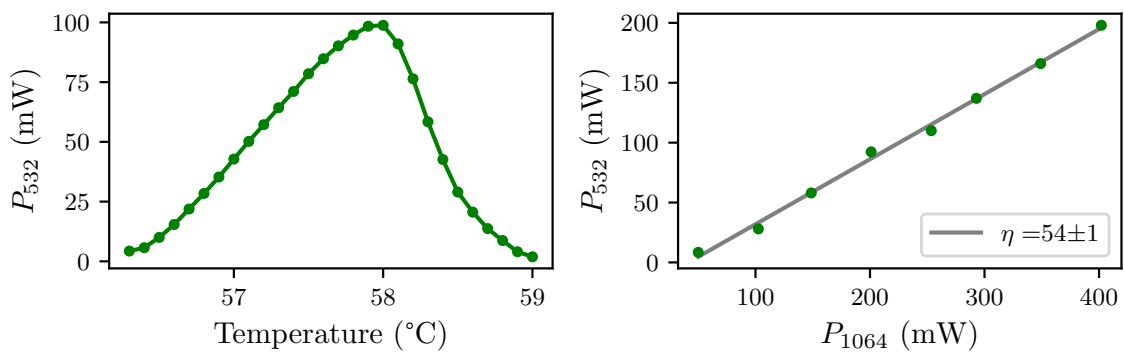


Fig. V.5

Conclusion

This chapter will cover the summary of the work done, the conclusions drawn from the experiments, and the perspectives for future research in optomechanical systems. It will highlight the key findings, their implications for quantum optics, and potential directions for further exploration.

Summary of Work

Outlooks

Final Remarks

Appendix A: Two-photon derivations

Field Quantization

From discrete to continuous modes

We consider the quantised electromagnetic field in a volume V along a single polarization direction. We assume the field to be a gaussian beam such that the quantization volume is written as $\mathcal{V} = \mathcal{A}L$, with \mathcal{A} the effective mode cross-sectional area, normal to the propagation direction z . The electric field operator can be written as

$$\hat{\mathbf{E}}(\mathbf{r}, t) = i \sum_{\ell} \sqrt{\frac{\hbar\omega_{\ell}}{2\varepsilon_0\mathcal{V}}} \left[\hat{a}_{\omega_{\ell}} \mathbf{f}_{\ell}(\mathbf{r}) e^{-i\omega_{\ell}t} - \hat{a}_{\omega_{\ell}}^{\dagger} \mathbf{f}_{\ell}^*(\mathbf{r}) e^{+i\omega_{\ell}t} \right], \quad (\text{V.1})$$

The index ℓ then labels the different modes, discrete at this point. The bosonic operators satisfy the canonical commutation relations

$$[\hat{a}_{\omega_{\ell}}, \hat{a}_{\omega_{\ell'}}^{\dagger}] = \delta_{\ell\ell'}, \quad [\hat{a}_{\omega_{\ell}}, \hat{a}_{\omega_{\ell'}}] = [\hat{a}_{\omega_{\ell}}^{\dagger}, \hat{a}_{\omega_{\ell'}}^{\dagger}] = 0.$$

We consider a the polarization along the $\hat{\mathbf{x}}$ direction where the hat denotes the unit vector and not an operator. The mode function can then be written as $\mathbf{f}_{\ell}(\mathbf{r}) = f_{\ell}(\mathbf{r})\hat{\mathbf{x}}$. We consider 1D wavevectors along the $+z$ direction i.e. positive k_{ℓ} only, such that in the limit of quantization volumes tending to infinity i.e. $L \rightarrow \infty$, the discrete sum over k modes turns into an integral over frequencies

$$\sum_{\ell}(\dots) \rightarrow \frac{L}{2\pi} \int_0^{\infty} dk(\dots) = \frac{1}{\Delta f} \int_0^{\infty} \frac{d\omega}{2\pi}(\dots) \quad \text{with} \quad \Delta f = \frac{c}{L}$$

using the dispersion relation $\omega = c|k|$. We then simply relabel $\hat{a}_{\omega_\ell} \rightarrow \hat{a}_\omega$, $f_\ell(\mathbf{r}) \rightarrow f(\mathbf{r}, \omega)$ and plug back into the original expression to have

$$\hat{\mathbf{E}}(\mathbf{r}, t) = i \int_0^\infty \frac{d\omega}{2\pi} \sqrt{\frac{\hbar\omega}{2\varepsilon_0\mathcal{A}c}} \left[\lim_{L \rightarrow \infty} \frac{\hat{a}[\Omega]}{\sqrt{\Delta f}} f(\mathbf{r}, \omega) e^{-i\omega t} - \lim_{L \rightarrow \infty} \frac{\hat{a}^\dagger[\Omega]}{\sqrt{\Delta f}} f^*(\mathbf{r}, \omega) e^{+i\omega t} \right] \hat{\mathbf{x}}.$$

and we can define the continuous bosonic operators as

$$\hat{a}[\omega] = \lim_{L \rightarrow \infty} \frac{\hat{a}_\omega}{\sqrt{\Delta f}} \quad \text{and} \quad \hat{a}^\dagger[\omega] = \lim_{L \rightarrow \infty} \frac{\hat{a}_\omega^\dagger}{\sqrt{\Delta f}}$$

such that the electric field operator reads

$$\hat{\mathbf{E}}(\mathbf{r}, t) = i \int_0^\infty \frac{d\omega}{2\pi} \mathcal{E} \left[\hat{a}[\omega] f(\mathbf{r}, \omega) e^{-i\omega t} - \hat{a}^\dagger[\omega] f^*(\mathbf{r}, \omega) e^{+i\omega t} \right] \hat{\mathbf{x}}, \quad \text{with} \quad \mathcal{E} = \sqrt{\frac{\hbar\omega}{2\varepsilon_0\mathcal{A}c}}.$$

Commutation relations

Using standard complex analysis techniques, the kronecker delta can be expressed as

$$\delta_{\ell\ell'} = \int_{-\pi}^{+\pi} dt \frac{e^{i(\ell-\ell')t}}{2\pi}.$$

Upon the aforementioned assumptions, we can introduce the frequency spacing $\Delta\omega = 2\pi\Delta f$ such that the discrete angular frequencies are written as $\omega_\ell = \ell\Delta\omega$. It then follows that $\ell - \ell' = (\omega_\ell - \omega_{\ell'})/\Delta\omega$. By changing the variable of integration from t to $t' = t/\Delta\omega$, we can rewrite the kronecker delta as

$$\delta_{\ell\ell'} = \int_{-L/2c}^{+L/2c} dt' \Delta f e^{i(\omega_\ell - \omega_{\ell'})t'}.$$

We can then see that in the limit of $L \rightarrow \infty$ i.e. $\Delta\omega \rightarrow 0$, the integral limits tend to infinity and the kronecker delta turns into a dirac delta such that

$$\lim_{L \rightarrow \infty} \frac{\delta_{\ell\ell'}}{\Delta f} = \int_{-\infty}^{+\infty} dt' e^{i(\omega - \omega')t'} = 2\pi\delta(\omega - \omega').$$

where we relabeled $\omega_\ell \rightarrow \omega$ and $\omega_{\ell'} \rightarrow \omega'$. The commutation relations for the continuous bosonic operators then read which satisfy the commutation relations

$$[\hat{a}[\omega], \hat{a}^\dagger[\omega']] = \lim_{L \rightarrow \infty} \frac{[\hat{a}_{\omega_\ell}, \hat{a}_{\omega_{\ell'}}^\dagger]}{\Delta f} = 2\pi\delta(\omega - \omega'), \quad [\hat{a}[\omega], \hat{a}[\omega']] = [\hat{a}^\dagger[\omega], \hat{a}^\dagger[\omega']] = 0.$$

Two photon formalism

Quadratures

We will now consider mode field frequencies $\omega = \omega_0 + \Omega$ around a carrier frequency ω_0 , such that the integral term becomes

$$\int_0^\infty \frac{d\omega}{2\pi}(\dots) \rightarrow \int_{-\omega_0}^\infty \frac{d\Omega}{2\pi}(\dots) \sim \int_{-B}^B \frac{d\Omega}{2\pi}(\dots) \sim \int_{-\infty}^\infty \frac{d\Omega}{2\pi}(\dots)$$

where B is the detection bandwidth, which is always much smaller than the optical frequency ω_0 . We can then safely extend the integral limits to infinity. Assuming that the mode function $f(\mathbf{r}, \omega)$ does not vary significantly over the bandwidth B , we can approximate it by its value at the carrier frequency $f(\mathbf{r}, \omega_0) \equiv f(\mathbf{r})$. Pulling out this term from the integral, one can then project the electric field operator onto both the proper polarization axis and this mode function such that the electric field operator becomes spatially independent and reads

$$\hat{E}(t) = i\mathcal{E}_0 \int_0^\infty \frac{d\Omega}{2\pi} \left[\hat{a}_+ e^{-i(\omega_0+\Omega)t} - \hat{a}_+^\dagger e^{+i(\omega_0+\Omega)t} + \hat{a}_- e^{-i(\omega_0-\Omega)t} - \hat{a}_-^\dagger e^{+i(\omega_0-\Omega)t} \right] \quad (\text{V.2})$$

with $\mathcal{E}_0 = \sqrt{\hbar\omega/2\varepsilon_0\mathcal{A}c}$, and where we additionally split the integral term in two, introducing negative and positive sideband frequencies whose annihilation and creation operators are written as

$$\hat{a}_\pm \equiv c_\pm \hat{a}[\omega_0 \pm \Omega] \quad \text{and} \quad \hat{a}_\pm^\dagger \equiv c_\pm \hat{a}^\dagger[\omega_0 \pm \Omega] \quad \text{with} \quad c_\pm = \sqrt{\frac{\omega_0 \pm \Omega}{\omega_0}}.$$

The commutators then read

$$[\hat{a}_\pm, \hat{a}_\pm^\dagger] = 2\pi c_\pm^2 \delta(\Omega - \Omega'), \quad [\hat{a}_\pm, \hat{a}_\mp] = [\hat{a}_\pm^\dagger, \hat{a}_\mp^\dagger] = 0$$

$$[\hat{a}_\pm, \hat{a}_\mp^\dagger] = 2\pi c_+ c_- \delta(\Omega + \Omega'), \quad [\hat{a}_\pm, \hat{a}_\mp] = [\hat{a}_\pm^\dagger, \hat{a}_\mp^\dagger] = 0$$

Computing expectation values for these operators in vacuum yields $\langle \hat{a}_\pm \rangle = \langle \hat{a}_\pm^\dagger \rangle = \langle 0 | \hat{a}_\pm^\dagger \hat{a}_\pm | 0 \rangle = 0$ and $\langle 0 | \hat{a}_\pm \hat{a}_\pm^\dagger | 0 \rangle = 2\pi c_\pm^2 \delta(0)$, which is consistent with the fact that no photons are present in these modes. We then regroup the terms along common quadratures $\cos \omega_0 t$ and $\sin \omega_0 t$ such that we get

$$\begin{aligned} \hat{E}(t) = i\mathcal{E}_0 & \left[\cos \omega_0 t \int_0^\infty \frac{d\Omega}{2\pi} \left[(\hat{a}_+ - \hat{a}_-^\dagger) e^{-i\Omega t} + (\hat{a}_- - \hat{a}_+^\dagger) e^{+i\Omega t} \right] \right. \\ & \left. - i \sin \omega_0 t \int_0^\infty \frac{d\Omega}{2\pi} \left[(\hat{a}_+ + \hat{a}_-^\dagger) e^{-i\Omega t} + (\hat{a}_- + \hat{a}_+^\dagger) e^{+i\Omega t} \right] \right] \end{aligned}$$

We now define the two-photon quadrature operators as

$$\hat{p}[\Omega] = \hat{a}_+ + \hat{a}_-^\dagger, \quad \hat{q}[\Omega] = i(\hat{a}_-^\dagger - \hat{a}_+)$$

such that the electric field operator reads

$$\begin{aligned} \hat{E}(t) &= \mathcal{E}_0 \left[\cos\left(\omega_0 t - \frac{\pi}{2}\right) \int_0^\infty \frac{d\Omega}{2\pi} [\hat{p}[\Omega] e^{-i\Omega t} + \hat{p}^\dagger[\Omega] e^{+i\Omega t}] \right. \\ &\quad \left. + \sin\left(\omega_0 t - \frac{\pi}{2}\right) \int_0^\infty \frac{d\Omega}{2\pi} [\hat{q}[\Omega] e^{-i\Omega t} + \hat{q}^\dagger[\Omega] e^{+i\Omega t}] \right] \end{aligned} \quad (\text{V.3})$$

where we used the fact that $\hat{p}^\dagger[\Omega] = \hat{p}[-\Omega]$ and $\hat{q}^\dagger[\Omega] = \hat{q}[-\Omega]$. The $\pi/2$ phase shifts originate from the leading factor i in the electric-field operator. Had the field operator been written without that prefactor (and without the minus sign in the creation-term), the resulting cosine and sine components would contain no such phase offset. The commutation relations for these quadrature operators read

$$\begin{aligned} [\hat{p}[\Omega], \hat{q}^\dagger[\Omega']] &= [\hat{q}[\Omega], \hat{p}^\dagger[\Omega']] = 4\pi i \delta(\Omega - \Omega') \\ [\hat{p}[\Omega], \hat{p}^\dagger[\Omega']] &= [\hat{q}[\Omega], \hat{q}^\dagger[\Omega']] = 4\pi \frac{\Omega}{\omega_0} \delta(\Omega - \Omega') \sim 0 \quad \text{if } \Omega \ll \omega_0 \\ [\hat{p}[\Omega], \hat{q}[\Omega']] &= [\hat{p}^\dagger[\Omega], \hat{q}^\dagger[\Omega']] = 0. \end{aligned}$$

In the limit where the sideband frequencies are small compared to the carrier frequency i.e. $\Omega \ll \omega_0$, we can approximate these prefactors by $c_\pm \sim 1$.

Expectations values in vacuum

We now proceed to evaluate the first and second momenta of our field operators in the vacuum state $|0\rangle$. As expected, the annihilation and creation operators have zero mean in vacuum, such that

$$\langle 0 | \hat{a}_+ | 0 \rangle = \langle 0 | \hat{a}_-^\dagger | 0 \rangle = 0$$

so it follows that

$$\langle 0 | \hat{p}[\Omega] | 0 \rangle = \langle 0 | \hat{q}[\Omega] | 0 \rangle = 0.$$

Building the two-photon quadrature column vector as

$$\hat{\mathbf{u}}[\Omega] = \begin{pmatrix} \hat{p}[\Omega] \\ \hat{q}[\Omega] \end{pmatrix}, \quad \text{we have} \quad \langle \hat{\mathbf{u}}[\Omega] \rangle = \begin{pmatrix} 0 \\ 0 \end{pmatrix}$$

where we see that, for a vacuum state, the full operator $\hat{\mathbf{u}}[\Omega]$ actually equates the fluctuating part $\delta\hat{\mathbf{u}}[\Omega] = \hat{\mathbf{u}}[\Omega] - \langle \hat{\mathbf{u}}[\Omega] \rangle$ since the mean value is zero. In the following, we will assume

that expectation values are always computed in the vacuum state unless otherwise specified (we will omit the $|0\rangle$ notation for clarity). We only wrote the results for the \hat{a}_+ and \hat{a}_-^\dagger operators as there are the ones composing the \hat{p} and \hat{q} quadratures, but the same results hold for the other sideband operators as well. We can then compute the second momenta of the annihilation and creation operators, yielding

$$\langle 0 | \hat{a}_-^\dagger \hat{a}_- | 0 \rangle = \langle 0 | \hat{a}_+ \hat{a}_- | 0 \rangle = \langle 0 | \hat{a}_-^\dagger \hat{a}_+^\dagger | 0 \rangle = 0$$

$$\langle 0 | \hat{a}_\pm \hat{a}_\pm^\dagger | 0 \rangle = 2\pi\delta(\Omega - \Omega') .$$

Using these relations, we can compute the second momenta for the two-photon quadrature operators as

$$\begin{aligned} \langle 0 | \hat{p}[\Omega] \hat{p}^\dagger[\Omega'] | 0 \rangle &= \langle 0 | \hat{a}_+ \hat{a}_+^\dagger + \hat{a}_+ \hat{a}_- + \hat{a}_-^\dagger \hat{a}_+^\dagger + \hat{a}_-^\dagger \hat{a}_- | 0 \rangle \\ &= 2\pi\delta(\Omega - \Omega') , \\ \langle 0 | \hat{q}[\Omega] \hat{q}^\dagger[\Omega'] | 0 \rangle &= 2\pi\delta(\Omega - \Omega') . \end{aligned}$$

as well as

$$\langle 0 | \hat{p}[\Omega] \hat{q}^\dagger[\Omega'] | 0 \rangle = -\langle 0 | \hat{q}^\dagger[\Omega] \hat{p}[\Omega'] | 0 \rangle = i2\pi\delta(\Omega - \Omega') .$$

Using the expression for the symmetrized double sided covariance matrix given in the main text, we can compute the covariance matrix for the two-photon quadrature operators in vacuum as

$$\begin{aligned} \mathbf{S}[\Omega] &= \frac{1}{2} \int \frac{\delta\Omega'}{2\pi} \langle \{ \delta\hat{\mathbf{u}}[\Omega], \delta\hat{\mathbf{u}}^\dagger[\Omega'] \} \rangle \\ &= \frac{1}{2} \int \frac{\delta\Omega'}{2\pi} \begin{pmatrix} \langle \{\hat{p}[\Omega], \hat{p}^\dagger[\Omega']\} \rangle & \langle \{\hat{p}[\Omega], \hat{q}^\dagger[\Omega']\} \rangle \\ \langle \{\hat{q}[\Omega], \hat{p}^\dagger[\Omega']\} \rangle & \langle \{\hat{q}[\Omega], \hat{q}^\dagger[\Omega']\} \rangle \end{pmatrix} \\ &= \frac{1}{2} \int \frac{\delta\Omega'}{2\pi} \begin{pmatrix} 2 \cdot 2\pi\delta(\Omega - \Omega') & 0 \\ 0 & 2 \cdot 2\pi\delta(\Omega - \Omega') \end{pmatrix} \\ &= \begin{pmatrix} 1 & 0 \\ 0 & 1 \end{pmatrix} = \mathbf{1} . \end{aligned}$$

The vacuum state then features vacuum fluctuations of unity in both quadratures, across all sideband frequencies Ω , and no correlations between the quadratures.

States and Operators in the Two-Photon Formalism

In a similar fashion as in the single-mode case, we can define the displacement operator as

$$\hat{D}(\alpha) = \exp \left(\int_{-\infty}^{\infty} \frac{d\Omega}{2\pi} [\alpha(\Omega) \hat{a}_-^\dagger - \alpha^*(\Omega) \hat{a}_+] \right)$$

as well as a squeezing operator

$$\hat{S}(r, \theta) = \exp \left(r \int_{-\infty}^{\infty} \frac{d\Omega}{2\pi} [e^{-i2\theta(\Omega)} \hat{a}_+ \hat{a}_- - e^{i2\theta(\Omega)} \hat{a}_+^\dagger \hat{a}_-^\dagger] \right)$$

where r is the squeezing factor and $\theta(\Omega)$ the squeezing angle. Here we assumed the squeezing parameter to be frequency independent, but one can easily generalize to a frequency dependent squeezing parameter $r(\Omega)$. Using the sidebands annihilation operators defined previously, we can compute the action of the displacement and squeezing operators on the annihilation operator as

$$\begin{aligned} \hat{D}^\dagger(\alpha) \hat{a}_+ \hat{D}(\alpha) &= \hat{a}_+ + \alpha(\Omega), \\ \hat{S}^\dagger(r, \theta) \hat{a}_+ \hat{S}(r, \theta) &= \hat{a}_+ \cosh r - e^{i2\theta(\Omega)} \hat{a}_-^\dagger \sinh r. \end{aligned}$$

We consider a intial vacuum state $|0\rangle$, and we displace it by a coherent amplitude $\alpha(\Omega) = \alpha\delta(\Omega)$ i.e. a carrier, monochromatic field of complex amplitude α sitting at frequency 0 (we are in the frame rotating at ω_0 already since we factored out the $e^{-i\omega_0 t}$ term). The displacement operator then acts on the two photon quadrature operators as

$$\begin{aligned} \hat{D}^\dagger(\alpha) \hat{p}[\Omega] \hat{D}(\alpha) &= \hat{p}[\Omega] + 2 \operatorname{Re}\{\alpha\} \delta(\Omega), \\ \hat{D}^\dagger(\alpha) \hat{q}[\Omega] \hat{D}(\alpha) &= \hat{q}[\Omega] + 2 \operatorname{Im}\{\alpha\} \delta(\Omega). \end{aligned}$$

or in matrix form

$$\hat{D}^\dagger(\alpha) \hat{\mathbf{u}}[\Omega] \hat{D}(\alpha) = \hat{\mathbf{u}}[\Omega] + 2 \begin{pmatrix} \operatorname{Re}\{\alpha\} \\ \operatorname{Im}\{\alpha\} \end{pmatrix} \delta(\Omega).$$

In a similar fashion, the squeezing operator acts as

$$\begin{aligned} \hat{S}^\dagger(r, \theta) \hat{p}[\Omega] \hat{S}(r, \theta) &= \hat{p}[\Omega] (\cosh r - \sinh r \cos 2\theta) - \hat{q}[\Omega] \sin 2\theta \sinh r, \\ \hat{S}^\dagger(r, \theta) \hat{q}[\Omega] \hat{S}(r, \theta) &= \hat{q}[\Omega] (\cosh r + \sinh r \cos 2\theta) - \hat{p}[\Omega] \sin 2\theta \sinh r. \end{aligned}$$

and its matrix form reads

$$\hat{S}^\dagger(r, \theta) \hat{\mathbf{u}}[\Omega] \hat{S}(r, \theta) = \mathbf{S}(r, \theta) \hat{\mathbf{u}}[\Omega], \quad \text{with} \quad \mathbf{S}(r, \theta) = \begin{pmatrix} \cosh r - \sinh r \cos 2\theta & -\sin 2\theta \sinh r \\ -\sin 2\theta \sinh r & \cosh r + \sinh r \cos 2\theta \end{pmatrix}.$$

The state resulting from applying both operators onto the vacuum is written as

$$|\psi\rangle = \hat{S}(r, \theta) \hat{D}(\alpha) |0\rangle$$

and describes a squeezed coherent state, or bright squeezed state. One can then set the coherent amplitude to 0 as to get a vacuum squeezed state, or set the squeezing parameter to 0 to get a coherent state. This is one of the most generic gaussian state one can define in quantum optics. We write the operator product as $\hat{D}\hat{S}$ and we drop the Ω dependencies to lighten the notation, such that applying them to the field operators yields

$$\begin{aligned} \hat{D}^\dagger \hat{S}^\dagger \hat{a}_+ \hat{S} \hat{D} &= \hat{a}_+ \cosh r - e^{i2\theta} \hat{a}_-^\dagger \sinh r + \gamma \delta(\Omega) \\ \hat{D}^\dagger \hat{S}^\dagger \hat{a}_-^\dagger \hat{S} \hat{D} &= \hat{a}_-^\dagger \cosh r - e^{-i2\theta} \hat{a}_+ \sinh r + \gamma^* \delta(\Omega). \end{aligned}$$

as well as the quadratures

$$\begin{aligned} \hat{D}^\dagger \hat{S}^\dagger \hat{p} \hat{S} \hat{D} &= \hat{p}(\cosh r - \cos 2\theta \sinh r) - \hat{q} \sin 2\theta \sinh r + 2 \operatorname{Re}\{\gamma\} \delta(\Omega), \\ \hat{D}^\dagger \hat{S}^\dagger \hat{q} \hat{S} \hat{D} &= \hat{q}(\cosh r + \cos 2\theta \sinh r) - \hat{p} \sin 2\theta \sinh r + 2 \operatorname{Im}\{\gamma\} \delta(\Omega). \end{aligned}$$

where we introduced the scalar part of these transformed operators as

$$\begin{aligned} \gamma &= \alpha \cosh r - \alpha^* e^{i2\theta} \sinh r, \\ \gamma^* &= \alpha^* \cosh r - \alpha e^{-i2\theta} \sinh r. \end{aligned}$$

The matrix form then reads

$$\hat{D}^\dagger \hat{S}^\dagger \hat{\mathbf{u}} \hat{S} \hat{D} = \mathbf{S}(r, \theta) \hat{\mathbf{u}} + 2 \begin{pmatrix} \operatorname{Re}\{\gamma\} \\ \operatorname{Im}\{\gamma\} \end{pmatrix} \delta(\Omega).$$

The mean values is then straightforward to compute

$$\begin{aligned} \langle \hat{D}^\dagger \hat{S}^\dagger \hat{\mathbf{u}} \hat{S} \hat{D} \rangle &= \mathbf{S}(r, \theta) \langle \hat{\mathbf{u}} \rangle + 2 \begin{pmatrix} \operatorname{Re}\{\gamma\} \\ \operatorname{Im}\{\gamma\} \end{pmatrix} \delta(\Omega) \\ &= 2 \begin{pmatrix} \operatorname{Re}\{\gamma\} \\ \operatorname{Im}\{\gamma\} \end{pmatrix} \delta(\Omega). \end{aligned}$$

such that the fluctuating part reads

$$\delta \hat{\mathbf{u}} = \hat{D}^\dagger \hat{S}^\dagger \hat{\mathbf{u}} \hat{S} \hat{D} - \langle \hat{D}^\dagger \hat{S}^\dagger \hat{\mathbf{u}} \hat{S} \hat{D} \rangle = \mathbf{S}(r, \theta) \hat{\mathbf{u}} \quad \text{and} \quad \delta \hat{\mathbf{u}}^\dagger = \hat{\mathbf{u}}^\dagger \mathbf{S}(r, \theta).$$

where we used the fact that the squeezing matrix is symmetric, i.e. $\mathbf{S} = \mathbf{S}^T$. The covariance matrix for this squeezed coherent state then reads

$$\begin{aligned} \mathbf{S}[\Omega] &= \frac{1}{2} \int \frac{\delta\Omega'}{2\pi} \langle \{\delta \hat{\mathbf{u}}[\Omega], \delta \hat{\mathbf{u}}^\dagger[\Omega']\} \rangle \\ &= \frac{1}{2} \int \frac{\delta\Omega'}{2\pi} \langle \{\mathbf{S}(r, \theta) \hat{\mathbf{u}}[\Omega], \hat{\mathbf{u}}^\dagger[\Omega'] \mathbf{S}(r, \theta)\} \rangle \\ &= \mathbf{S}(r, \theta) \left(\frac{1}{2} \int \frac{\delta\Omega'}{2\pi} \langle \{\hat{\mathbf{u}}[\Omega], \hat{\mathbf{u}}^\dagger[\Omega']\} \rangle \right) \mathbf{S}(r, \theta) \\ &= \mathbf{S}(r, \theta) \cdot \mathbf{1} \cdot \mathbf{S}(r, \theta) = \mathbf{S}(r, \theta)^2 \\ &= \begin{pmatrix} \cosh 2r - \sinh 2r \cos 2\theta & -\sin 2\theta \sinh 2r \\ -\sin 2\theta \sinh 2r & \cosh 2r + \sinh 2r \cos 2\theta \end{pmatrix}. \end{aligned}$$

such that the expectation values are computed as

$$\begin{aligned} \langle \hat{a}_+ \rangle &= \gamma \delta(\Omega) \\ \langle \hat{a}_-^\dagger \rangle &= \gamma^* \delta(\Omega) \\ \langle \hat{p} \rangle &= 2 \operatorname{Re}\{\gamma\} \delta(\Omega) \\ \langle \hat{q} \rangle &= 2 \operatorname{Im}\{\gamma\} \delta(\Omega). \end{aligned}$$

and we compute the expectation value of our two-photon annihilation operator as

$$\langle \hat{a}_+ \rangle = \alpha \delta(\Omega) \quad \text{and} \quad \langle \hat{a}_-^\dagger \rangle = \alpha^* \delta(\Omega)$$

as well as their second momenta as

The electric field operator finally reads

$$\hat{\mathbf{E}}(\mathbf{r}, t) = i \sqrt{\frac{\hbar\omega_0}{\varepsilon_0 \mathcal{A}c}} \left[\int_{-\infty}^{\infty} \frac{d\Omega}{2\pi} \left[\hat{a}_\Omega e^{-i(\omega_0 + \Omega)t} - \hat{a}_\Omega^\dagger e^{+i(\omega_0 + \Omega)t} \right] \right] \quad (\text{V.4})$$

such that the classical part of the electric field reads

We start from the standard single-mode field quantization in terms of annihilation and

creation operators \hat{a} and \hat{a}^\dagger :

$$\hat{E}(t) = \sqrt{\frac{\hbar\omega_0}{2\varepsilon_0}} (\hat{a}e^{-i\omega_0 t} + \hat{a}^\dagger e^{i\omega_0 t}).$$

and we now make our bosonic operators time-dependent, $\hat{a} \rightarrow \hat{a}(t)$, to account for sidebands around the carrier frequency ω_0 . Using the Fourier transform convention

$$\hat{a}(t) = \int_{-\infty}^{+\infty} \frac{d\Omega}{2\pi} \hat{a}[\Omega] e^{-i\Omega t},$$

we rewrite the field operator as

$$\hat{E}(t) = \sqrt{\frac{\hbar\omega_0}{2\varepsilon_0}} \int_{-\infty}^{+\infty} \frac{d\Omega}{2\pi} (\hat{a}[\Omega] e^{-i(\omega_0+\Omega)t} + \hat{a}^\dagger[\Omega] e^{i(\omega_0+\Omega)t}).$$

$$\hat{p}[\Omega] = 2|\alpha|(\delta[\Omega] + \text{Re}\{\varepsilon[\Omega]\}) + \delta\hat{p}[\Omega], \quad (\text{V.5})$$

$$\hat{p}[\Omega] \hat{p}[\Omega'] = 4|\alpha|^2 (\delta[\Omega]S[\Omega'] + \delta[\Omega]\text{Re}\{\varepsilon[\Omega']\} + \delta[\Omega']\text{Re}\{\varepsilon[\Omega]\} + \text{Re}\{\varepsilon[\Omega]\}\text{Re}\{\varepsilon[\Omega']\}) + \delta\hat{p}[\Omega] \delta\hat{p}[\Omega'], \quad (\text{V.6})$$

$$\langle \dots \rangle = 4|\alpha|^2 (\delta(\Omega)\delta(\Omega') + \frac{\varepsilon}{2}\delta(\Omega)\delta(\Omega' - \Omega_m) + \frac{\varepsilon}{2}\delta(\Omega)\delta(\Omega' + \Omega_m)) \quad (\text{V.7})$$

$$+ \frac{\varepsilon}{2}\delta(\Omega')\delta(\Omega - \Omega_m) + \frac{\varepsilon}{2}\delta(\Omega')\delta(\Omega + \Omega_m) \quad (\text{V.8})$$

$$+ \frac{\varepsilon^2}{4} [\delta(\Omega - \Omega_m)\delta(\Omega' + \Omega_m) + \delta(\Omega - \Omega_m)\delta(\Omega' - \Omega_m) \quad (\text{V.9})$$

$$+ \delta(\Omega + \Omega_m)\delta(\Omega' + \Omega_m) + \delta(\Omega + \Omega_m)\delta(\Omega' - \Omega_m)] + \langle \delta p[\Omega] \delta p[\Omega'] \rangle. \quad (\text{V.10})$$

Derivation of the optimal angle

Optimal fixed homodyne angle with complex \mathcal{K}

Assume the measured (reflected) quadrature is

$$\delta q_r = \delta q_{\text{in}} + \mathcal{K} \delta p_{\text{in}},$$

so that, for any input covariance matrix S^{in} ,

$$S_{qq}^r = S_{qq}^{\text{in}} + |\mathcal{K}|^2 S_{pp}^{\text{in}} + 2 \text{Re}\{\mathcal{K}\} S_{pq}^{\text{in}}.$$

For an input squeezed state of strength R and angle θ ,

$$S^{\text{in}}(r, \theta) = \begin{pmatrix} \cosh 2r + \sinh 2r \cos 2\theta & -\sinh 2r \sin 2\theta \\ -\sinh 2r \sin 2\theta & \cosh 2r - \sinh 2r \cos 2\theta \end{pmatrix}.$$

Hence

$$\begin{aligned} S_{qq}^r(\theta) &= \cosh 2r - \sinh 2r \cos 2\theta + |\mathcal{K}|^2(\cosh 2r + \sinh 2r \cos 2\theta) - 2 \operatorname{Re}\{\mathcal{K}\} \sinh 2r \sin 2\theta \\ &= (1 + |\mathcal{K}|^2) \cosh 2r - (1 - |\mathcal{K}|^2) \sinh 2r \cos 2\theta - 2 \operatorname{Re}\{\mathcal{K}\} \sinh 2r \sin 2\theta. \end{aligned} \quad (\text{V.11})$$

Optimal fixed angle. Differentiate (V.11) w.r.t. θ and set to zero:

$$\frac{\partial S_{qq}^r}{\partial \theta} = 2 \sinh 2r \left[(1 - |\mathcal{K}|^2) \sin 2\theta - 2 \operatorname{Re}\{\mathcal{K}\} \cos 2\theta \right] = 0,$$

which gives the optimal fixed readout angle

$$\tan(2\theta_{\text{opt}}) = \frac{2 \operatorname{Re}\{\mathcal{K}\}}{1 - |\mathcal{K}|^2} \quad (\text{V.12})$$

Writing $\mathcal{K} = |\mathcal{K}|e^{i\varphi_m}$ one may also use

$$\tan(2\theta_{\text{opt}}) = \frac{2|\mathcal{K}| \cos \varphi_m}{1 - |\mathcal{K}|^2}.$$

Minimum attained value. Plugging the optimal angle back into (V.11) then yields

$$S_{qq,\text{min}}^r = (1 + |\mathcal{K}|^2) \cosh 2r - \sqrt{(1 - |\mathcal{K}|^2)^2 + (2 \operatorname{Re}\{\mathcal{K}\})^2} \sinh 2r, \quad (\text{V.13})$$

Lower bound and the real- \mathcal{K} case. In the free mass limit, \mathcal{K} is purely real, so that $\varphi_m = 0$ and $\operatorname{Re}\{\mathcal{K}\} = |\mathcal{K}|$. In this case, the minimum variance (V.13) reduces to

$$S_{qq,\text{min}}^r = (1 + |\mathcal{K}|^2)e^{-2r}$$

Appendix B: Error Signals

In this appendix, we detail calculation details not mentionned in the main text regarding the detection of optical fields and error signals.

Direct detection error signals

We describe the completely generic photocurrent obtained from direct detection of two optical fields interfering on a photodetector. We consider two fields with field operators \hat{a} and \hat{a}' , with classical amplitudes $|\bar{\alpha}|$ and $|\bar{\alpha}'|e^{-i(\Delta\omega t+\phi)}$ as well as fluctuations $\delta\hat{a}$ and $\delta\hat{a}'e^{-i(\Delta\omega t+\phi)}$ i.e. $\bar{\alpha}$ is real. The photocurrent operator is then given by

$$\hat{I} = \left(|\bar{\alpha}| + \delta\hat{a}^\dagger + |\bar{\alpha}'|e^{i(\Delta\omega t+\phi)} + \delta\hat{a}'^\dagger e^{i(\Delta\omega t+\phi)} \right) \left(|\bar{\alpha}| + \delta\hat{a} + |\bar{\alpha}'|e^{-i(\Delta\omega t+\phi)} + \delta\hat{a}'e^{-i(\Delta\omega t+\phi)} \right)$$

We remind here the expression for the amplitude and phase quadratures for both fields

$$\delta\hat{p} = \delta\hat{a} + \delta\hat{a}^\dagger, \quad \delta\hat{q} = -i(\delta\hat{a} - \delta\hat{a}^\dagger),$$

and

$$\delta\hat{p}' = e^{-i(\Delta\omega t+\phi)}\delta\hat{a}' + e^{i(\Delta\omega t+\phi)}\delta\hat{a}'^\dagger, \quad \delta\hat{q}' = -i(e^{-i(\Delta\omega t+\phi)}\delta\hat{a}' - e^{i(\Delta\omega t+\phi)}\delta\hat{a}'^\dagger).$$

Expanding this expression and keeping only terms up to first order in the fluctuations, we find

$$\begin{aligned} \hat{I}(t) \approx & |\bar{\alpha}|^2 + |\bar{\alpha}'|^2 + 2|\bar{\alpha}||\bar{\alpha}'| \cos(\Delta\omega t + \phi) \\ & + |\bar{\alpha}|(\delta\hat{p} + \delta\hat{p}') \\ & + |\bar{\alpha}'| \cos(\Delta\omega t + \phi)(\delta\hat{p} + \delta\hat{p}') \\ & + |\bar{\alpha}'| \sin(\Delta\omega t + \phi)(\delta\hat{q} - \delta\hat{q}') \end{aligned}$$

The first line corresponds to the classical DC and beatnote terms, while the remaining lines correspond to the fluctuations. We will now explore the different detection regimes covered in the main text.

Single field detection

Let's first consider the single field case where we get rid of all terms related to \hat{a}' . The photocurrent operator then reduces to

$$\hat{I} \approx |\bar{\alpha}|^2 + |\bar{\alpha}|\delta\hat{p}.$$

The photocurrent fluctuations are then directly proportional to the amplitude quadrature fluctuations of the input field, scaled by the classical amplitude.

Two fields detection

Let's first consider two fields with the same frequency, i.e. $\Delta\omega = 0$. The photocurrent operator then reads

$$\begin{aligned}\hat{I} \approx & |\bar{\alpha}|^2 + |\bar{\alpha}'|^2 + 2|\bar{\alpha}||\bar{\alpha}'| \cos(\phi) \\ & + |\bar{\alpha}| (\delta\hat{p} + \delta\hat{p}') \\ & + |\bar{\alpha}'| \cos(\phi) (\delta\hat{p} + \delta\hat{p}') \\ & + |\bar{\alpha}'| \sin(\phi) (\delta\hat{q} - \delta\hat{q}')\end{aligned}$$

where the mean field is a simple interference between the two fields, while the fluctuations depend on both amplitude and phase quadratures of the two fields. By adjusting the relative phase ϕ , one can select which quadrature is measured. For example, setting $\phi = 0$ selects the amplitude quadratures, while setting $\phi = \pi/2$ selects the phase quadratures. The issue is that in this case, both fields contribute to the measured quadrature fluctuations, which is not desired when probing sub shotnoise fluctuations of a signal (the LO will add its own fluctuations).

Two fields detection with frequency offset

Now, we consider the case where the two fields have a frequency offset $\Delta\omega \neq 0$. The mean photocurrent then contains a beatnote at frequency $\Delta\omega$ and reads

$$\bar{I} = |\bar{\alpha}|^2 + |\bar{\alpha}'|^2 + 2|\bar{\alpha}||\bar{\alpha}'| \cos(\Delta\omega t + \phi).$$

such that demodulating the photocurrent at frequency $\Delta\omega' \sim \Delta\tilde{\omega}$ with phase $\tilde{\phi}$ and low-pass filtering yields

$$\bar{I}_{\text{demod}} \approx |\bar{\alpha}||\bar{\alpha}'| \cos((\Delta\omega - \Delta\tilde{\omega})t + \phi - \tilde{\phi}).$$

This very signal can then be used to lock the frequency of an auxiliary laser to the desired frequency offset $\Delta\tilde{\omega}$ from the main laser. However, this signal featuring many zero crossings, one needs to tune the auxiliary laser frequency close enough to the desired offset so that it

ensures the feedback loop locks to the correct zero crossing. This is generally done manually by scanning the auxiliary laser frequency until the right zero crossing is found, confirmed by monitoring the beatnote on a spectrum analyzer.

PDH error signal

the Pound-Drever-Hall (PDH) error signal starting from the real, quantum-normalized phase-modulated electric field expression. We aim to show how the demodulated signal is a linear combination of the real and imaginary parts of the cavity reflection coefficient, with the demodulation phase selecting the appropriate quadrature for locking.

Input Phase-Modulated Field

The electric field at the input of the cavity is assumed to be a coherent state that has been phase-modulated at frequency Ω , such that the classical (real) electric field takes the form:

$$E_{\text{cl}}^{(\text{PM})}(t) = i\sqrt{\frac{\hbar\omega_0}{2\varepsilon_0}} \alpha_0 \left[e^{-i\omega_0 t} - e^{i\omega_0 t} + \frac{i\epsilon_\phi}{2} (e^{-i(\omega_0-\Omega)t} + e^{i(\omega_0-\Omega)t}) + \frac{i\epsilon_\phi}{2} (e^{-i(\omega_0+\Omega)t} + e^{i(\omega_0+\Omega)t}) \right] \quad (\text{V.14})$$

where α_0 is the coherent amplitude of the carrier, $\epsilon_\phi \ll 1$ is a small modulation index (related to the phase modulation depth), and ω_0 is the optical carrier frequency. This field includes both the positive and negative frequency components, as expected for a physical (Hermitian) electric field operator.

Reflection from the Cavity

Each frequency component of the field is reflected with a complex frequency-dependent amplitude reflection coefficient $r(\omega)$, such that the reflected field is:

$$\begin{aligned} E_{\text{refl}}(t) = & i\sqrt{\frac{\hbar\omega_0}{2\varepsilon_0}} \alpha_0 \left[r(\omega_0)e^{-i\omega_0 t} - r^*(\omega_0)e^{i\omega_0 t} \right. \\ & + \frac{i\epsilon_\phi}{2} (r(\omega_0 - \Omega)e^{-i(\omega_0-\Omega)t} + r^*(\omega_0 - \Omega)e^{i(\omega_0-\Omega)t}) \\ & \left. + \frac{i\epsilon_\phi}{2} (r(\omega_0 + \Omega)e^{-i(\omega_0+\Omega)t} + r^*(\omega_0 + \Omega)e^{i(\omega_0+\Omega)t}) \right] \end{aligned} \quad (\text{V.15})$$

Photodetected Intensity

The photodetector measures the intensity:

$$I(t) \propto |E_{\text{refl}}(t)|^2$$

We isolate the terms oscillating at Ω , which arise from the interference between the carrier and sideband components. Keeping only the beat terms between the carrier and sidebands, we find:

$$I(t) \supset \epsilon_\phi \cdot \operatorname{Re}[A_+ - A_-] \cos(\Omega t) + \epsilon_\phi \cdot \operatorname{Im}[A_+ - A_-] \sin(\Omega t) \quad (\text{V.16})$$

where we define:

$$A_\pm = r(\omega_0)r^*(\omega_0 \pm \Omega)$$

Demodulation with Arbitrary Phase

The signal is demodulated using a local oscillator $\cos(\Omega t + \phi)$, where ϕ is the demodulation phase. Using trigonometric identities:

$$\cos(\Omega t + \phi) = \cos(\Omega t) \cos \phi - \sin(\Omega t) \sin \phi$$

we multiply Equation (V.16) and low-pass filter to obtain:

$$\epsilon_{\text{PDH}}(\phi) \propto \epsilon_\phi \{\operatorname{Re}[A_+ - A_-] \cos \phi + \operatorname{Im}[A_+ - A_-] \sin \phi\} \quad (\text{V.17})$$

Sidebands Far Off-Resonance Approximation

In the standard PDH regime, the modulation frequency is much greater than the cavity linewidth:

$$\Omega \gg \kappa$$

so the sidebands are far off-resonance. This means:

$$r(\omega_0 \pm \Omega) \approx 1 \Rightarrow A_\pm \approx r(\omega_0)$$

and therefore:

$$A_+ - A_- \approx 0$$

However, if we retain the asymmetry between the sidebands (e.g., due to dispersion), or keep the finite detuning contribution, we approximate:

$$A_+ - A_- \approx r(\omega_0) [r^*(\omega_0 + \Omega) - r^*(\omega_0 - \Omega)] = r(\omega_0) \Delta r^*$$

Final Result

Substituting into Equation (V.17), we obtain:

$$\epsilon_{\text{PDH}}(\phi) \propto \epsilon_\phi \{\operatorname{Re}[r(\omega_0) \Delta r^*] \cos \phi + \operatorname{Im}[r(\omega_0) \Delta r^*] \sin \phi\} \quad (\text{V.18})$$

In the limit where $\Delta r^* \rightarrow 1$ (normalized, symmetric sidebands), this simplifies to:

$$\epsilon_{\text{PDH}}(\omega_0, \phi) \propto \cos \phi \cdot \text{Re}[r(\omega_0)] + \sin \phi \cdot \text{Im}[r(\omega_0)] \quad (\text{V.19})$$

7. Interpretation

Equation (V.19) shows that the demodulated error signal is a linear superposition of the real and imaginary parts of the complex reflection coefficient. The demodulation phase ϕ selects the detected quadrature:

- $\phi = 0$: error signal is proportional to $\text{Re}[r]$ — symmetric around resonance, not suitable for locking.
- $\phi = \pi/2$: error signal is proportional to $\text{Im}[r]$ — antisymmetric, ideal dispersive error signal.
- $\phi \neq 0, \pi/2$: mixes quadratures, possibly introducing offset or distortion.

This derivation makes explicit how the PDH method uses phase-sensitive detection to extract the component of the reflection coefficient that varies linearly with detuning, enabling precise feedback locking of the laser to the cavity resonance.

Bibliography

- [1] O. Arcizet et al. “Radiation-pressure cooling and optomechanical instability of a micromirror”. In: *Nature* 444.7115 (Nov. 2006), pp. 71–74. ISSN: 0028-0836, 1476-4687. DOI: [10.1038/nature05244](https://doi.org/10.1038/nature05244). URL: <http://www.nature.com/articles/nature05244> (visited on 01/09/2023) (cit. on p. 5).
- [2] H. J. Kimble et al. “Conversion of conventional gravitational-wave interferometers into quantum nondemolition interferometers by modifying their input and/or output optics”. In: *Physical Review D* 65.2 (Dec. 2001), p. 022002. ISSN: 0556-2821. DOI: [10.1103/PhysRevD.65.022002](https://doi.org/10.1103/PhysRevD.65.022002). URL: <http://link.aps.org/doi/10.1103/PhysRevD.65.022002> (cit. on p. 19).
- [3] Jérôme Poirson et al. “Analytical and experimental study of ringing effects in a Fabry–Perot cavity. Application to the measurement of high finesse”. In: *J. Opt. Soc. Am. B* 14.11 (Nov. 1997), pp. 2811–2817. DOI: [10.1364/JOSAB.14.002811](https://doi.org/10.1364/JOSAB.14.002811). URL: <https://opg.optica.org/josab/abstract.cfm?URI=josab-14-11-2811> (cit. on p. 29).
- [4] A. A. Clerk et al. “Introduction to Quantum Noise, Measurement and Amplification”. In: *Reviews of Modern Physics* 82.2 (Apr. 15, 2010), pp. 1155–1208. ISSN: 0034-6861, 1539-0756. DOI: [10.1103/RevModPhys.82.1155](https://doi.org/10.1103/RevModPhys.82.1155). arXiv: [0810.4729\[cond-mat, physics:quant-ph\]](https://arxiv.org/abs/0810.4729). URL: <http://arxiv.org/abs/0810.4729> (visited on 05/27/2024) (cit. on pp. 55, 57).
- [5] H. J. Kimble et al. “Conversion of conventional gravitational-wave interferometers into quantum nondemolition interferometers by modifying their input and/or output optics”. In: *Physical Review D* 65.2 (Dec. 26, 2001), p. 022002. ISSN: 0556-2821, 1089-4918. DOI: [10.1103/PhysRevD.65.022002](https://doi.org/10.1103/PhysRevD.65.022002). URL: <https://link.aps.org/doi/10.1103/PhysRevD.65.022002> (visited on 05/22/2023) (cit. on p. 62).
- [6] A. M. Jayich et al. “Dispersive optomechanics: a membrane inside a cavity”. In: *New Journal of Physics* 10.9 (Sept. 2008), p. 095008. ISSN: 1367-2630. DOI: [10.1088/1367-2630/10/9/095008](https://doi.org/10.1088/1367-2630/10/9/095008). URL: <https://dx.doi.org/10.1088/1367-2630/10/9/095008> (visited on 08/27/2024) (cit. on p. 64).

- [7] J. C. Sankey et al. “Strong and tunable nonlinear optomechanical coupling in a low-loss system”. In: *Nature Physics* 6.9 (Sept. 2010). Publisher: Nature Publishing Group, pp. 707–712. ISSN: 1745-2481. DOI: [10.1038/nphys1707](https://doi.org/10.1038/nphys1707). URL: <https://www.nature.com/articles/nphys1707> (visited on 08/27/2024) (cit. on pp. 64, 66).
- [8] C. A. Regal, J. D. Teufel, and K. W. Lehnert. “Measuring nanomechanical motion with a microwave cavity interferometer”. In: *Nature Physics* 4.7 (May 2008), pp. 555–560. ISSN: 1745-2473. DOI: [10.1038/nphys974](https://doi.org/10.1038/nphys974). URL: <http://www.nature.com/doifinder/10.1038/nphys974> (cit. on p. 89).
- [9] J. C. Sankey et al. “Strong and tunable nonlinear optomechanical coupling in a low-loss system”. In: *Nature Physics* 6.9 (June 2010), pp. 707–712. ISSN: 1745-2473. DOI: [10.1038/nphys1707](https://doi.org/10.1038/nphys1707). URL: <http://www.nature.com/doifinder/10.1038/nphys1707> (cit. on pp. 93, 105).
- [10] J. D. Thompson et al. “Strong dispersive coupling of a high-finesse cavity to a micromechanical membrane.” In: *Nature* 452.7183 (Mar. 2008), pp. 72–75. ISSN: 1476-4687. DOI: [10.1038/nature06715](https://doi.org/10.1038/nature06715). URL: <http://www.ncbi.nlm.nih.gov/pubmed/18322530> (cit. on p. 105).
- [11] D. J. Wilson et al. “Measurement-based control of a mechanical oscillator at its thermal decoherence rate”. In: *Nature* (2015), pp. 2–6. ISSN: 0028-0836. DOI: [10.1038/nature14672](https://doi.org/10.1038/nature14672). URL: <http://www.nature.com/doifinder/10.1038/nature14672> (cit. on p. 105).

Sujet : Squeezed light optomechanics: Theory and Experiments

Résumé : Cette thèse de doctorat étudie les limites quantiques à l'oeuvre dans la détection interferométrique de petits déplacements mécaniques, et comment surmonter ces dernières en utilisant de la lumière comprimée. Dans un premier temps, le travail traite théoriquement la faisabilité d'une lumière comprimée dépendante en fréquence via l'utilisation d'une cavité de filtrage/rotation en sortie d'un amplificateur paramétrique optique. Dans un second temps, il se concentre sur la faisabilité d'une détection sous la limite quantique standard (SQL) en détaillant deux expériences réalisées. La première implémente un système « membrane at the edge » (MATE) basé sur une membrane en nitrure de silicium à haut facteur de qualité mécanique monté dans une cavité Fabry Perot de grande finesse. La deuxième expérience présente une source de lumière comprimée indépendante de la fréquence. Ces deux expériences sont pilotées à l'aide de locks optiques digitaux basé sur FPGA et développé au laboratoire, permettant un fonctionnement stable dans les conditions requises pour des mesures à la limite quantique.

Mots clés : Optomecanique, Lumière comprimée, Cavité de grande Finesse, Interferométrie, Bruit thermique, Bruit de grenaille quantique, Resonateur de grand facteur de Qualité, Interféromètres pour la detection d'ondes gravitationnelles, Bruit de pression de radiation quantique

Subject : Optomechanics and squeezed light

Abstract:

Keywords : Optomechanics, Squeezing, High-Finesse cavity, Interferometry, Thermal Noise, Quantum Shot Noise, High-Q Resonator, Gravitational wave Interferometer, Quantum Radiation Pressure Noise

